Dissertation

submitted to the
Combined Faculties of the Natural Sciences and Mathematics
of the Ruperto-Carola-University of Heidelberg, Germany
for the degree of
Doctor of Natural Sciences

Put forward by
Dennis Patrick Schulz
born in: Heidelberg

Oral examination: 5. May 2021

Development and characterization of MOCCA, a 4k-pixel molecule camera for the energy-resolved detection of neutral molecule fragments

Referees: Prof. Dr. Christian Enss
Prof. Dr. Maurits Haverkort

The MOCCA detector is a 64 × 64-pixel molecule camera with an active area of 4.5 cm×4.5 cm, developed for the energy-resolved detection of neutral molecule fragments at kinetic energies up to 300 keV at the Cryogenic Storage Ring (CSR) at the Max Planck Institute for Nuclear Physics, Heidelberg. Its principle is based on metallic magnetic calorimeters (MMCs): an energy deposition in the detector leads to an increase in temperature, resulting in a change in magnetization of a paramagnetic sensor, which can be measured with a SQUID. This thesis presents the detector design, the cleanroom processing and the developed cryogenic and electronic platform to operate the detector. To ensure a good thermalization over the complete detector, a process to produce gold-filled through-wafer vias was optimized and used. In characterization measurements, the full functionality of the readout system of MOCCA is presented. In measurements with 5.9 keV X-ray photons, an energy resolution of 88 eV is demonstrated. With the results obtained in this thesis, MOCCA fulfills all requirements for the challenging experiments planned at CSR, presently making it the largest and most complex operational MMC-type detector array.

Entwicklung und Charakterisierung von MOCCA, einer 4k-Pixel-Molekülkamera für die energieauflösende Detektion von neutralen Molekülfragmenten

Der MOCCA-Detektor ist eine 64 × 64-Pixel-Molekülkamera mit einer aktiven Fläche von 4.5 cm × 4.5 cm, die für die energieauflösende Detektion neutraler Molekülfragmente mit Energien bis zu 300 keV am Cryogenic Storage Ring CSR am Max-Planck-Institut für Kernphysik in Heidelberg entwickelt wurde. MOCCA basiert auf metallischen magnetischen Kalorimetern (MMCs): Die durch die Absorption eines Teilchens deponierte Energie führt zu einer Erhöhung der Temperatur, die wiederum zu einer Änderung der Magnetisierung eines paramagnetischen Sensors führt, welche mit einem SQUID gemessen wird. In dieser Arbeit wird das Design und die Herstellung von MOCCA und die entwickelte kryogene und elektronische Plattform zu seiner Auslesung mittels 32 zweistufigen dc-SQUIDs vorgestellt. Um eine gute Ankopplung des Detektors an das thermische Bad zu erreichen, wurde ein Prozess zur Herstellung goldgefüllter Silizium-Durchkontaktierungen entwickelt. In Charakterisierungsmessungen mit 5.9 keV-Röntgenphotonen erreichte MOCCA eine Energieauflösung von 88 eV. Damit erfüllt MOCCA alle Anforderungen für die herausfordernden Experimente am CSR und ist zum jetzigen Stand der größte, komplexeste MMC-basierte Detektor.

Contents

1. Introduction

Molecular clouds are large accumulations of interstellar medium in the universe and the dominant location for the formation of new stars. Their chemical composition has been the subject of intense research, started by the observation of absorption bands of neither planetary nor stellar origin [Har04], and identifying the first interstellar molcules CH and CN about 80 years ago [McK40b, McK40a, Ada41]. There still are interstellar absorption bands discovered in the 1930s whose origin is unknown [Mer34, Kre20], and the reaction paths leading to the chemical composition of molecular clouds is not well understood: While these clouds seem to be unlikely places for the formation of complex molecules due to their low densities, high radiation fields and temperatures around 10 K [Sno06], research has uncovered the existence of molecules such as buckminster fullerenes (C_{60} and C_{70}, [Zha11, Cam10]) and many other many-atom molecules, with new ones constantly being added to the list.

From the many possible reaction types present in these clouds, one process is considered especially vital for reaction networks in molecular clouds: dissociative recombination. In dissociative recombination, a positively charged ion recombines with an electron and quickly dissociates into neutral molecule fragments. This barrierless process is regarded as the dominant neutralizing mechanism in interstellar matter and an efficient destruction mechanism for molecules with high proton affinities [Lar12, Wak10]. However, studying dissociative recombination in a lab-based setup is demanding: Due to the low temperatures and the low densities of molecular clouds, molecules in space will typically occupy their lowest rotational and vibrational state. These states have long relaxation times, and in a radiation field of 300 K, much higher rotational states are excited. For that reason, most of the data on dissociative recombination was recorded neglecting the rotational state of the molecule [Kre19].

In order to gain a better understanding of the abundance and reaction networks of molecules in interstellar molecular clouds, the Cryogenic Storage Ring (CSR) at the Max Planck Institute for Nuclear Physics was constructed. The ring, built to store molecules at energies between 20 and 300 keV, has a beam circumference of 35 m and can be continuously cooled to temperatures below 10 K [vH16]. The CSR is also the only cryogenic electrostatic storage facility using electron cooling, enabling brilliant ion beams for a good resolution in collision studies [Kre19]. The excellent vacuum and the low temperatures enable storage times long enough for particles to relax into their rotational ground states for measurements such as the recently published state-specific rate coefficients for dissociative recombination [Nov19a].

However, the currently used detector setup does not allow for energy-resolved measurements, limiting the range of molecules that can be investigated to simple systems. In order to investigate the dissociative recombination of complex multi-atom molecules, fully identifying all the reaction products and the kinetic energy released during dissociative recombination, a large, spatially and energy-resolving detector able to detect neutral molecule fragments at low kinetic energies is needed. For this, the molecule camera MOCCA was designed. MOCCA is based on metallic magnetic calorimeters (MMCs), a versatile type of detector that has shown excellent energy resolutions in measurements with X-ray photons [Kra20]. MMCs are used for a wide range of experiments [Hen17, Vel19, Gei20, Sik20], and were used to detect neutral massive particles in test measurements [Nov15, Gam19]. With its 4096 pixels and a detection area of $4.5\,\mathrm{cm} \times 4.5\,\mathrm{cm}$, MOCCA is presently the largest granular MMC-based detector. It can be read out using only 32 dc-SQUID channels. This thesis presents the design and the fabrication of the MOCCA detector, describes the readout system developed to acquire data with the detector, and characterizes MOCCA using measurements with X-ray photons and alpha particles, proving its full functionality for the planned demanding experiments at CSR.

Chapter 2 explains the scientific motivation and the measurement principle at CSR. Then, chapter 3 introduces the basic principles of MMCs. The used dilution refrigerator, the ADCs and the program used for data acquisition are presented in chapter 4.

Chapter 5 describes the design of the MOCCA detector and the cryogenic and electronic platform for running experiments with that detector, developed within this thesis. The cleanroom procedures are summed up, and a reliable process for producing gold-filled through-wafer vias is presented, which was first used on a MOCCA detector characterized in this thesis. The readout infrastructure and the planned setup for deployment of MOCCA at CSR are presented. Then, the methods used for the data analysis are introduced. As MMCs are very sensitive to electromagnetic noise caused by, e.g. mobile phone emissions, recorded traces have to be pre-filtered before fitting the pulse data, for which a very effective and fast set of filters were developed. Finally, the used setups for the characterization of MOCCA are introduced.

Chapter 6 presents the characterization of finished MOCCA detectors. After demonstrating the successful use of the filters, the inductance of the pick-up coils of the MOCCA detector is deducted from noise measurements. The full readout principle of MOCCA is shown, and the signal shape is analyzed. With its low cross-talk, the excellent energy resolution and the spatial resolution of its 4096 pixels, MOCCA fulfills all requirements for deployment at the CSR.

2. The Cryogenic Storage Ring CSR

The Cryogenic Storage Ring (CSR) at the Max Planck Institute for Nuclear Physics in Heidelberg is an electrostatic storage ring for beams of anions and cations with energies of up to 300 keV per charge unit. In this chapter, the scientific motivation for building the CSR and its technical setup will be explained. Then, the current detector setup and the advantages of installing a new detector based on Metallic Magnetic Microcalorimeters will be discussed.

2.1 Scientific motivation

Molecular clouds are accumulations of interstellar medium. Typically, their sizes can reach several hundred parsecs with masses up to $10^7\,\mathrm{M}_\odot$ [Fuk10]. They act as centres of star formation in the universe. The conditions in those clouds - low temperatures of a few Kelvin and low particle densities - seem to make them an unlikely environment for the formation of complex organic molecules [Sno06]. However, since the first molecules present in these clouds were identified in the 1930s [Fel01], intense research has uncovered a plethora of molecules present in the interstellar medium, including complex many-atom molecules like buckminsterfullerenes (C_{60} and C_{70}) and ethyl methyl ether ($C_2H_5OCH_3$) [Zha11, Sel10, Cam10, Ter18], with new molecules still being added to the list (see, for example, [Riv20, Biz20, McG20, Xue20]). A constantly updated overview of all confirmed molecule species can be found in the Cologne Database for Molecular Spectroscopy [Mül01, Mül05].

Those molecules, their abundance and their reaction networks play an important part in interstellar chemistry. To gain understanding of how interstellar chemistry works, a reliable and correct knowledge of reaction cross sections and ratios is needed. One of the types of reactions possible in the interstellar medium is the so-called dissociative recombination. Schematically, dissociative recombination can be described as

$$\mathrm{AB}^+ + e^- \rightarrow \mathrm{A} + \mathrm{B}, \tag{2.1}$$

where AB^+ is an arbitrary, singly charged positive molecular ion which breaks apart into two neutral molecule fragments A and B.

Dissociative recombination has several properties that make it a vital component of reaction network of molecular clouds: the reaction does not have an energy barrier, and the rate increases with decreasing translational energy of the reaction constituents [Lar12]. Dissociative recombination is regarded as the dominant neutralizing mechanism in interstellar matter and can act as an efficient destruction mechanism for molecules with high proton affinities [Wak10]. In some environments, stable cations can only be destroyed with dissociative recombination [Lar12]. However, studying reaction rates of dissociative recombination using an earth-based laboratory setup is demanding: Due to the low density in molecular clouds, molecules inside the clouds will typically occupy their lowest rotational and vibrational state, because time between collisions of molecules can be months or years. For lab-based experiments, this poses a problem: Rotational states can have long relaxation times and can be excited in a radiation field of 300 K [Kre19], but most experimental data available was recorded in room-temperature setups, neglecting the rotational states of the molecules. Recently published measurements suggests that rotational states play a significant role for reaction rates, as shown for the electron recombination rate of HeH^+, a primordial molecule important for the formation of the first stars [Nov19a].

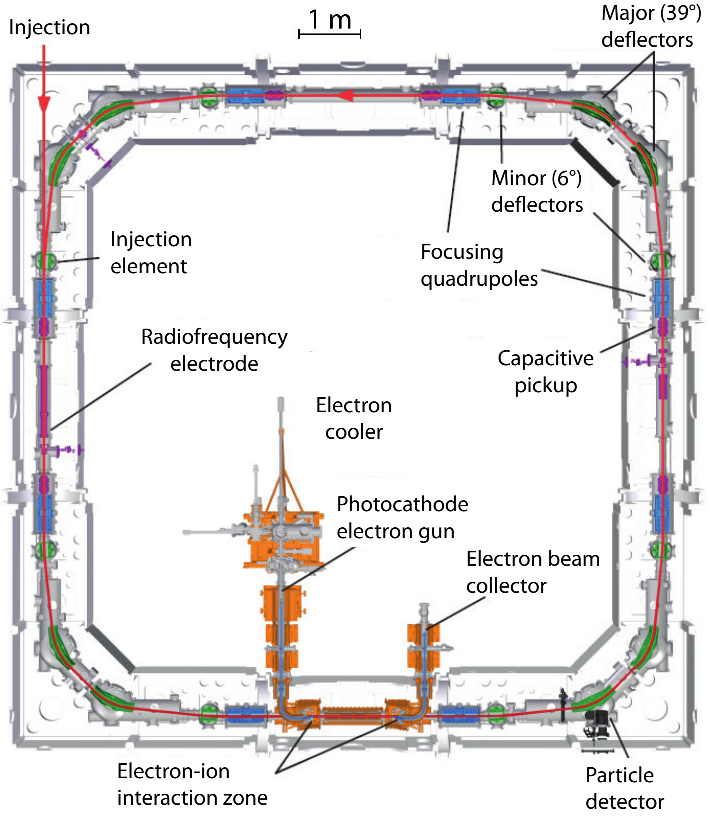

Figure 2.1: Sketch of the CSR from above. Beams are injected into the CSR at the top left corner and circulate in counter clockwise direction. The electron cooler, shown in orange, is positioned in the straight section that also houses the detectors. Picture taken from [Nov19b].

Several electrostatic storage rings have been built to enable measurements on these systems: DESIREE in Sweden, RICE at RIKEN in Japan and the Cryogenic Storage Ring CSR at the Max-Planck-Institute for Nuclear Physics in Heidelberg [Sch13, Nak17, vH16]. The largest of those, CSR, will be described in the next section.

2.2 Setup of the CSR

The Cryogenic Storage Ring is a electrostatic cryogenic storage ring at the Max Planck Institute for Nuclear Physics in Heidelberg for collisional and laser-interaction studies over long storage times with ion beams at energies between 20 keV and 300 keV per charge unit. The beam chamber can be continously cooled, reaching temperatures below 10 K and extremely low pressures below 10^{-13} mbar. On its first comissioning runs, temperatures of 5.5 K and a vacuum below 140 particles/cm^3, equivalent to a room-temperature pressure of below 10^{-14} mbar, were reported. While this section aims at giving an overview over the facility, a detailed description of the cryogenic and vacuum design can be found in [vH06, vH11, vH16], while more recent reports of performance can be found, for example, in [Nov19b] or [Kre19].

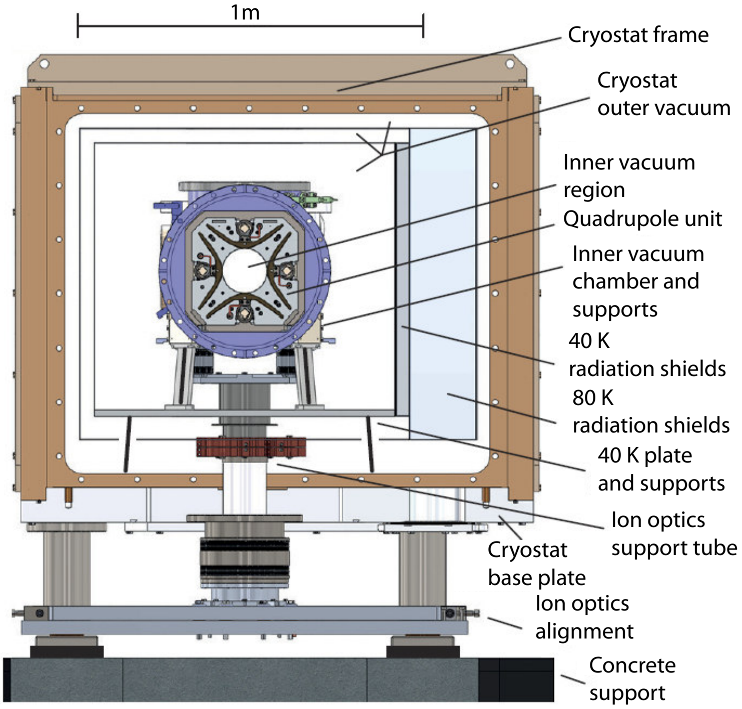

Figure 2.2: Schematic cross section of the CSR perpendicular to the beam direction. Shown are a focussing quadrupole inside the beam line, the two temperature shields at 40 K and 80 K and the mechanical support for the chambers. Taken from [vH16].

The general layout of the CSR is shown in figure 2.1. It consists of four straight beam lines for housing different experimental setups. These sections are connected with four deflection quadrants, each consisting of two minor 6° and two major 39° deflectors. If a neutral is formed in one of the straight sections, it passes through a gap between the deflectors into a space where detectors can be placed. The ion beam is created on a 300 kV acceleration platform and injected into the CSR. The platform can create both atomic and molecular beams, including beams of heavy bio-molecules.

A sketch of a sectional cut through the CSR beam tube is shown in figure 2.2. The beam chamber is cooled with liquid helium, while the 40 K and 80 K shields are cooled with helium gas. Both are supplied via an external refrigerator. The freezing of residual gas on specifically prepared cryogenic surfaces contributes to the exceptional vacuum inside the CSR.

One of the straight sections of the CSR houses an electron cooler, described in detail in [Wil19]. Inside the electron cooler section, the ion beam is superimposed with a nearly mono-energetic, velocity-controlled electron beam over the distance of about 1 m, enabling phase-space cooling of the ion beam. Additionally, the section where the electron and the ion beam overlap can act as the interaction region to study processes like dissociative recombination. A detector setup for detection of the produced neutral molecule fragments is positioned in beam direction straight behind the electron cooler. The detection principle for those molecule fragments, the resulting requirements for a detector setup and the current detector setup at the Cryogenic Storage Ring are discussed in the next section.

2.3 Detection principle and requirements at the CSR

The reaction products of dissociative recombination, the recombination of an electron and a molecular ion succeeded by a dissociation into various molecule fragments, can take many different forms. Assuming a singly charged positive ion ABC^+, comprised of three atoms A, B and C, undergoes dissociative recombination with an electron, the reaction products can be

$$\mathrm{ABC}^+ + e^- \rightarrow \begin{cases} \mathrm{A} + \mathrm{B} + \mathrm{C} \\ \mathrm{AB} + \mathrm{C} \\ \mathrm{A} + \mathrm{BC} \\ \mathrm{AC} + \mathrm{B} \end{cases} . \tag{2.2}$$

To completely distinguish all reaction channels and correctly measure branching ratios, a mass resolved measurement is needed. Also, the kinetic energy $\mathrm{E}_{\mathrm{kin}}$ released at the dissociation is of scientific interest.

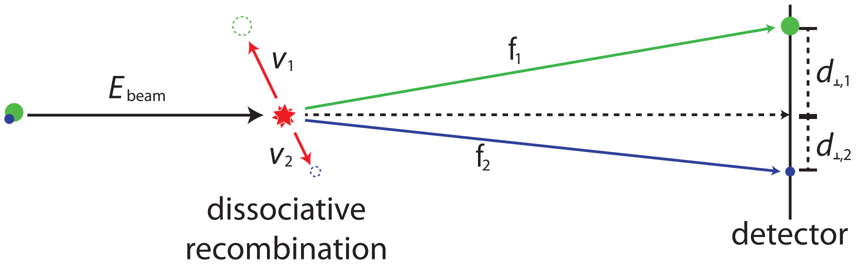

Figure 2.3: Schematical drawing of the particle trajectories at the CSR: An ion enters the electron-ion interaction region with the beam energy E_{beam} and undergoes dissociative recombination, symbolically depicted by the fragmentation into the blue and the green fragment. Due to the kinetic energy released in the reaction, the particle hits the detector at a distance $d_{\perp,i}$ to the prolonged beam direction.

The particle trajectories after a dissociative recombination inside the CSR are shown in figure 2.3. The molecule enters the electron-ion interaction region with a known kinetic energy E_{beam}. Due to the energy released at the dissociative recombination, both molecule fragments receive an additional velocity v_i, whose direction depends on the orientation of the molecule upon dissociation. As the kinetic energy released during dissociation is typically much lower than the kinetic energy of the beam molecules, the beam velocity can be assumed as constant during dissociative recombination. The absorbed kinetic energy in the detectors for one fragment f_i,

$$E^{\text{lab}}_{\text{kin},i} = \frac{1}{2} m_{\text{f}_i} v_i \approx \frac{1}{2} m_{\text{f}_i} v_{\text{beam}}, \tag{2.3}$$

is therefore directly correlated with the mass of the impinging particle, allowing for molecule fragment identification. However, as shown in figure 2.3, the released energy does lead to a slight change of the particle trajectory, leading to a temporal and spatial shift when impinging on a flat detector surface perpendicular to the beam direction. Therefore, to fully resolve the reaction dynamics, the detector used in this setup has to fulfill the following three requirements: Firstly, the detector needs to be able to detect neutral molecule fragments over a vast mass range with kinetic energies in the range of the CSR, i.e. 20 to 300 keV. Secondly, energy- and space-resolved detection is necessary to differentiate multiple molecule fragments hitting the detector almost simultaneously. Thirdly, a timing resolution of a few nanoseconds could allow to resolve the time-of-flight differences of the molecule fragments. Apart from that, the detector has to work in a fully cryogenic environment under very low pressures, adding the need to limit outgassing of all materials to a minimum.

2.4 Current detector setup at the CSR

The current detector setup at CSR consists of two types of Micro-Channel Plate-type detectors, both able to detect neutral molecule fragments: the COMPACT and the NICE detector.

The NICE detector (**N**eutral **I**maging in **C**old **E**nvironment) is a double-stack 120 mm microchannel plate detector. The anode is comprised of a phosphor screen. A CCD camera records the picture of the phosphor screen in timesteps of 2 µs [Nov19b]. The spatial resolution of the detector is reached by analyzing these pictures of the phosphor screen.

The COMPACT detector (**Co**ld **M**ovable **Pa**rticle **C**oun**T**er) is used as a hit counter and consists of an aluminium converter plate and a Multi-Channel Plate which collects the secondary electrons created by particles hitting the aluminium plate. This detector is mounted on a translational stage to enable measurements not only of neutral particles, but also of ions that left the nominal orbit. Count rates of up to $10^3\,\mathrm{s}^{-1}$ were achieved without saturating the detector [vH16].

A restriction with both detectors is that they are unable to provide mass-sensitive measurements. This is currently limiting measurements at the CSR to simple molecule systems: In measurements, if the reaction product consists of two fragments, collecting the respective impact positions over many reactions and then analyzing the distribution can yield the angular distributions of the reaction, together with the kinetic energy released [Nov19b]. In the case of more complex reactions with more possible reaction channels and products, the ability for mass-resolved measurement becomes a necessity.

For this reason, a new detector based on metallic magnetic calorimeters and an infrastructure to run this detector were developed within the realm of this thesis. This detector type is described in the next chapter.

3. Metallic Magnetic Calorimeters

Metallic Magnetic Calorimeters (MMCs) are low-temperature detectors, mostly used for high-resolution energy dispersive detection of X-ray photons. First suggested by F. Simon et al. in 1935 [Sim35], they are used for a wide range of precision measurements: Most recently, MMCs were used to measure the isometric energy of the thorium isotope ^{229}Th for establishing new time standards [Sik20, Gei20]. MMCs are the detector technology used in the ECHo project which investigates the neutrino mass using the analysis of the electron capture spectrum of ^{163}Ho [Gas17]. They are also used to measure standard calibration lines for gamma detectors in more detail [Kim20]. A multi-pixel large-area MMC is suggested as a technology for the LYNX telescope [Ste19, Ban19].

MMCs also allow the detection of massive particles such as alpha particles and molecules, even at comparably low kinetic energies [Gam19]. Therefore, a detector based on this technique was built for use at the CSR, fulfilling the conditions outlined in chapter 2.3. In this chapter, the basic working principle of MMC detectors and their abilities will shortly be explained. A more extensive and in-depth description can, for example, be found in [Fle03, Fle05, Fle09].

3.1 Working principle

The principle of MMCs is based on the first law of thermodynamics. Their general scheme is shown in figure 3.1: MMCs consist of a particle absorber and a sensitive thermometer, both in good thermal contact with each other. The thermometer consists of a paramagnetic sensor read out by a pick-up coil made from superconducting material. The whole setup is placed inside an external magnetic field B_{ext}, therefore, the sensor exhibits a temperature-dependent magnetization. Changes in the magnetization of the sensor lead to a change of the magnetic flux inside the superconducting pick-up coil, which in turn induces a current in the coil. This signal is measured using a SQUID current sensor. To keep the detector at a stable base temperature, the sensor has a weak thermal coupling to a stable temperature bath, usually at a few millikelvin.

When a photon or a massive particle hits the absorber, the deposited energy ΔE leads to a change of the detector temperature of

$$\Delta T \simeq \frac{\Delta E}{C_{\text{tot}}}, \tag{3.1}$$

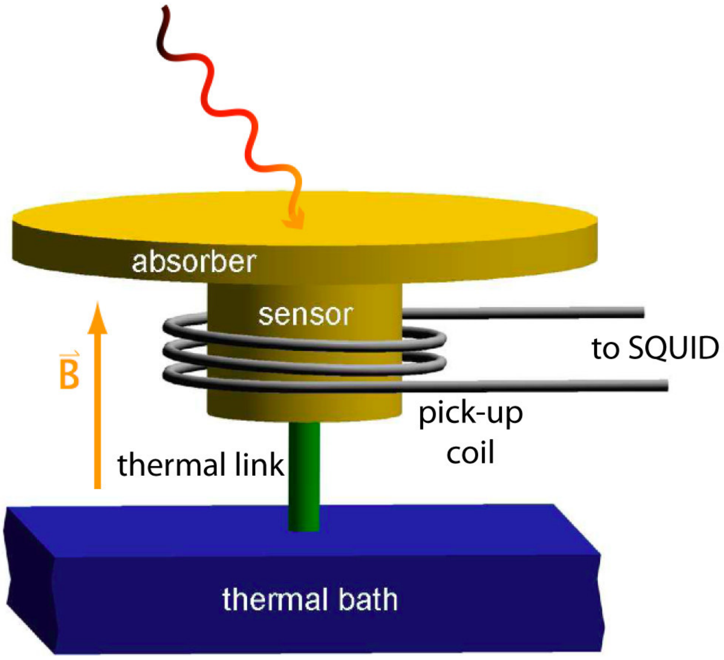

Figure 3.1: General scheme of a metallic magnetic calorimeter.

where $C_{\mathrm{tot}} = C_{\mathrm{a}} + C_{\mathrm{s}}$ is the total heat capacity of the MMC, comprised of the heat capacity of the absorber C_{a} and the sensor C_{s}. This change in temperature of the sensor leads to a change ΔM of its temperature-dependent magnetization, which can be expressed as

$$\Delta M = \frac{\partial M}{\partial T}\Delta T = \frac{\partial M}{\partial T}\frac{\Delta E}{C_{\mathrm{tot}}}. \tag{3.2}$$

The change in magnetization ΔM of the paramagnetic sensor leads to a change of magnetic flux $\Delta\Phi$ in the pick-up coil, which in turn leads to a change $\Delta\Phi_{\mathrm{s}}$ of magnetic flux in the dc-SQUID:

$$\Delta\Phi_{\mathrm{s}} \propto \Delta\Phi \propto \Delta M \propto \Delta T. \tag{3.3}$$

Two basic requirements for maximizing the MMC signal - and, therefore, the signal-to-noise-ratio - can already be derived from equation 3.2: Firstly, keeping the heat capacity of sensor and absorber of an MMC small, and secondly, having a strong temperature dependence of the sensor magnetization around working temperatures of the detector. The first requirement is fulfilled both by keeping all components of the MMC small in volume and by running the detector at cryogenic temperatures, as both the phononic ($c_{\mathrm{p}} \propto T^3$) and the electronic ($c_{\mathrm{e}} \propto T$) contribution to the specific heat of the detector decrease with temperature.

The material choice for MMCs is of high importance and significantly influences the detector properties. In the next section, the choice for the sensor material will be discussed.

3.2 Sensor material

A material showing temperature-dependent magnetization at millikelvin temperatures can be fabricated by embedding paramagnetic ions into a non-magnetic host material. Early MMCs used dielectric materials as host material for the ions, however, the coupling between phonons and magnetic moments at low temperatures is very weak with relaxation times in the range of some milliseconds to seconds [Bue88, Bue93, Fau93]. This leads to very slow signal rise times, limiting the rate and the timing resolution of these detectors. For this reason, S. Bandler et al. [Ban93] suggested to use a normal conducting metallic host material instead. In those materials, the magnetic moments can interact with the conduction electrons, allowing for much faster relaxation times below 100 ns [Fle09]. This is usually preferable, even though the conduction electrons lead to an additional interaction between the magnetic moments of the $^{3+}$Er ions, the so-called RKKY interaction described in section 3.2.1.

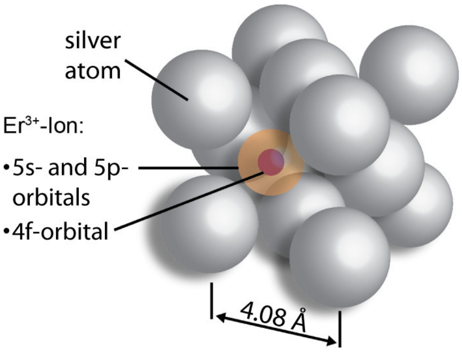

Figure 3.2: Schematical view of the Ag:Er atomic grid. Shown are the atoms of the host material, silver, and the 4f, 5s and 5p orbitals of an $^{3+}$Er ion substituting a silver atom on a regular lattice site.

Within the frame of this thesis, silver, doped with a few hundred ppm of Erbium, was used as the sensor material, denoted as Ag:Er in the subsequent text. A schematic illustration of the atomic grid of Ag:Er is shown in figure 3.2. Pure silver has a face-centered cubic lattice structure with a lattice constant of 4.08 Å and shows a weak diamagnetic behaviour. In low concentrations, Erbium occupies a regular lattice site, adding three of its electrons to the electron gas, resulting in an electron configuration of $[\mathrm{Kr}]4\mathrm{d}^{10}4\mathrm{f}^{11}5\mathrm{s}^{2}5\mathrm{p}^{6}$. Since the 4f-shell of the $^{3+}$Er ions is only filled with 11 out of the possible 14 electrons, the $^{3+}$Er ion exhibits a permanent magnetic moment, leading to the desired paramagnetic behaviour of the sensor.

The diameter of the 4f-shell is only 0.6 Å [Fra76] and, therefore, located deep within the outer 5s- and 5p-shells with diameters of 2 Å, shielding it well from the influence of the crystal field. Using Hund's rules, the total spin of this system is

$S = 3/2$, the angular momentum $L = 6$ and the total angular momentum $J = L + S = 15/2$. With this, both the resulting Landé factor

$$g_J = 1 + \frac{S(S+1) + J(J+1) - L(L+1)}{2J(J+1)} = \frac{6}{5} \tag{3.4}$$

and the magnetic moment of the Erbium ions

$$\mu = -g_{\mathrm{J}}\mu_{\mathrm{B}}J \tag{3.5}$$

can be calculated [Abr70], where $\mu_{\mathrm{B}} \simeq 9.27 \times 10^{-24}\,\mathrm{J/T}$ is the Bohr magneton. The contribution of the crystal field leads to a splitting of the 16-fold degenerate Er^{3+} ground state into a set of multiplets. Below temperatures of 200 K, this cannot be neglected anymore [Wil69] when calculating the magnetization $M(T)$ or the specific heat $C(T)$. Using neutron scattering, the energy splitting between the ground state doublet and the first excited multiplet was measured to be around $25\,\mathrm{K}\times k_{\mathrm{B}}$ for $\underline{\mathrm{Ag}}$:Er [Hah92], where $k_{\mathrm{B}} \simeq 1.38 \times 10^{-23}\,\mathrm{J/K}$ is the Boltzmann constant. For that reason, higher multiplets can be neglected at working temperatures of MMCs below 100 mK, and the behaviour can be described as a two-level system with effective spin $\tilde{S} = 1/2$ and isotropic Landé factor $\tilde{g}_{\underline{\mathrm{Ag}}:\mathrm{Er}} = 6.84$ [Tao71].

3.2.1 Heat capacity and magnetization of the sensor

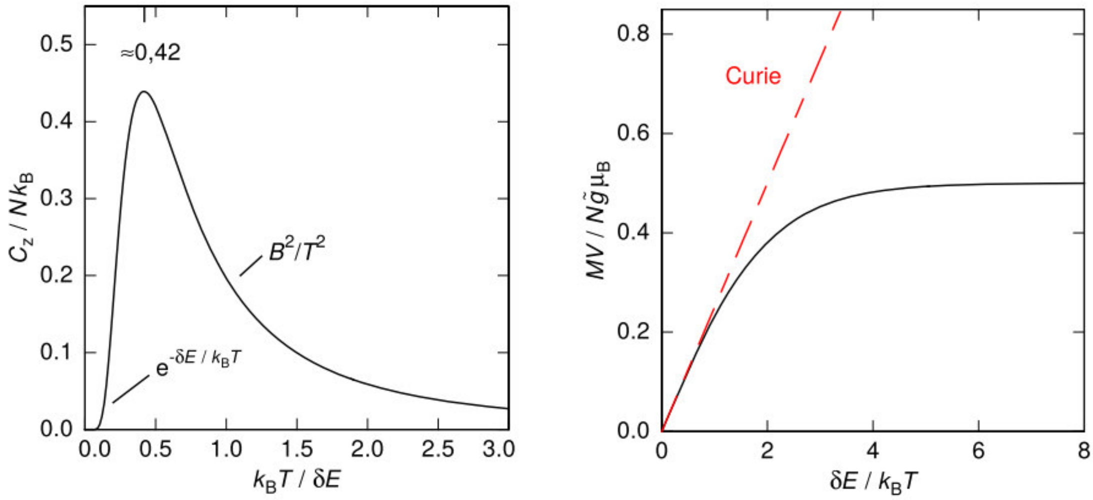

Figure 3.3: Reduced specific heat (**left**) and reduced magnetization (**right**) for a system consisting of N independent two-level systems with spin $\tilde{S} = 1/2$ and energy splitting $\partial E = \tilde{g}\mu_{\mathrm{B}}B$. The high-temperature Curie behaviour is indicated by the dashed line.

To model the behaviour of MMCs, the change of magnetization with temperature $\partial M/\partial T$ and the heat capacity of the sensor C_{s} need to be known. In [Fle03], both of these quantities were successfully modeled for the largely similar system of erbium-doped gold. As shown there, the Au:Er system with very low concentrations of ${}^{3+}$Er ions can be approximated as an ensemble of non-interacting magnetic moments. In a magnetic field B, the ${}^{3+}$Er ions with spin $\tilde{S}$ experience a Zeeman splitting of the ground state into $2\tilde{S}+1=2$ energy levels. In thermodynamic equilibrium, the occupation of these levels is given by a Boltzmann distribution, resulting in a heat capacity of the Zeeman system of

$$C_\mathrm{Z}(T) = N k_\mathrm{B} \left(\frac{\delta E}{k_\mathrm{B} T}\right)^2 \frac{e^{\delta E/k_\mathrm{B}T}}{\left(e^{\delta E/k_\mathrm{B}T}+1\right)^2}, \tag{3.6}$$

where N is the number of independent magnetic moments and $\delta E = \tilde{g}\mu_\mathrm{B} B$ is the energy splitting of the according two-level system. The characteristics of this curve are shown on the left-hand side of figure 3.3. The graph shows a maximum at a heat capacity of $C_\mathrm{Z} \approx 0.44\, N k_\mathrm{B}$ for $k_\mathrm{B}T \approx 0.42\,\delta\mathrm{E}$, known as Schottky anomaly. Towards low temperatures, the heat capacity drops according to $e^{-\delta E/k_\mathrm{B}T}$. For high temperatures, the heat capacity is proportional to B^2/T^2. The according calculations for the magnetization show that, in the limit of low temperatures, the magnetization approaches a saturation value of

$$M \approx \frac{N}{2V_\mathrm{s}} \tilde{g}\mu_\mathrm{B}, \tag{3.7}$$

for a density of magnetic moments N/V_s. Towards high temperatures, the magnetization shows a Curie-like behavior with $M \propto B/T$. The saturation corresponds to the case where all magnetic moments inside the sensor are oriented in parallel to the external magnetic field, allowing no further increase in magnetization. The behavior of the magnetization over a large temperature range is shown on the right-hand side in figure 3.3.

While the assumption of non-interacting magnetic moments is good enough for qualitative estimates, in reality, two interaction mechanisms of the ${}^{3+}$Er ions and the nuclear spin of one of the Erbium isotopes have to be taken into account as well:

- The **dipole-dipole interaction** describes the direct interaction between pairs of ${}^{3+}$Er ions. The interaction is an-isotropic and decreases with r_{ij}^{-3}, where r_{ij} is the distance between two ions i and j.
- The **RKKY interaction**[1] [Rud54, Kas56, Yos57] describes the indirect interaction of two Er^{3+} ions via a polarization of the conduction electrons of the host material. The RKKY interaction is isotropic and spatially oscillating, but

---

[1] Named after the initials of the first scientists to theoretically describe the interaction, M.A. Ruderman, C. Kittel, T. Kasuya and K. Yosida

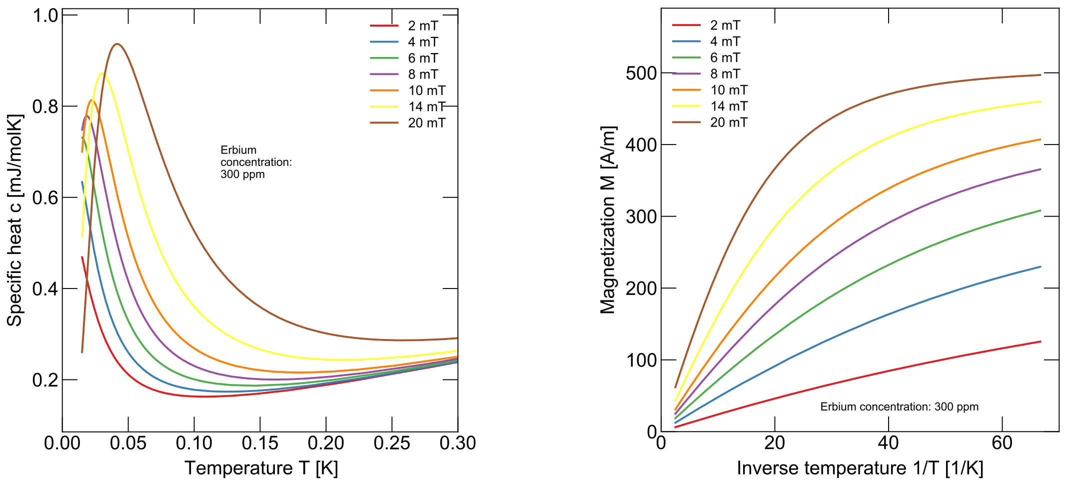

Figure 3.4: Simulated temperature dependency of the specific heat and the magnetization of an Ag:Er sample with an assumed Erbium concentration of 300 ppm. Calculated with a simulation written by Matthew Herbst [Her22] on the basis of a simulation for Au:Er by [Fle03].

decreases with r_{ij}^{-3}, just as the dipole-dipole interaction. It contributes to the specific heat and, therefore, leads to a decreased signal height in the range of interesting temperatures and magnetic fields for operating MMCs.

- In its natural composition, Erbium contains 22.9% of ^{167}Er, which possesses a nuclear spin of $I = 7/2$. This leads to a hyperfine splitting of the ground state doublet. Excitations between the two multiplets do not necessarily lead to a change in magnetization, therefore, the presence of ^{167}Er can reduce the signal size [Fle00].

Figure 3.4 shows the results for magnetization and specific heat from a simulation for a sensor made of silver containing an Er^{3+} concentration of 300 ppm for different external magnetic fields B, using the method of exact diagonalisation of the Hamiltonian describing the interaction and taking the RKKY and the dipole-dipole interaction into account [Her22]. Compared to the simulations based on the case of non-interacting magnetic moments from figure 3.3, the temperature dependence of heat capacity and magnetisation are qualitatively similar. Both the maximum of the Schottky anomaly and the temperature where the magnetization saturates depend on the magnetic field. For the detector within this thesis, enriched Er was used, rendering the contribution of ^{167}Er negligible. Measurements on erbium-doped gold show a good match between the simulated data for that material and experimental data [Fle03].

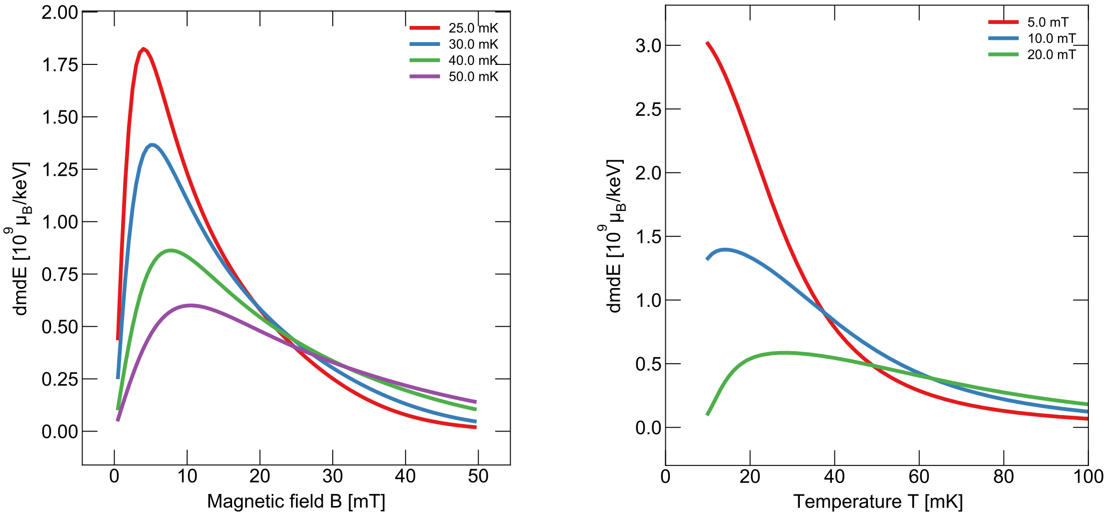

Figure 3.5: Calculated signal height per absorbed energy as a function of the external magnetic field (**left**) and the detector temperature (**right**) for an exemplary detector with an absorber made from gold with a size of 1.4 mm×1.4 mm×4 µm and a sensor size of 400 µm×400 µm×2 µm and an erbium concentration of 300 ppm in an Ag:Er sensor assuming non-interacting magnetic moments. Data for the specific heat of silver and gold taken from [Isa65, Mar73]. The external magnetic field B was assumed to be homogeneous.

3.2.2 Signal height

As shown in equation 3.2, the signal height of an MMC is proportional to the temperature dependence of the magnetization of the sensor material. The change in magnetic moment of a sensor with the volume V_s can be calculated by integrating over the sensor volume V_s, neglecting the interactions between the $^{3+}$Er ions. The total heat capacity of the sensor is comprised of the heat capacity of the spin system C_Z, the heat capacity of the electrons C_e and the heat capacity of the phonons C_ph, therefore, only the share $C_\mathrm{Z}/(C_\mathrm{Z}+C_\mathrm{e}+C_\mathrm{ph})$ of the deposited energy ΔE contributes to the detector signal. The change in magnetic moment of a sensor in an exterior magnetic field B can therefore be expressed using

$$\Delta m = \frac{C_\mathrm{Z}(B,T)}{C_\mathrm{Z}(B,T)+C_\mathrm{e}(T)+C_\mathrm{ph}(T)}\frac{\Delta E}{B}. \tag{3.8}$$

As shown in equation 3.6, the heat capacity of the Zeeman system C_Z depends both on the temperature and on the external magnetic field B. Figure 3.5 shows the signal height per absorbed energy as a function of the external magnetic field and the detector temperature. For these graphs, the detector was assumed to have an absorber made from gold with a size of 1.4 mm × 1.4 mm × 4 µm, a Ag:Er sensor with a size of 400 µm × 400 µm × 2 µm and an Erbium concentration of 300 ppm. For the sake of the argument, the external magnetic field is assumed to be homogeneous. As can be seen in the left plot, the dependency between magnetic field and signal height is approximately linear for small magnetic fields B. A maximum is reached when C_Z is approximately the same as the heat capacity of the electron system C_e and the phonon system C_ph. Towards higher magnetic fields, the signal height decreases $\propto 1/B$.

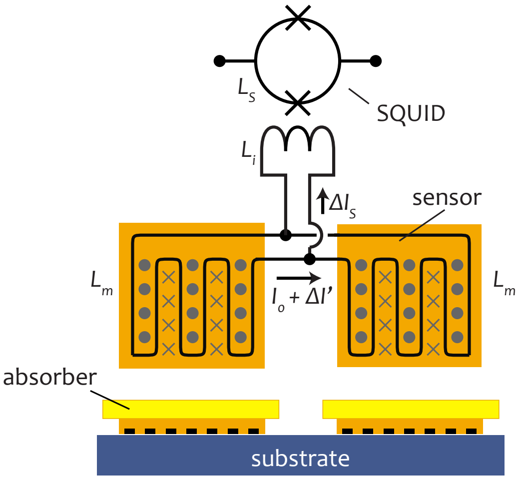

Figure 3.6: Schematic drawing of a readout geometry used for MMCs: Two planar, meander-shaped pick-up coils are placed below one sensor each. The input coil of the SQUID is connected to the coils so that the polarity of the signal determines from which of the two sensors the signal originated. A persistent current I_0 inside the superconducting loop induces the magnetic field for the sensor. Taken from [Hen17] after [Fle05].

3.3 Sensor readout

The change in magnetization upon the absorption of a particle in the detector discussed in the last section has to be coupled into the input coil of a SQUID current sensor for measurement. Using micro-fabrication techniques for MMC fabrication allows detector designs with more pixels and more complex geometries. A range of possible basic geometries is discussed in [Fle05], one of the most commonly used designs is shown in figure 3.6 and will be discussed in this section: Two planar, meander-shaped pick-up coils are connected in parallel to the input coil of a SQUID current sensor, typically using bonding wires. A persistent current I_0 can be prepared in the superconducting circuit formed by the two meander-shaped pick-up coils. A change of magnetic flux in one of the coils induces screening currents in all parts of the circuit, leading to a change in current through the input coil of the

SQUID current sensor. The signals resulting from flux changes in the two coils can be distinguished by the polarity of the signal.

This design has a range of advantages. By preparing a persistent supercurrent in the meander-shaped coils, they create the magnetic field for the sensor. As sensor and pick-up coil are just separated by a thin, electrically isolating layer, the coupling between pick-up coil and the sensor is comparably high. Another advantage is that the two coils can be designed in a way that they are gradiometrically coupled, making the setup less sensitive to external magnetic field changes. Finally, each SQUID can read out two sensors independently, reducing the number of needed SQUIDs and, by that, the needed wiring, which is often a limiting factor in cryogenic setups.

The inductance of a meander-shaped pick-up coil with center-to-center line distance p and meander area A is approximately given by

$$L_\mathrm{m} = l\mu_0 \frac{A}{p}, \tag{3.9}$$

where $\mu_0 \simeq 1.257 \times 10^{-6}\mathrm{Vs/Am}$ is the vacuum permittivity and l is a constant depending on the magnetic penetration depth λ_L of the superconducting material and the respective geometry, for example in form of w/p, with w being the width of the lines and p being the center-to-center distance of adjacent lines. For $w = 5\,\mu\mathrm{m}$, $p = 9\,\mu\mathrm{m}$ and $\lambda_\mathrm{L} \ll w$, l is approximately 0.2.

Generated magnetic field

The magnetic field distribution created by the current in the pick-up coil is highly inhomogeneous and decreases exponentially with the distance from the pick-up coil plane. The resulting field distribution can be calculated using numerical methods. The spatial dependency of the magnetic field $\mathbf{B}(\mathbf{r})$ inside the sensor can be described by introducing a dimensionless geometry factor

$$G(\mathbf{r}/p) = \frac{p}{\mu_0} \frac{|\mathbf{B}(\mathbf{r})|}{I_0}. \tag{3.10}$$

Exemplary simulations for the magnetic field inside a sensor on top of a meander with a pitch of $p = 9\,\mu\mathrm{m}$ and a width of $w = 5\,\mu\mathrm{m}$ can be found in [Sch15].

Flux change in the pick-up coil

The dimensionless factor $G(\mathbf{r}/p)$ defined in equation 3.10 can also be used in order to calculate the flux change inside the pick-up coil when a particle is absorbed in the detector [Bur04]. Taking an infinitesimally small volume element $\mathrm{d}V_\mathrm{s}$ of the sensor, a change of magnetization $\Delta M(\mathbf{r})$ inside that sensor volume leads to a change of flux in the pick-up coil of

$$d(\delta\Phi) = \frac{\mu_0}{p}\, G(\mathbf{r}/p)\, \Delta M(\mathbf{r}) \mathrm{d}V. \tag{3.11}$$

The total change of magnetic flux can be calculated by integrating $\mathrm{d}V$ over the full sensor volume. Taking into account that the specific heat in the sensor $c_\mathrm{s}(B(\mathbf{r}))$ depends on the magnetic field at position $\mathbf{r}$, this integral can only be solved numerically due to the complicated spatial dependence of B and G. To circumvent this, the weighted average

$$\langle X \rangle = \int\limits_0^\infty X\, P(B)\, \mathrm{d}B = \int\limits_0^\infty X\, P(G)\, \mathrm{d}G \tag{3.12}$$

can be used instead, where $P(B)$ and $P(G)$ are the probability to find the field B and the coupling factor G inside the sensor volume, respectively. With this, the flux change in the pick-up coil can be expressed as

$$\frac{\delta\Phi}{\delta E} = \frac{V_\mathrm{s}}{V_\mathrm{s}\langle c_\mathrm{s}\rangle + C_\mathrm{a}} \left\langle \mu_0 \frac{G}{p} \frac{\partial M}{\partial T} \right\rangle . \tag{3.13}$$

Flux change in the SQUID

The magnetic flux Φ inside of superconducting loops is conserved. Therefore, a change in the magnetization of the sensor that leads to a flux change $\Delta\Phi_i$ in the superconducting pick-up coil i induces screening currents in all parts of this superconducting network. For detectors using pairs of identically shaped pick-up coils connected in parallel to the input coil of the SQUID current sensor, as is the case for the geometry shown in figure 3.6, the change of current in the input coil of the SQUID ΔI_s can be expressed using Kirchhoff's laws as

$$\Delta I_\mathrm{s} = \frac{\Delta\Phi_1 - \Delta\Phi_2}{L_\mathrm{m} + 2(L_\mathrm{i} + L_\mathrm{b})}. \tag{3.14}$$

Here, L_i is the inductance of the input coil of the SQUID, and L_b is the inductance of the bonding wires connecting the detector with the input coil of the SQUID current sensor. The change ΔI_s of current through the input coil leads to a flux change

$$\Delta\Phi_\mathrm{s} = M_\mathrm{is} \Delta I_\mathrm{s} \tag{3.15}$$

in the SQUID, where M_is is the mutual inductance

$$M_\mathrm{is} = k\sqrt{L_\mathrm{i} L_\mathrm{s}} \tag{3.16}$$

with the coupling factor k. With equation 3.14, the change of flux in the SQUID is given by

$$\Delta\Phi_\mathrm{s} = M_\mathrm{is}\Delta I_\mathrm{s} = \frac{k\sqrt{L_\mathrm{i}L_\mathrm{s}}}{L_\mathrm{m} + 2(L_\mathrm{i} + L_\mathrm{b})}(\Delta\Phi_1 - \Delta\Phi_2). \tag{3.17}$$

External, macroscopic magnetic field changes or changes of the temperature of the complete detector do not lead to a signal in the SQUID as their effects in both coils cancel each other out, assuming both coils are attached to the input coil of the SQUID in a completely symmetrical way.

3.4 Signal shape

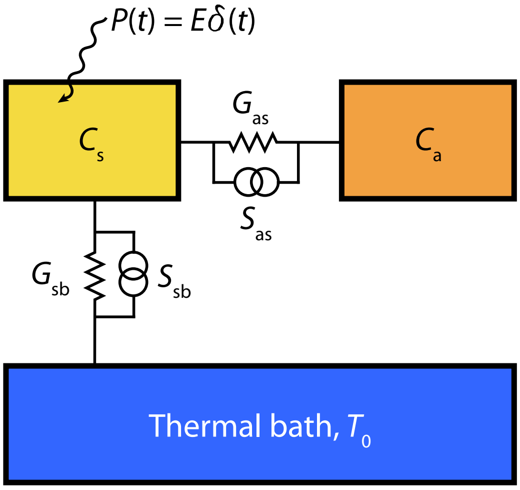

Figure 3.7: Thermal subsystems of an MMC, as modelled in [Fle05]. Depicted are the subsystem of the absorber and the subsystem of the sensor with heat capacities C_a and C_s, the thermal conductances G_{ij} between the subsystems, noise sources S_{ij}, a power input $P(t)$ into the system and the thermal bath at experimental temperature T_0.

One possibility to model the signal shape of an MMC is to assume it as consisting of two thermal subsystems: the system of the absorber with heat capacity C_a and the system of the sensor with heat capacity C_s [Fle05]. This is shown schematically in figure 3.7. The system of the sensor and the system of the absorber are connected via a thermal link with the thermal conductance G_as, while the sensor is connected with a heat bath with the thermal conductance G_sb. Assuming an instantaneous energy input $E\delta(t)$ into the absorber and neglecting the noise sources S_as and S_sb for the moment, the resulting system is described by the coupled differential equations

$$\dot{E}_\mathrm{a}(t) = C_\mathrm{a}\dot{T}_\mathrm{a}(t) = -\left(T_\mathrm{a} - T_\mathrm{s}\right)G_\mathrm{as} + E\delta(t) \tag{3.18}$$

and

$$\dot{E}_{\mathrm{s}} = C_{\mathrm{s}}\dot{T}_{\mathrm{s}}(t) = -\left(T_{\mathrm{s}} - T_{\mathrm{a}}\right)G_{\mathrm{as}} - \left(T_{\mathrm{s}} - T_0\right)G_{\mathrm{sb}} \tag{3.19}$$

where E_{a} and E_{s} are the energy content and T_{a} and T_{s} are the temperature of the subsystem of the absorber and the sensor, respectively. T_0 is the bath temperature. In the detectors discussed here, the thermal link between absorber and sensor is significantly better than the thermal link between sensor and thermal bath. Therefore, assuming $G_{\mathrm{as}} \gg G_{\mathrm{sb}}$, the system of differential equations yields

$$E_s(t) = \Delta E\, p(t) \tag{3.20}$$

where $p(t)$ is the point spread function

$$p(t) \approx \frac{C_{\mathrm{s}}}{C_{\mathrm{tot}}}(-e^{-t/\tau_a} + e^{-t/\tau_b}), t > 0. \tag{3.21}$$

The time constants can be approximated to the rise time

$$\tau_a \simeq \frac{C_{\mathrm{s}}C_{\mathrm{a}}}{C_{\mathrm{tot}}G_{\mathrm{as}}} \tag{3.22}$$

and the decay time

$$\tau_b \simeq \frac{C_{\mathrm{tot}}}{G_{\mathrm{sb}}}. \tag{3.23}$$

Therefore, the expected signal of the detector can be described by the sum of two exponential functions. Both the rise time and the decay time can be influenced by the detector design, as the fast rise time depends on the thermal conductance between absorber and sensor, and the slow decay time depends on the thermal conductance between sensor and thermal bath. Also, as the heat capacities of sensor and absorber are temperature-dependent, the rise time and the decay time are temperature-dependent, too.

3.5 Energy resolution

The noise contributions to the signal of MMCs are well understood. In this section, the dominant noise contributions limiting the energy resolution of an MMC will be discussed.

3.5.1 Thermodynamical energy fluctuations

The energy resolution of an MMC is fundamentally limited by thermodynamic energy fluctuations between the different thermal subsystems of the detector. To get the spectral power density of the fluctuations of the energy content of the sensor, the model shown in figure 3.7 can be used. This time we omit the energy input by an absorbed particle $P(t)$, but we include the energy fluctuations represented by the two noise sources labeled S_{as} and S_{sb} for the energy fluctuations between absorber and sensor and the energy fluctuations between sensor and thermal bath, respectively. The spectral power density of the noise caused by these fluctuations is frequency-independent and can be described by $S = 4k_{\mathrm{B}}T^2G_{ij}$. In analogy to the coupled differential equations 3.18 and 3.19, the differential equations for this system are

$$\dot{E}_{\mathrm{a}}(t) = C_{\mathrm{a}}\dot{T}_{\mathrm{a}}(t) = -(T_{\mathrm{a}} - T_{\mathrm{s}})G_{\mathrm{as}} - S_{\mathrm{as}}(t) \tag{3.24}$$

and

$$\dot{E}_{\mathrm{s}}(t) = C_{\mathrm{s}}\dot{T}_{\mathrm{s}}(t) = -(T_{\mathrm{s}} - T_{\mathrm{a}})G_{\mathrm{as}} - (T_{\mathrm{s}} - T_{\mathrm{b}})G_{\mathrm{sb}} + S_{\mathrm{as}}(t) + S_{\mathrm{sb}}(t). \tag{3.25}$$

Assuming $\tau_{\mathrm{a}} \ll \tau_{\mathrm{b}}$, C_{a} to be in the same range as C_{s}, and assuming that both noise sources contribute incoherently to the total noise, solving those differential equations for the energy fluctuations in the sensor yields

$$S_{E_{\mathrm{s}}}(f) \approx 4k_{\mathrm{B}}T^2C_{\mathrm{s}}\left((1-\beta)\frac{\tau_{\mathrm{a}}}{1+(2\pi\tau_{\mathrm{a}}f)^2} + \beta\frac{\tau_{\mathrm{b}}}{1+(2\pi\tau_{\mathrm{b}}f)^2}\right), \tag{3.26}$$

where $\beta = C_{\mathrm{s}}/C_{\mathrm{tot}}$ is the ratio between the heat capacity of the sensor and the total heat capacity of the detector. Using the Fourier transform of the point spread function $\tilde{p}(f)$ from equation 3.21, the signal-to-noise ratio can be given as

$$\mathrm{SNR}^2(f) = \frac{|\tilde{p}(f)|^2}{S_{E_s}(f)} \approx \frac{1}{k_{\mathrm{B}}T^2C_{\mathrm{s}}}\left(\frac{\beta\tau_{\mathrm{b}}}{1+\frac{1-\beta}{\beta}\tau_{\mathrm{a}}\tau_{\mathrm{b}}(2\pi f)^2}\right). \tag{3.27}$$

As described in [Fle03], using the method of optimal filtering, this yields an instrumental line width

$$\begin{aligned}\Delta E_{\mathrm{FWHM}} &= 2\sqrt{2\ln 2}\left(\int_0^\infty \mathrm{SNR}^2(f)\mathrm{d}f\right)^{-1/2} \\ &\approx 2\sqrt{2\ln 2}\sqrt{4k_{\mathrm{B}}T^2C_{\mathrm{a}}}\left(\frac{1}{\beta(1-\beta)}\right)^{1/4}\left(\frac{\tau_{\mathrm{a}}}{\tau_{\mathrm{b}}}\right)^{1/4},\end{aligned} \tag{3.28}$$

which defines a fundamental limit of the energy resolution of an MMC. This limit, assuming metallic absorbers with $C_{\mathrm{a}} \propto T$, is approximately proportional to $T^{3/2}$. For $\beta = 0.5$, the instrumental line width shows a minimum, meaning that MMCs reach the best energy resolution if the heat capacity of the absorber is equal to the heat capacity of the sensor. The energy resolution also relies on the rise and decay time of the signal: the energy resolution is better for faster rise times and slower decay times. However, additional noise contributions originating from the experimental setup itself have to be taken into account. Those are explained in the following sections.

3.5.2 Additional noise contributions

Magnetic Johnson Noise

In normal-conducting metallic materials, the random motion of charge carriers leads to fluctuating magnetic fields. This creates the so-called Magnetic Johnson Noise S_{Φ_j}, a magnetic flux noise in pick-up coils that contributes to the total noise of an MMC. In experiments, it is mostly caused by sensors and parts of the experimental setup that stay normal-conducting at experimental temperature, such as parts made out of copper or brass. As shown in [Pie08, Pie12], the spectral noise density in a normal conductor positioned parallel to the plane of a meander-shaped pick-up coil is proportional to σT, where σ is the electrical conductivity of the normal-conducting material.

This contribution is approximately frequency-independent in the frequency range used for the readout of metallic magnetic calorimeters. It becomes smaller with decreasing temperature and can be reduced by limiting the amount of normal conductors in close proximity of the detector. For detectors using Ag:Er as sensor material, this contribution is typically negligibly small compared to other noise contributions [Pie12].

1/f noise of the Erbium ions

For MMCs using erbium-doped noble metals as sensors, an additional noise contribution, approximately inversely proportional to frequency, was observed. This noise contribution was shown to depend on the concentration of Er^{3+} ions inside the sensor material [Dan05] and was measured to be independent of temperature between 30 mK and 4.2 K [Fle03]. Further measurements showed that the noise can be described by assuming that every ion contributes to the noise with

$$S_\mathrm{m}(f) \approx 0.1 \times \frac{\mu_\mathrm{B}^2}{f^\zeta} \tag{3.29}$$

with the exponent ζ taking values between 0.8 and 1. By integrating over all the Erbium ions in the sensor by using the weighted geometry coefficient introduced in equation 3.10, the spectral noise density of all Erbium ions can be expressed as

$$S_{\Phi_\mathrm{Er}}(f) = \frac{\mu_0 \langle G^2 \rangle}{p^2} S_\mathrm{m}(f) N_\mathrm{Er} \propto \frac{N_\mathrm{Er}}{f^\zeta}, \tag{3.30}$$

with the total number of Erbium ions N_Er.

While the physical source of this noise remains unclear, measurements on spin glass systems showed similar fluctuations of magnetic moments [Kog81]. However, the spin glass transition temperature is far below the experimental temperatures of MMCs.

3.5.3 Total noise

In addition to the noise contributions mentioned above, the SQUID itself adds the noise $S_{\Phi_\mathrm{s}}(f)$, as will be described later in chapter 4.1.3. As all contributions are statistically independent to each other, they can be summed up to get the total noise of an MMC in the SQUID. Using the flux-to-flux coupling $\Delta\Phi_\mathrm{s}/\Delta\Phi$, the total noise in the SQUID is

$$S_{\Phi_\mathrm{tot}}(f) = \left(\frac{\Delta\Phi_\mathrm{s}}{\Delta\Phi}\right)^2 \left(S_{\Phi_{\mathrm{E_s}}}(f) + S_{\Phi_\mathrm{j}} + S_{\Phi_{\mathrm{Er}}}(f)\right) + S_{\Phi_\mathrm{s}}(f). \tag{3.31}$$

For the special case of using MMCs to detect massive particles, additional effects have to be taken into account. Those are summed up in the next section.

3.6 Detection of massive particles with MMCs

MMCs have often been used to measure the energy of photons. When using this detector type to measure massive particles, additional effects can occur that deteriorate an energy spectrum obtained with an MMC. An incident, massive particle on an absorber loses its kinetic energy by interactions with absorber electrons and scattering with the ion cores of the host material, which creates phonons that undergo further scattering, but also lattice defects. The particle then comes to a full stop within the absorber and remains inside the absorber as an impurity. During the impact of a particle, the following three mechanisms can occur that lead to a energy loss, i.e. energy that is not converted to heat:

- In **back scattering**, shown in figure 3.8a), the scattering on the host material of the absorber creates a trajectory that leads to the incident particle leaving the absorber again. The kinetic energy of the particle when leaving the absorber is missing in the detector measurement of the total kinetic energy of the particle.
- If, during the absorption, enough energy is transmitted to a surface-adjacent absorber atom, it can leave the absorber, taking its kinetic energy from the measurement of the total kinetic energy. This process, shown in figure 3.8b), is called **sputtering**.
- Due to scattering, an atom in the absorber material can be pushed to an interstitial lattice site, leading to a so-called **Frenkel defect**. This is shown

in figure 3.8c). Frenkel defects consist of an atom occupying an interstitial site in a lattice and the regular lattice position of the atom which is now left vacant. At room temperature, such pairs recombine very fast, however, at the operating temperature of MMCs below 0.1 K, they remain stable [De 75]. A massive particle with kinetic energies of 100 keV can create a few hundred Frenkel pairs on impact.

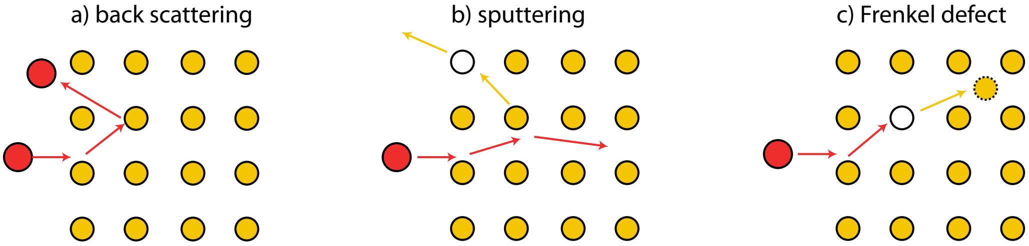

Figure 3.8: Schematical drawing of the possible effects of the absorption of a massive particle in an absorber: a) back scattering of the incident particle, b) sputtering of absorber atoms, and c) creation of a Frenkel defect. The atoms of the lattice are shown as yellow circles, the incident particle is shown in red. Empty lattice sites are shown as circles.

As these effects heavily depend on the absorber material, extensive simulations and measurements on the performance of MMCs exposed to massive particles - considering both the measurement itself and a possible long-term degradation of the detector - were examined in detail in [Gam17, Gam19].

4. Experimental methods

In this chapter, parts of the infrastructure to run an MMC-type detector are introduced. First, the SQUIDs already mentioned in previous chapters are described. Then, the dilution refrigerator used to reach low temperatures and the setup for data acquisition will be presented. Parts that were developed within this thesis are discussed in chapter 5.

4.1 dc-SQUIDs

SQUIDs[1] are extremely sensitive and fast sensors for changes in magnetic flux. They are based on the Josephson effects [Jos62]. A SQUID with an integrated input coil (a SQUID current sensor) can be used to measure very small current signals such as the output of pick-up coils of MMCs. In that case, a change of current ΔI in the input coil leads to a change of magnetic flux $\Delta\Phi_\mathrm{s}$ in the SQUID. Within this thesis, dc-SQUIDs designed and fabricated by our group in the institute cleanroom were used for readout of signals of the MOCCA detector. While an exhaustive description of SQUIDs can be found in [Cla04], this section summarizes the working principle and different noise contributions of SQUIDs.

4.1.1 Working principle of a dc-SQUID

Figure 4.1a) shows a sketch of a dc-SQUID. It consists of a superconducting loop, interrupted by two Josephson junctions, indicated by crosses. The Josephson junction enable magnetic flux to enter into the loop. A shunt resistor is connected in parallel to each junction to prevent hysteretic behavior of the SQUID. A current I_b is applied to the SQUID, while the voltage U_s over the SQUID is measured.

Josephson junctions are realized as thin layers of non-superconducting materials between two superconducting materials. When applying a current I_b to the SQUID, each junction can carry a superconducting current up to a critical current $I_\mathrm{c}/2$. This critical current depends periodically on the magnetic flux through the SQUID, where the period is the magnetic flux quantum $\Phi_0 = h/2e = 2.07 \times 10^{-15}\,\mathrm{Vs}$. When the current I_b becomes larger than the critical current, a part of the current is carried by quasi-particles tunneling through the Josephson junction. This leads to a voltage U_s over the SQUID. In figure 4.1b), this voltage is shown as a function of the applied

---

[1] SQUID is an acronym for **S**uperconducting **Qu**antum **I**nterference **D**evice.

current for the two extreme cases of $\Phi_\mathrm{s} = n \times \Phi_0$ and $\Phi_\mathrm{s} = (n + \frac{1}{2})\Phi_0$ with $n \in \mathbb{N}$. The voltage across the SQUID as a function of the magnetic flux is shown in figure 4.1c).

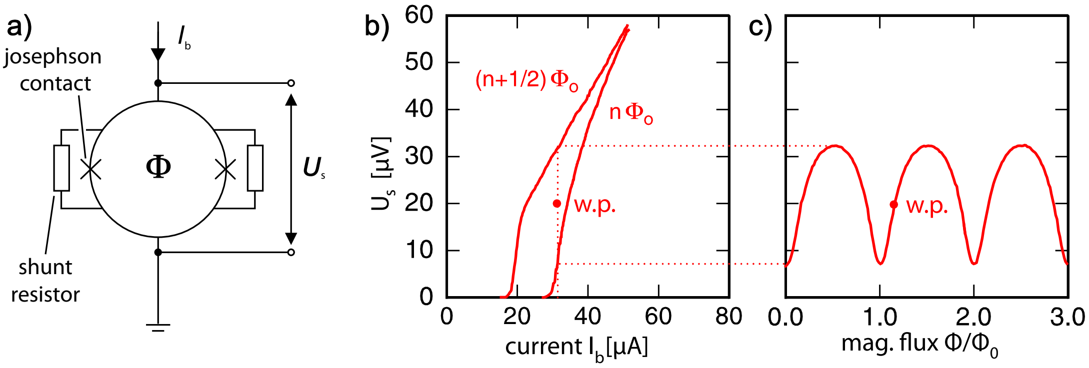

Figure 4.1: (a) Sketch of a dc-SQUID consisting of a superconducting loop with two Josephson junctions. A shunt resistor is added in parallel to each Josephson junction. (b) Current-voltage characteristic of a dc-SQUID for a magnetic flux of $n\Phi_0$ and $(n + 1/2)\Phi_0$ inside the SQUID loop. (c) Dependence of the voltage U_s across the SQUID on the magnetic flux through the SQUID loop, given in units of Φ_0.

If the SQUID is in the state indicated as working point (w.p.) in figure 4.1b) and c), any change in magnetic flux in the SQUID leads to a change in voltage across the SQUID. In this mode, the SQUID acts as a flux-to-voltage converter with a resolution far better than Φ_0. However, the periodic flux-voltage-characteristics only allows measurements in a very small range: the signal from the SQUID is approximately linear only in a range of about $\Phi_0/4$ around the optimum working point. To circumvent this limitation and keep the SQUID output linear over a large range of magnetic flux, the SQUID can be operated in a flux-locked-loop setup, which is described in the next chapter.

4.1.2 Flux-locked loop

Single-stage flux-locked loop

A flux-locked-loop (FLL) setup is used to keep the SQUID output signal linear to Φ_s over a large range of magnetic flux Φ_s. This is achieved by stabilizing the SQUID at a working point on a steep part of the flux-voltage characteristic. Figure 4.2 shows a sketch of this FLL-setup. In a flux-locked loop circuit, the voltage U_s across the SQUID is fed into a differential amplifier at room temperature. As a reference voltage of the amplifier, the voltage U_b over the SQUID at the chosen working point is used. The signal of the amplifier is then integrated using a voltage integrator, whose output serves two functions: firstly, it is connected to a feedback coil in series with a feedback resistor R_{fb}. A current through the feedback coil leads to a change of the magnetic flux in the SQUID, mediated by the mutual inductance M_{fb}. Assuming large gain for the amplifier, this loop compensates any flux changes in the SQUID [Cla04], keeping the flux Φ_{s} inside the SQUID constant at the working point. Secondly, the output voltage

$$U = -\frac{R_{\mathrm{fb}}}{M_{\mathrm{fb}}}\Delta\Phi_{\mathrm{s}} \tag{4.1}$$

of the circuit is proportional to the flux Φ_{s} in the SQUID, providing an output signal linear to the external magnetic flux through the SQUID over many Φ_0. The gain of this loop can be adjusted by choosing R_{fb}.

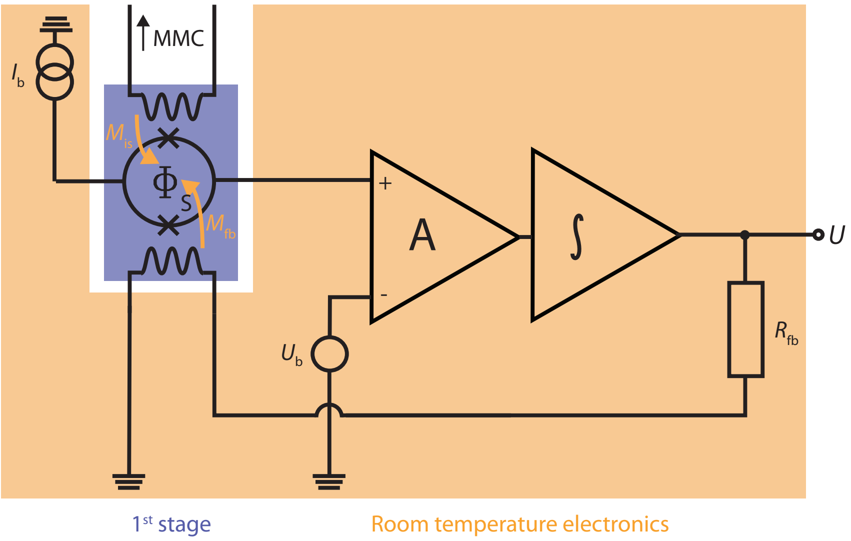

Figure 4.2: Connection diagram for a single-stage flux-locked loop circuit. The single stage of the FLL at millikelvin temperatures is drawn in purple. The part of the circuit located in the room-temperature electronics have an orange background.

One flaw in the described SQUID readout is the fact that the output impedance of the SQUID is at least a factor of 10 smaller than the input impedance of the room temperature amplifier. Therefore, impedance matching and overall noise performance can be improved by adding an amplifying stage at cryogenic temperatures. For this, a so-called two-stage flux-locked loop setup is used, which is described in the next section.

Two-stage flux-locked loop

In order to pre-amplify the detector signal at cryogenic temperatures, a series array of 16 SQUIDs with a common bias current I_{b2} and a common input coil were used in this thesis. In practice, they behave like one SQUID with a 16-fold output signal. This series array will be called (amplifier) SQUID array in the subsequent text, while the dc-SQUID used for readout of the pick-up coils of the detector will be referred to as front-end SQUID.

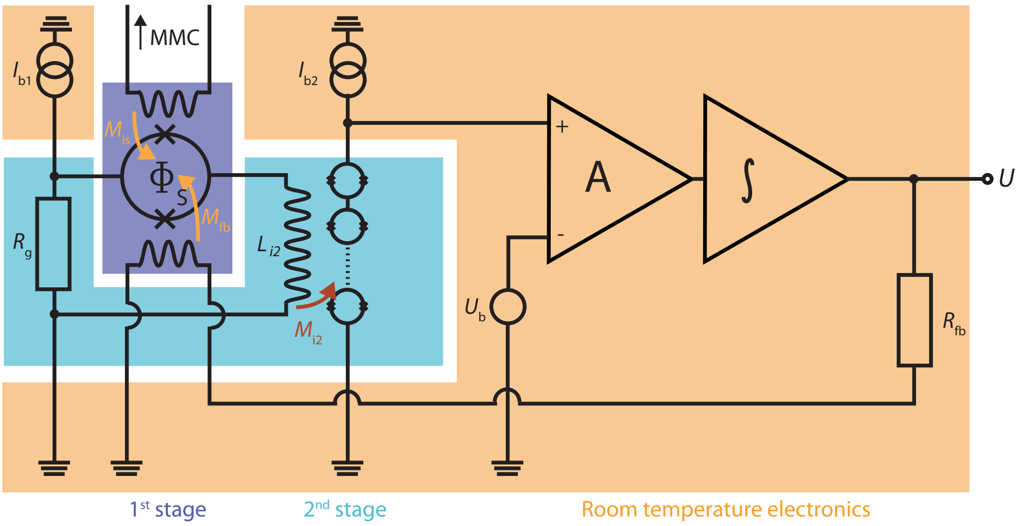

Figure 4.3: Connection diagram for a two-stage flux-locked loop circuit, enabling amplification of the signal already at the low experimental temperatures. The background is purple for parts of the circuit belonging to the first stage, blue for the second stage, and orange for the room-temperature electronics.

The circuit for using SQUID arrays for impedance matching is shown in figure 4.3. In this circuit, the front-end SQUID is connected in parallel to a gain resistor R_g and the input coil L_{i2} of the SQUID array. This input coil has a mutual inductance M_{i2} with the SQUID array. The detector SQUID and the SQUID array are operated with different bias currents, I_{b1} and I_{b2}. In this setup, I_{b1} splits up and flows both through the gain resistor R_g and the SQUID plus the inductance L_{i2}. For that reason, the working point of the front-end SQUID is determined by both the bias current I_{b1} and the gain resistor R_g. The gain resistor is chosen to be significantly smaller than the dynamic resistance of the front-end SQUID. This keeps the voltage over the front-end SQUID approximately constant, making the SQUID act as a flux-to-current converter. Any flux change in the front-end SQUID leads to a current change in the input coil of the SQUID array. The SQUID array is connected with the room temperature electronics in a way analog to the front-end SQUID in the previous section, with the output of the integrator again both acting as the output signal of the SQUID and the driver of the feedback current through the feedback coil of the front-end SQUID. The expression for the output voltage of this setup is given by

$$U = \frac{R_{fb}}{M_{fb}} \Delta\Phi_s = R_{fb} \frac{M_{is}}{M_{fb}} I_s. \tag{4.2}$$

4.1.3 Noise contributions of SQUIDs

SQUIDs enable highly sensitive measurements due to their very low but finite noise which can be split up into two dominant contributions,

$$S_{\Phi_\mathrm{s}}(f) = S_{\Phi,\mathrm{w}} + S_{\Phi,\mathrm{f}}, \tag{4.3}$$

where the two contributions are the white noise $S_{\Phi,\mathrm{w}}$ and a frequency-dependent pink noise contribution $S_{\Phi,\mathrm{f}}$.

White noise

The white noise contribution of a SQUID is theoretically well-understood and stems from the thermal noise of the two shunt resistors R_s. Using numerical calculations, [Tes77] and [Bru82] determined the optimal parameters for dc-SQUIDs with shunt resistors. With this optimization, the spectral power density for the apparent flux noise caused by the thermal noise in the SQUID can be expressed as

$$S_{\Phi_{\mathrm{S,w}}} \approx 18 k_\mathrm{B} T \frac{L_\mathrm{s}^2}{R_\mathrm{s}}, \tag{4.4}$$

where L_s is the inductance of the SQUID loop. In experiments, a typical value for the white noise of the SQUID is around $\sqrt{S_{\Phi_{\mathrm{s,w}}}} \approx 0.1\,\mu\Phi_0/\sqrt{\mathrm{Hz}}$. For this value, a SQUID temperature of $T = 150\,\mathrm{mK}$ (due to self-heating effects [Wel94]), an inductance of $L_\mathrm{s} \approx 100\,\mathrm{pH}$ and shunt resistances of $R_\mathrm{s} \approx 5\,\Omega$ were assumed.

Pink noise

The second noise contribution $S_{\Phi,\mathrm{f}}$ of SQUIDs is increasing towards lower temperatures, often behaving according to

$$S_{\Phi,\mathrm{f}} \propto \frac{1}{f^\alpha}. \tag{4.5}$$

This noise contribution is approximately proportional to the inverse of the frequency, with an exponent α taking values between 0.6 and 1.2 [Kem16]. The amplitude of the flux noise at 1 Hz is typically around $S_{\Phi,\mathrm{f}} \approx 5\,\mu\Phi_0/\sqrt{\mathrm{Hz}}$. The reason for this noise contribution remains partially unidentified, however, there are theories tracing the noise to magnetic moments on the surface of the SQUID loop [Koc07] or in the vincinity of the Josephson junctions [Kum16, De 17].

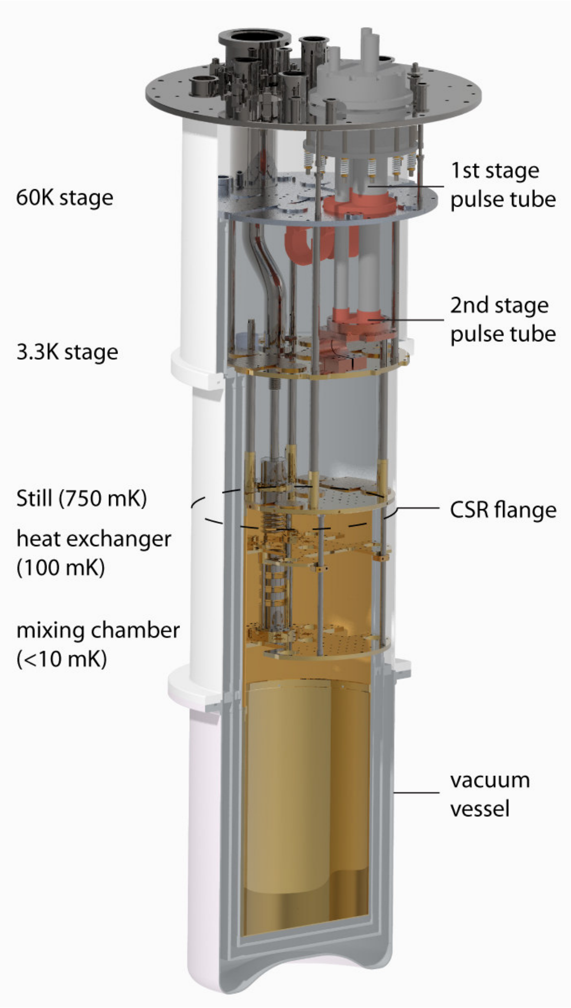

Figure 4.4: Cutaway drawing of the LD-series refrigerator by BlueFors used for this thesis. The cryostat frame and the ^{4}He compressor have been omitted in this drawing. The position of the CSR flange, as described in the text, is indicated by the dotted line.

4.2 Dilution refrigerator

As MMCs need to be run at temperatures below 0.1 K, they are most conveniently operated in ^{3}He/^{4}He dilution refrigerators. Their refrigeration principle is described in detail, for example, in [Lou74]. For this thesis and for later deployment inside the CSR, a BlueFors[2] LD series refrigerator was used. It uses a double-stage pulse tube for pre-cooling to 4 K. A sketch of the refrigerator is shown in figure 4.4. The refrigerator reaches a base temperature of below 7 mK and can be run for months without the need to supply any cryogenic liquids. There are additional temperature stages at

---

[2] BlueFors Oy, Arinatie 10, 00370 Helsinki, Finland

temperatures of approximately 100 mK, 750 mK, 3.3 K and 60 K. The cryostat itself rests on an air suspension inside its frame, separated from most vibration-inducing parts, to reduce the amount of vibration on the experimental setup itself.

As a special condition for this refrigerator, it needs to enable usage both as a stand-alone setup for detector testing and as an insert of the CSR ring. Therefore, the vacuum shield has an additional flange at the position marked with a dotted line in figure 4.4 to connect the refrigerator to the storage ring.

4.3 Data Acquisition

The output of each two-stage FLL-SQUID electronics is an analog signal. These signals are fed into analog-to-digital converters (ADCs). PAQs, a home-made software package, controls the data acquisition of the ADCs and writes the acquired data to disk. Both the used ADCs and PAQs, which was developed for MMC data readout by Daniel Hengstler [Hen17], will be explained in more detail in the following sections.

4.3.1 ADC

Within this thesis, two SIS3316 desktop digitizer modules[3] were used, each containing a total of 16 single-ended analog input channels. Each channel has a maximum sampling rate of 125 MHz with a 16 bit resolution and an effective resolution of 13.3 bit. It is possible to simultaneously acquire and transfer data to the measurement computer, either via an Ethernet cable or optical fiber, enabling a high data throughput. The clocks of multiple cards can be synchronized to each other.

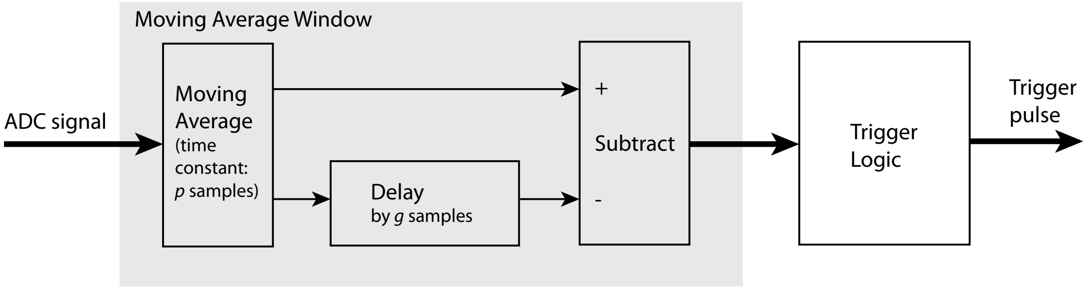

Figure 4.5: Schematical view of the trigger logics for one ADC channel. More details are given in the text.

To obviate the need for external signal filtering for triggering, the SIS3316 splits each digitized signal into two data streams in its FPGA: one for triggering, one for

---

[3] Struck Innovative Systeme GmbH, Harksheider Str. 102, 22399 Hamburg, Germany

acquisition, as shown in figure 4.5. The trigger is operated as a constant fraction discriminator with a Finite Impulse Response filter. A moving average with time constant p is applied to the incoming ADC signal in the stream used for triggering. Then, the signal is split up in two pathways. While one signal is passed directly to a subtractor, the other signal is delayed by g samples before being fed into the other connection of the subtractor. An exemplary original signal (black) and the two resulting signals (red, green) of the two pathways are shown on the left of figure 4.6, the resulting signal after the subtractor is shown on the right-hand side of figure 4.6. If the resulting signal passes a threshold that can be set via PAQs, the trigger is activated. The trigger time is set to the point where the subtracted signal returns to 50 %.

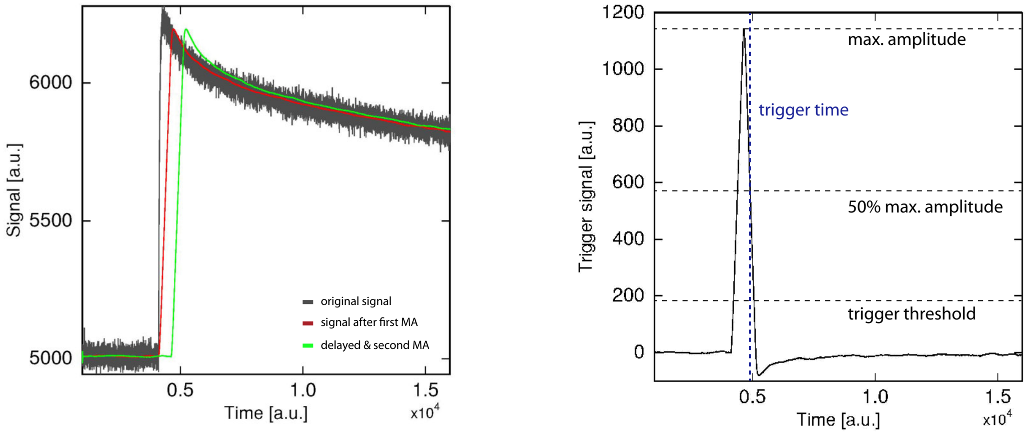

Figure 4.6: Left: Digitized signal (black), signal after the first moving average filter (red) and signal after delay (green). **Right:** Resulting signal after the subtractor. A trigger is activated if the amplitude of this signal crosses the chosen threshold.

4.3.2 PAQs

PAQS is a software package which allows for the parallel readout of presently 32-channel MMC-type detectors. Assuming each channel to read out a gradiometric pair of pick-up coils, PAQs can acquire and sort the signals of 64 MMCs. For that, PAQs directly controls the two 16-channel digitizer modules described in the previous section. The program was originally built to record all 64 pixels of a maXs30 detector, but the software package can be used more generally for all MMC-based detectors. It was created and is maintained by Daniel Hengstler [Hen17]. Its main properties will be summarized in this section.

Generally, PAQs directly controls the hardware of the digitizer modules. With this, a range of variables can be set, for example the number of samples recorded per second (sampling rate), how many samples are recorded per trace (sample length) and the amount of samples recorded before the trigger (pretrigger). Oversampling describes averaging over a certain number of recorded samples and writing the averaged value to the trace as one sample. With the used ADCs, the sampling rate can be chosen between 5.5 MHz and 125 MHz with values for oversampling between 4 and 512. The maximal sample lengths are 32768 total samples per trace with a maximum of 4096 samples in the pretrigger. As an additional option, a part of the signal around the trigger time can be written to disk with no oversampling applied at all. While the options above can only be applied globally to all channels, trigger levels can be set for every channel individually. The trigger engines of all channels can operate asynchronously. Recording untriggered baselines in fixed intervals is possible. Optionally, multiple reference channels can be recorded every time a trigger signal is received in any of the other, regular channels. Using the online fit functionality, a template fit can be applied during the measurement. The trigger can be suppressed for a set time after the previous trigger was recorded ("holdoff").

Recorded traces of the same ADC channel and the same polarity are saved in the same folder in groups of 1000 traces, collected in one zip-compressed folder. Each saved trace file consists of two parts: An ASCII-encoded header and the data, saved in binary format. The header contains basic information about the trace, such as as the time stamp when the trigger was activated or information on pulse shape and amplitude.

5. Development of the experimental setup

The development of the MOCCA detector, a highly granular large-area detector designed for use at the Cryogenic Storage Ring (CSR), the design of cryogenic and electronic platform to run MOCCA, the development of the micro-fabrication processes, and the software development enabling data analysis on the full detector were a major part of the work done for this thesis. One of the central properties of MOCCA is its very large active detection area of 4.5 cm ×4.5 cm covered by 64×64 pixels, which, to our knowledge, presently makes it the largest and most complex MMC-based detector. With MOCCA, energy resolutions of below 100 eV are achievable, as shown in sections 5.2 and 6.2.9.

In this chapter, design considerations and the design of the detector as well as the micro-fabrication processes will be described, with a focus on the newly developed processes such as through-wafer via process. Then, the developed readout infrastructure for MOCCA will be described. The planned setup for the operation at CSR will be outlined, and finally, central parts of the analysis software will be discussed.

5.1 Detector for CSR

MOCCA was specifically built for the detection of neutral molecule fragments at CSR. As formulated in chapter 2.3, a detector in this environment has to fulfill a range of requirements: it needs to be able to detect neutral massive particles at kinetic energies between 20 to 300 keV with spatial resolution and an energy resolution below 200 eV. Additionally, a multi-hit capability and a good timing resolution are required.

As a first iteration for CSR, the PIZZA detector was designed, decribed in detail in [Kam10, Gam13]. The active area of PIZZA is circular with a diameter of 36 mm. The 16 absorbers are shaped like 16 slices of a pizza with temperature sensors along the part of the circumference of each slice. The spatial resolution was achieved by analyzing the shape of the measured signal arriving at the sensor, using the heat diffusion inside the absorber to determine the radial position of the absorption of the incoming particle: The larger the rise time of the measured signal, the further away from the sensor the particle hit. Drawbacks were the limited possible rate and multi-hit capability of the design and a non-uniform energy resolution: as rise and decay times varied depending on where the particle hit the detector, the energy resolution of particles hitting the detector further away from the sensor was significantly worse, as can be derived from equation 3.27. For this reason, a design for a new detector, the MOCCA detector, was proposed in [Sch15].

5.1.1 General chip layout of MOCCA

The MOCCA detector, sketched in figure 5.1 and shown in a photograph of the setup in figure 5.14, is a pixel array consisting of 64×64 pixels[1] with an area of approximately $700\,\mu\mathrm{m} \times 700\,\mu\mathrm{m}$ each. The active area of the detector is $4.48\,\mathrm{cm} \times 4.48\,\mathrm{cm}$. With gaps of about $4\,\mu\mathrm{m}$ between absorbers, the filling factor[2] is $\simeq 99\,\%$. On two of the four sides, bondpads for the connection to the SQUIDs are placed. In total, MOCCA needs 32 front-end SQUIDs. The respective channels are labeled 1 to 16 for the rows and A to P for the columns. The detector is thermalized by through-wafer vias filled with gold, connecting the gold-covered back of the detector with the front at a total of 256 vias.

Along each edge of MOCCA, the distance between the active detector area and the edge of the chip is 5 mm. Within these margins, the bondpads and large area gold pads are located. The bondpads for the readout of the channels mirror the design used for the front-end SQUIDs produced within our group. Additional bondpads on the side are used for controlling the persistent current switch for the preparation of the persistent current creating the magnetic field in the coils of the detector, as described in [Sch15, Gam19]. Depending on how they are connected, they can be used to prepare current in the whole detector at once, in rows and columns separately or in blocks of four channels. The large gold areas can be used to ensure thermalization by connecting them to the chip carrier made of copper using gold bonding wires.

The MOCCA chip measures $5.48\,\mathrm{cm} \times 5.48\,\mathrm{cm}$. As the detector is fabricated on a three-inch wafer and the full diagonal of the detector slightly exceeds three inches, the corners of the detector are rounded. For overview, some of the general properties of the detector are summed up in table 5.1.

One of the design objectives for MOCCA was to minimize the number of SQUIDs needed for readout, as they tend to drive complexity and cost of the experiment. Potentially, an independent readout of each of the 4096 pixels could be achieved by using SQUID multiplexing techniques in the future. However, while already in development [Kem17], those techniques were not yet fully developed during the development of the MOCCA detector. Therefore, in order to read out 4096 pixels with just 32 SQUIDs, two principles were used: the line- and column-wise summing of the readout signals and a principle called hydra principle. Those two principles

---

[1] Within the context of MOCCA, one absorber is counted as one pixel.

[2] Filling factor is the ratio of the active area covered with absorbers, i.e. the ratio of the area where impinging particles are measured, in relation to the full detector area.

will be explained in the next two sections.

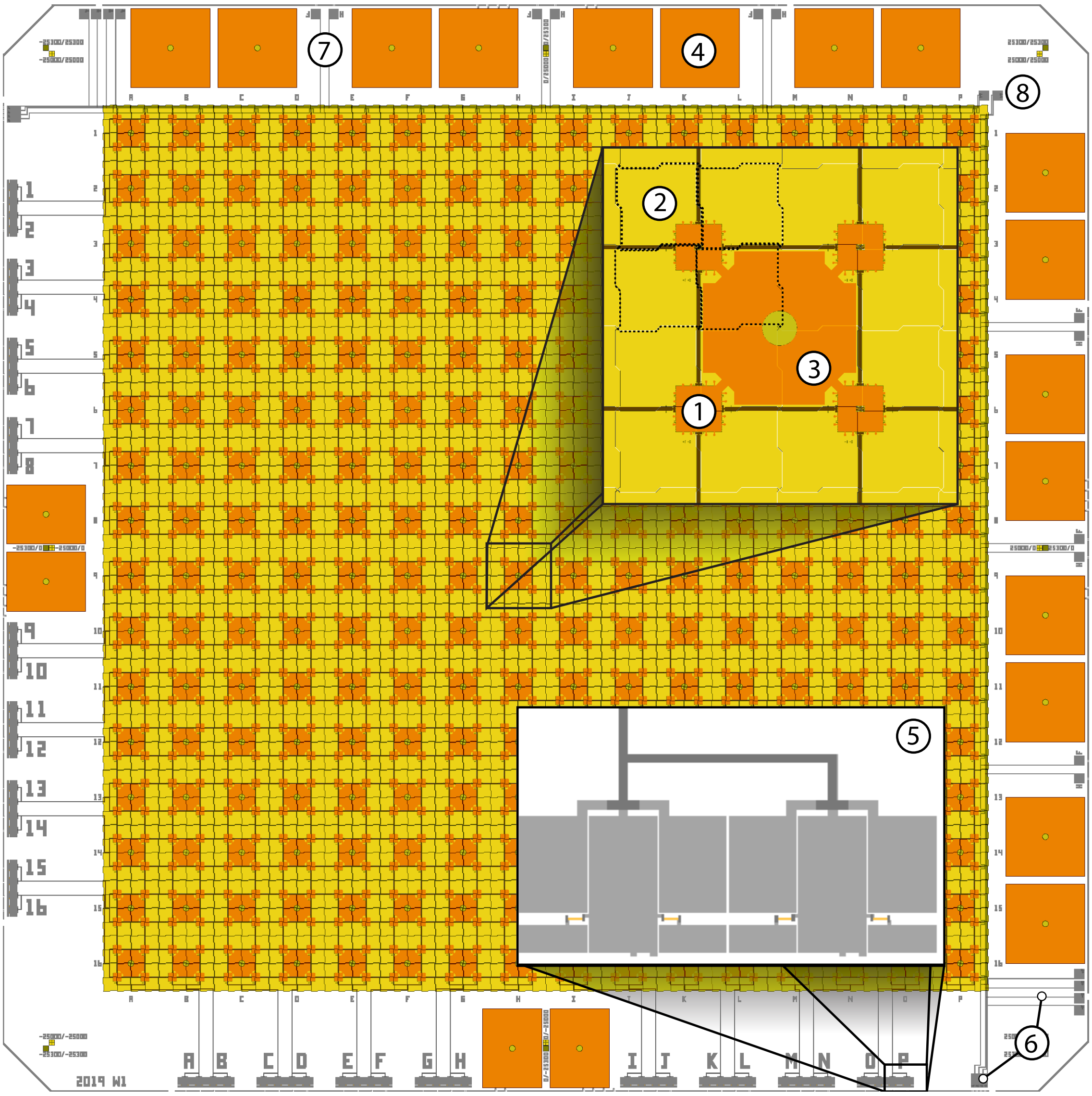

Figure 5.1: Drawing of the detector design for MOCCA. Pictured is the square chip with a side length of 5.48 cm and two enlarged views, one showing the area of approximately four by four absorbers and one showing the redundant bond pads for one channel. The absorber layer is pictured as yellow and semi-transparent. Indicated are (1) a sensor, (2) one absorber, (3) the thermalization pad between four sensors with the through-wafer via in the middle (orange), (4) a gold pad on the side of the chip for thermalization, (5) the bond pads for connecting the front-end SQUIDs, (6) the bondpads for connection to the persistent current switch, (7) bondpads that can be used to selectively inject persistent current into groups of four channels, (8) bondpads that, when connected, allow the operation of all persistent current switches of the complete detector with just one current source.

5.1.2 Hydra principle

For the general introduction of the working principle of MMCs in chapter 3.1, it was assumed that every sensor is connected to a single absorber. While this holds true for many MMC designs for high resolution x-ray spectroscopy (see, for example, [Hen17, Gas17, Sch19]), the number of absorbers per sensor can be increased using the so-called Hydra principle, pioneered by a group at the NASA Goddard Space Flight Centre [Por11] and named after the many-headed serpent of Greek mythology. A sketch of the hydra principle is shown in figure 5.2: One single temperature sensor is connected to n absorbers. By varying the thermal conductances g_i between each absorber $i, i \leq n$, and the sensor, signals from different absorbers can be distinguished from each other: Assuming that heat distribution in the absorber itself happens on a significantly faster timescale than the thermalization between absorber and sensor through g_i, the different thermal conductances lead to different signal rise times. During data analysis, this difference in rise time can be used to assign the measured pulse to the absorber where the absorption of the particle took place.

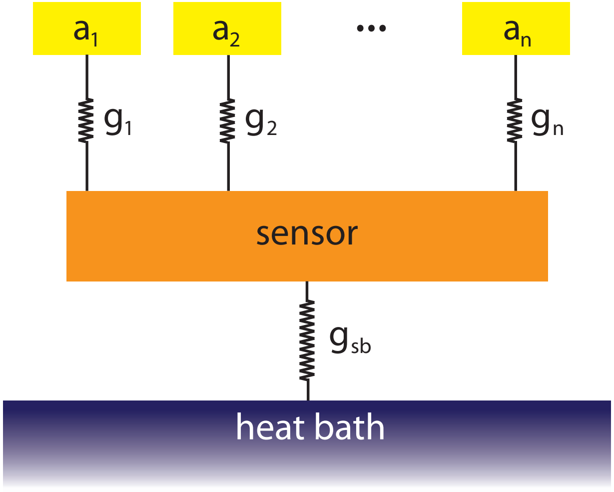

Figure 5.2: Schematic view of the hydra principle with n absorbers a_i, $i \leq n$, coupled to the sensor with the thermal conductances g_i. The sensor is connected to the thermal bath via the thermal conductance g_{sb}.

Using this principle introduces more complexity to the data analysis: to achieve the full spatial resolution of the detector, the pulse shape of each recorded trace has to be analyzed. As the energy resolution depends on the rise time (see eq. 3.27), the achievable energy resolution for the different pixels of the hydra will slightly differ. If, for example, the signal rise times of two pixels differ by a factor of 4, the fundamental energy resolution of those pixels differs by a factor of $\sqrt[4]{4} = 1.4$. Also, the complexity of the pulse shape is increased, as shown in the calculation of the point spread function for a 4-pixel hydra in [Gam19]. However, the hydra principle offers the ability to increase the granularity by a factor n while degrading the energy resolution only by about $\sqrt{n}$. As this does not increase the need of sensors and, thereby, the number of SQUIDs, the hydra principle can lead to a significant increase in spatial resolution and pixel number of large-area detectors.

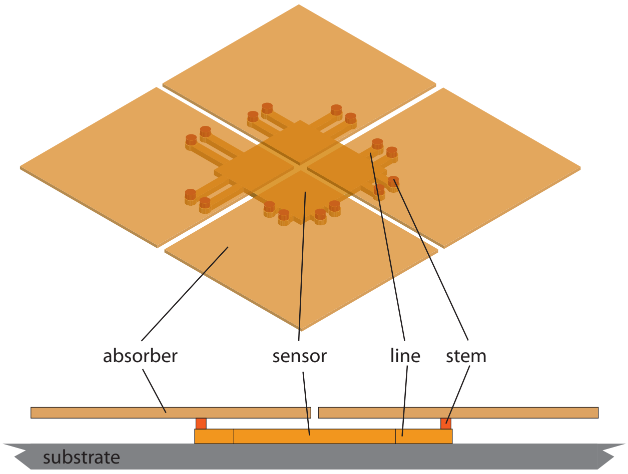

Figure 5.3: Sketch of the hydra design in sectional view and three dimensional view with transparent absorbers of one sensor with four absorbers, connected with four different thermal links. The lengths of the lines between landing pad and sensor are exaggerated for illustration purposes.

For the latest MOCCA design, it was decided to use $n = 4$ absorbers per sensor, designing the rise times to be 4 µs, 8 µs, 12 µs, and 16 µs. The realization of this design is shown in figure 5.3: Each absorber rests on a total of four so-called stems. Those stems are in direct contact with a circular landing pad fabricated from the same material as the sensors. The contact area between landing pad and absorber is circular with a diameter of 15 µm each. The thermal conductance between sensor and absorber is defined by the length of the line between sensor and landing pad. The expected rise time can be calculated using equation 3.22, the respective lengths used in the latest MOCCA design were adjusted using data from earlier MOCCA versions, using four landing pads per absorber with distances of 2, 10, 20 and 30 µm between pad and sensor. For future detectors, a higher number n of absorbers per sensor can be chosen. In a recent work of the group at Goddard Space Flight Center [Ste19, Yoo20], a proposed MMC with a 25-pixel hydra was shown to work well.

5.1.3 Summed line- and columnwise readout

The 32 × 32 sensors of the MOCCA detector are arranged in a square grid with a center-to-center distance of 1.4 mm. In order to minimize the number of SQUIDs

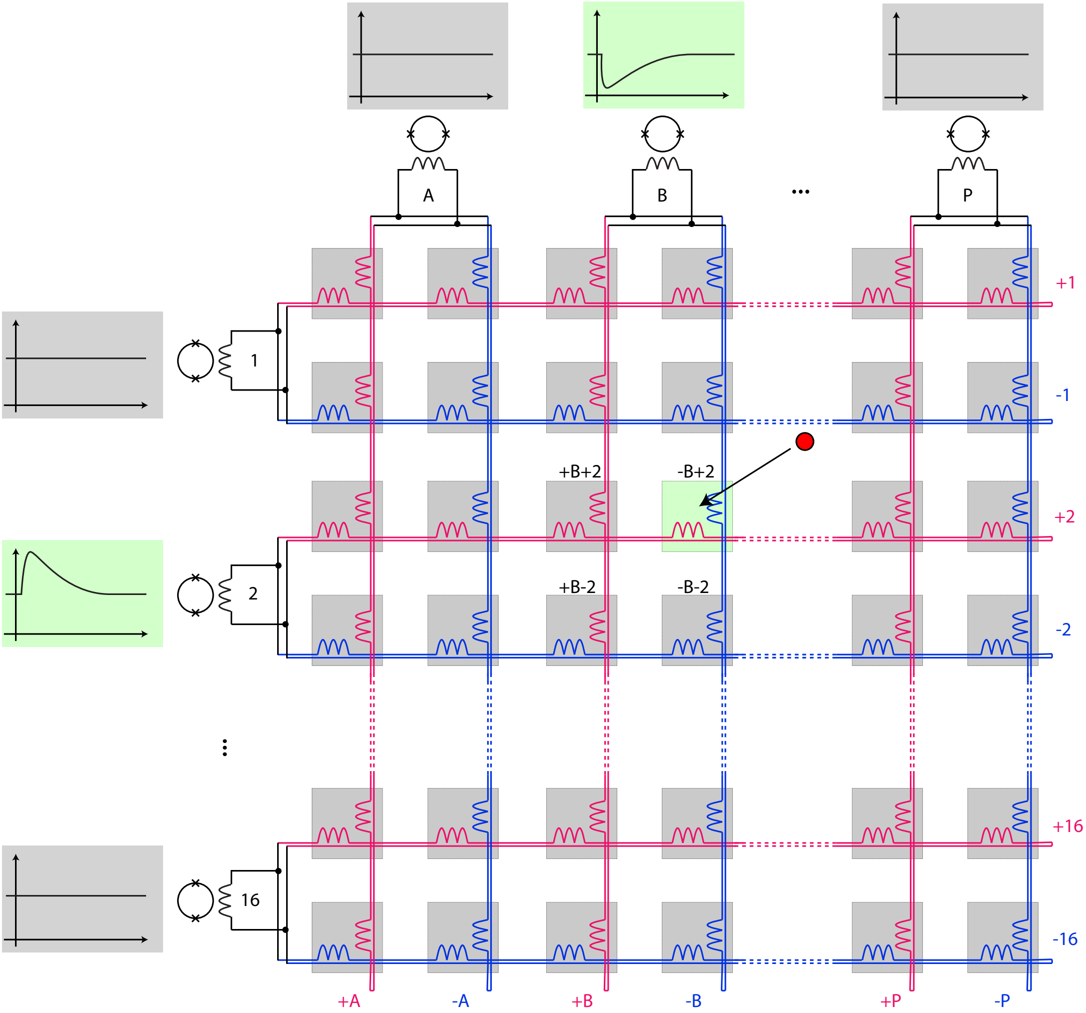

Figure 5.4: Illustration of the row- and columnwise readout scheme of the sensors. Each SQUID is labeled with its channel name. Lines leading to a signal with positive polarity in the SQUID are drawn red, lines leading to a negative signal are drawn blue. For illustration, the resulting signals from a hit in channel B with negative polarity and channel 2 with positive polarity are shown. The respective sensor is named −B+2.

needed, a summed line- and columnwise readout is used, i.e. each hit by a particle leads to a signal in the corresponding line and in the corresponding column. By matching those two signals to each other, the sensor where the particle hit the detector can be identified. In the given example in figure 5.4, the particle absorbed in one of the absorbers of sensor −B+2 leads to a negative signal in channel B and a positive signal in channel 2, which are measured coincidentally.

The design used to achieve this is based on the basic MMC principle from figure

3.6 and is shown in figure 5.4. In MOCCA, each line[3] of 32 sensors is read out by pick-up coils, connected in series to each other. Analogous to figure 3.6, the lines are paired up and connected with one SQUID per pair, where a hit in one line leads to a signal of positive polarity, while a hit in the other line of the pair leads to a signal of negative polarity. In figure 5.4, this is symbolized by red (positive polarity) and blue (negative polarity) lines. On the detector itself, each sensor is identified with the respective channel combination and signal polarity, as indicated for four sensors of channels B and 2 in the figure.

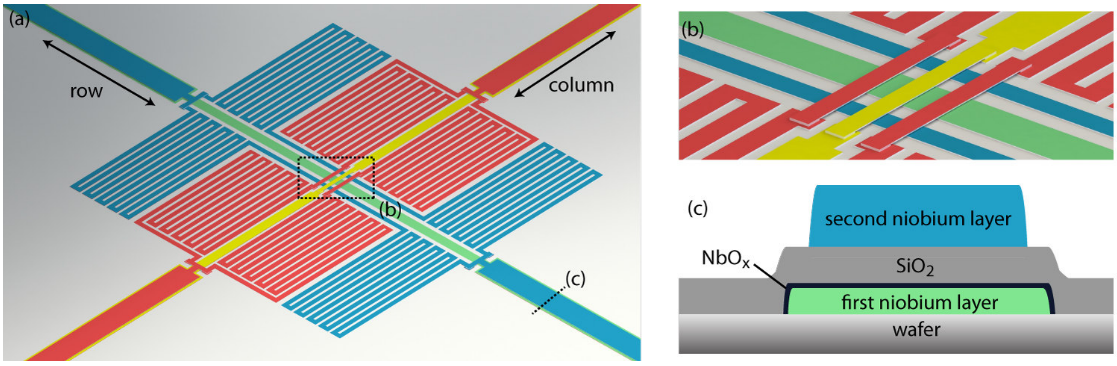

Figure 5.5: (a) Design of the meander-shaped pick-up coils under one sensor. The row connections are shown in blue and green, the column connections are shown in yellow and red. (b) Enlarged view of the crossing in the center between the meander-shaped pick-up coils. (c) Cut through the connection line between meanders. Layer thicknesses are drawn to scale. The colors of the niobium layers refer to the colour of the lines in figure (a).

This means that each sensor has to be read out by two galvanically separated pick-up coils. The design used to achieve this is shown in figure 5.5(a). The pick-up coil is realized using niobium lines with a width of 5 µm. As can be seen in the figure, the coils under each sensor are split up into several sub-coils. This has two reasons: Firstly, this reduces the amount of cross-talk between columns and rows. Secondly, almost all lines inside the pick-up coil are redundant; if, during the fabrication of the detector, one line should be damaged and interrupted within one of the sub-coils, this does not interrupt the electrical circuit at large. As shown in figure 5.5b), in the center of the pick-up coil, the row- and the column-lines cross each other, with one of the two passing in the layer of the meander in the first niobium layer, while the other crosses in a bridge-like arrangement in the second niobium layer.

As this design drives up the total inductance of the detector channels, the signal size is smaller compared to other MMC-type detectors, which also contributes to MOCCA having a worse energy resolution than other MMC-type detectors. However,

---

[3] Here, line stands for both column or row.

this can be neglected compared to the degradation of linewidth due to random defect production by the massive particles, as described in section 3.6.

5.1.4 Layout of one MMC unit

The three-dimensional layout of one MMC unit, comprising one sensor, four absorbers, and a thermalization pad shared by a total of four sensors, is shown in figure 5.6. The full MOCCA detector is comprised of a total of 1024 of those MMC units, arranged in a grid with a center-to-center distance of 1.4 mm.

The lines used for connecting the pick-up coils are shown in figure 5.5(c). They are realized as two-layered co-parallel connection lines, which we call micro-strip-lines here, fabricated from niobium. In between the two niobium layers, electrically isolating Nb_2O_5 and SiO_2 is used. As outlined in [Sch15], these connections add very little additional parasitic inductance to the total inductance of a line and couple weakly to external magnetic fields.

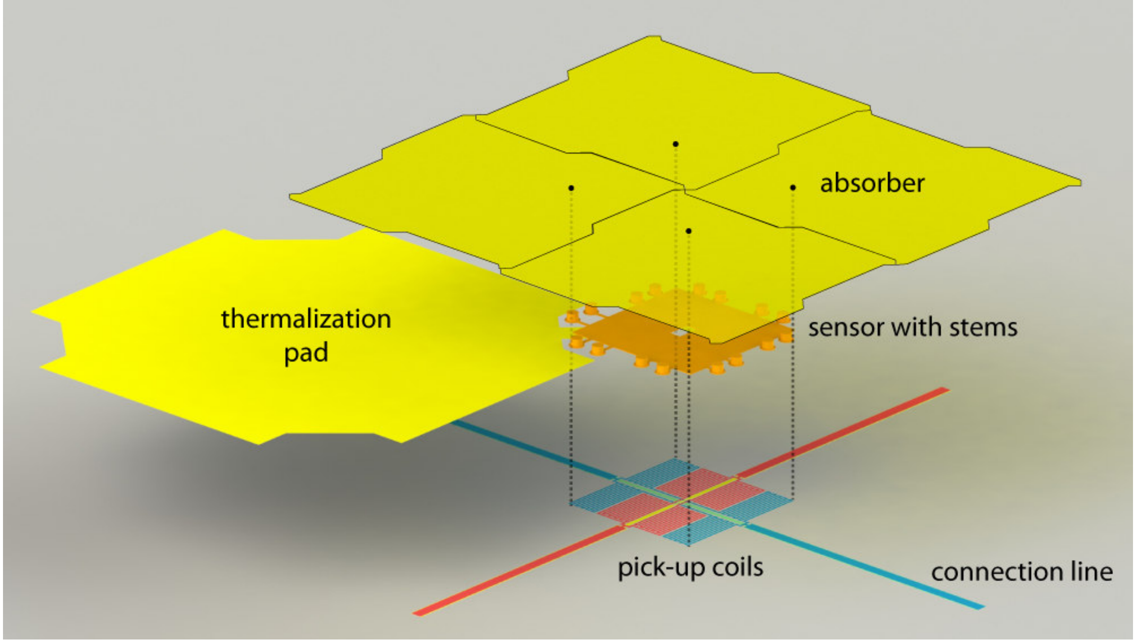

Figure 5.6: Exploded view of one of 1024 MMC hydra units of MOCCA. The area parallel to the absorber is drawn to scale, heights are not to scale. The absorbers are shown transparent for better overview.

The sensor is deposited on top of the meander-shaped pick-up coil, covering its full area with the exception of a cut-out in its center. The cut-out ensures that there is no electrical connection between the sensor and the upper niobium layer of the bridge-like lines in the middle of the pick-up coil.

Design values		**SQUID parameters**	
Pitch p (pick-up coil)	9 µm	$L_{\text{input, SQUID}}$	1.7 nH
Line width w (p.-u. coil)	5 µm	coupling constant $\mathrm{k_{is}}$	0.69
Absorber area A_{abs}	$\approx (700\,\mu\text{m})^2$	**SQUID noise**	
Absorber height h_{abs}	4 µm	exponent of 1/f noise	0.9
Sensor area A_{sens}	$(397\,\mu\text{m})^2$	SQUID noise at 1 Hz	$5 \times 10^{-6} \frac{\Phi_0}{\sqrt{\text{Hz}}}$
Sensor height h_{sens}	2 µm	SQUID, white noise	$0.2{\times}10^{-6} \frac{\Phi_0}{\sqrt{\text{Hz}}}$
Signal rise times τ_1	4 µs, 8µs, 12 µs, 16 µs	Mutual induct. $\mathrm{M_{is}}$	$(12.5\,\mu\text{A}/\Phi_0)^{-1}$
Signal decay time τ_2	1 ms	**Other parameters**	
L_{ch}(one MOCCA ch.)	8.8 nH	Er concentration in $\underline{\text{Ag}}$:Er	395 ppm
L_{sl} of conn. lines	21.7 nH/m	Bond wires induct. $\mathrm{L_{wire}}$	500 pH

Table 5.1: List of MOCCA properties, as designed for the latest version of MOCCA used in this thesis.

The outline of the absorbers follows a jigsaw pattern instead of completely straight lines. This is to avoid direct impact of particles on the niobium lines between the pick-up coils. Between the absorbers, a gap of 4 µm is left. With the absorber side length of approximately 700 µm, this amounts to a total filling factor of $\simeq$ 99 %.

To keep the sensor at the base temperature of the refrigerator, groups of four sensors are coupled to one common thermalization pad via a gold line. This gold line defines the thermal contact between sensor and thermal bath and, by that, the decay time of the signal. The thermalization pad is thermally connected to the backside of the wafer using a gold-filled through-wafer via, described in section 5.3.2.

5.2 Simulation

As the properties of MMCs are well-understood, it is possible to simulate and optimize the expected energy resolution for a given application and, on that basis, calculate optimal detector parameters. This can be carried out by a script written by Matthew Herbst [Her22], based on a script developed by several members of the group [Sch00, Fle03, Fle05]. Parameters that can be optimized are sensor area A and height h, Erbium concentration in the sensor x, the prepared persistent current I_0 in the pick-up coils and the pitch of the pick-up coil p.

For MOCCA, the absorber and sensor area are both derived from geometrical considerations and are considered as given. The height of the absorber h_{abs} was chosen to be 4 µm as this thickness will be sufficient to stop 6 keV X-ray photons as well as atomic ions with kinetic energies up to 300 keV. The value of 4 µm is

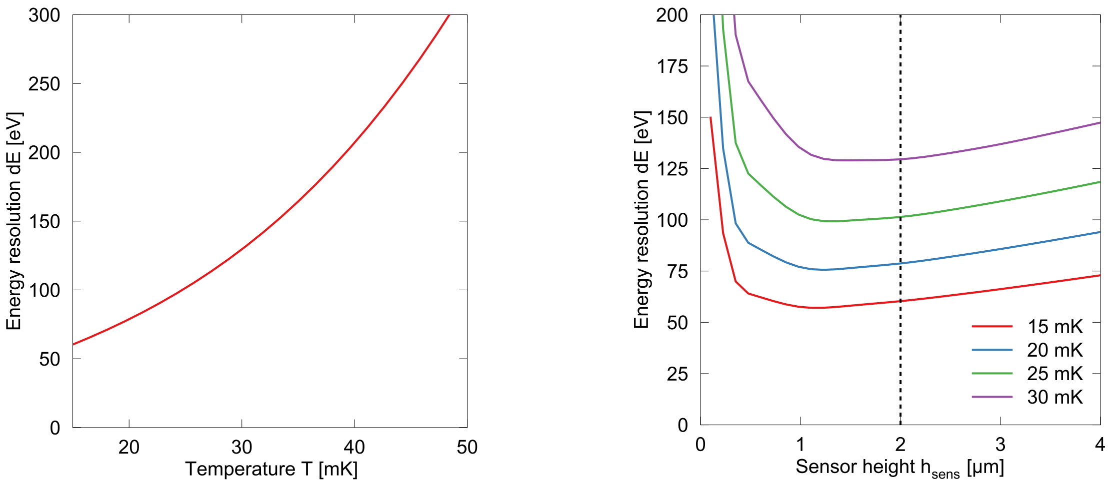

(a) Energy resolution as a function of the temperature T of the detector for the range of 15 to 100 mK.

(b) Energy resolution as a function of the sensor height h_{sens} of the sensor for temperatures of 20, 30 and 40 mK.

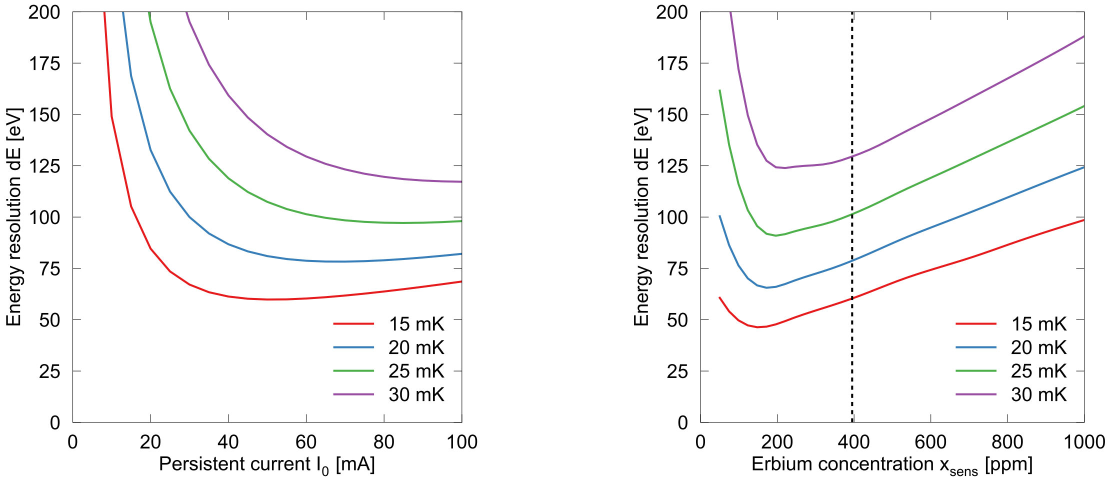

(c) Energy resolution as a function of the prepared supercurrent I_0 for temperatures of 20, 30 and 40 mK.

(d) Energy resolution as a function of the Erbium concentration in the sensor x_{sens} for temperatures of 20, 30 and 40 mK.

Figure 5.7: Effective energy resolution for different varied parameters. If not stated differently, values from table 5.1 were used as a basis for the calculation, and I_0 was assumed to be 60 mA. For (c) and (d), the actual values from the latest MOCCA design are highlighted.

higher than the 3 µm minimum derived from the attenuation length of 6 keV X-ray radiation, but the change in energy resolution for the additional thickness is only 10 %. The erbium concentration is determined by the available target for sputter deposition.

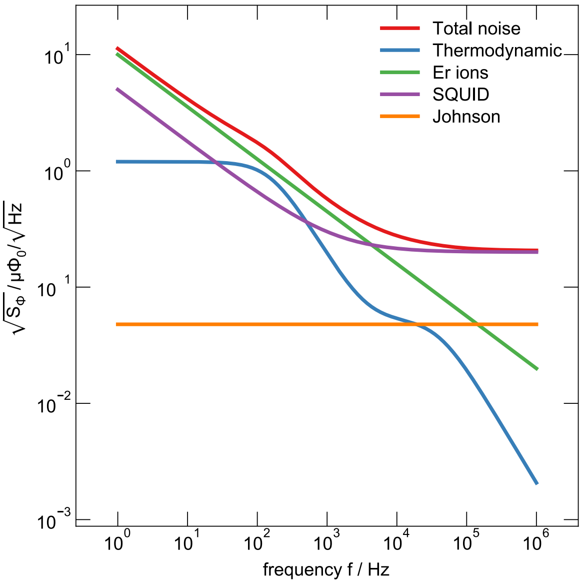

Figure 5.8: Total noise and the most important noise contributions for a MOCCA detector at a temperature of 20 mK and $I_0 = 60\,\mathrm{mA}$. For calculation, the parameters listed in table 5.1 were used.

The expected energy resolution for different temperatures T, persistent current values I_0, Erbium concentrations x in the sensor and sensor heights h are given in figure 5.7. The parameters used for the simulation are described in table 5.1. The temperature has a major influence on the resolution of the detector. For sensor height, Erbium concentration and current, the energy resolution is worst at small values, but large parameter spaces exist with very little dependency between the respective variable and ΔE.

Assuming the detector will be at 20 mK during measurements and using the values outlined in table 5.1, the calculated possible energy resolution for MOCCA is 46 eV. The best energy resolution achievable with MOCCA V8w1, the latest produced MOCCA, is 60 eV FWHM at 15 mK and 78 eV FWHM at 20 mK. The spectral dependency of the different noise contributions from equation 3.31 is shown in figure 5.8, together with the simulated total noise. While the SQUID noise dominates the behavior for higher frequencies, the noise at low frequencies is dominated by the noise of the erbium ions.

5.3 Micro-fabrication process development

The detectors designed and used within the scope of this thesis were completely fabricated in the ISO 5 class[4] cleanroom of our institute. As the production process for an earlier version of the MOCCA detector was already described in detail in [Gam19], this chapter will only give an overview over the available processes. The production process for gold-filled through-wafer vias was developed within the work for this thesis, building on earlier results by [Hen17, Sch19, Gam19] and will be described in more detail.

Inside the cleanroom, a range of different processes is available. All available machines can be used with wafers up to a diameter of 3 inch, some machines can also be used for larger wafers. Wafers are supplied by SiMat[5] and Siegert Wafer[6], have a diameter of 3 inch, a thickness of 375 µm, and a resistivity of $> 10\,\mathrm{k\Omega cm}$. At least one side of each wafer is polished. All wafers have a thermal oxide layer of around 240 nm thickness on both sides, created by exposing the wafers to an oxygen atmosphere in a heated furnace.

For defining micrometer-sized structures, a range of different photoresists was used, with a lot of processing based on the resist AZ 5214E, an image-reversible positive resist for layer thicknesses between one and two micrometers, and AZ 4533 and AZ 4562, positive photoresists with high chemical resistance and larger resist thicknesses of up to 10 µm. All used photoresists are distributed by MicroChemicals[7] and produced by Merck[8]. Resists are applied using spin-coating. The mask-less aligner MLA 150[9] was used to write structures directly into the resist, using a 375 nm-laser. For deposition of metallic and non-metallic layers, two different sputtering machines are available: one UHV sputtering system by DCA[10], and a HV sputtering system by Alcatel[11]. For plasma etching, a Sentech SI 500 C[12] was used. This machine is described in more detail in the next section. Available wet-etching processes are a potassium-iodine solution for gold etching containing I_2, KI and H_2O in a relation of $1 : 4 : 40$, and an aluminum etch made from a mixture of phosphoric acid (H_3PO_4), nitric acid (HNO_3), acetic acid (CH_3COOH) and water in a mixing ratio

---

[4] ISO 5 is a classification after the norm ISO 14644 and limits the number of particles in one cubic meter of air in dependance of the particle size.

[5] Si-Mat Deutschland, Silicon Materials, Viktor-Frankl-Strasse 20, 86916 Kaufring, Germany

[6] Siegert Wafer GmbH, Charlottenburger Allee 7, 52068 Aachen, Germany

[7] MicroChemicals GmbH, Nicolaus-Otto-Strasse 39, 89079 Ulm, Germany

[8] Merck KGaA, Frankfurter Str. 250, 64293 Darmstadt, Germany

[9] Heidelberg Instruments Mikrotechnik GmbH, Tullastrasse 2, 69126 Heidelberg, Germany

[10] DCA Instruments Oy, Vajossuonkatu 8, 20360 Turku, Finland

[11] Alcatel SCM601, Alcatel Vacuum Technology France SAS, merged to Pfeiffer Vacuum SAS, 98 Av. de Brogny, 74009 Annecy, France

[12] SI 500 C, Sentech Instruments GmbH, Schwarzschildstrasse 2, 12489 Berlin, Germany

of 16:1:1:2. A custom-built setup allows for electroplating high-purity gold layers, enabling thicknesses of up to 100 µm. The used gold-plating solution is Technigold 25 ES ready-to-use (RTU)[13].

In order to fabricate structures, two general principles can be distinguished: Etching processes and lift-off processes.

- For etching processes, first, the desired material is deposited over the full surface of the wafer. Then, photoresist is applied and patterned in a way that the resist covers all structures of the design. Through dry (plasma) or wet etching methods, all other material is then removed.
- In the lift-off process, first, resist is applied on the whole wafer and structured. Resist will cover all areas that are supposed to be free of material later. Then, the material is applied over the whole wafer. When this wafer is put in solvent, the resolving resist will release the material on top of the resist, removing it from the wafer. Typically, submerging the wafer in an ultrasonic bath is used to completely remove all spare material.

While etching processes generally lead to smoother structure edges and clean removal of materials, they have to be tuned to selectively etch the desired material. Lift-off processes can be generally applied for a range of many materials, but due to sidewall coverage, wing-like structures can form along edges of structures.

ICP-RIE

Reactive ion etching with inductively coupled plasma (ICP-RIE) is a method to selectively remove layers of material. Inside an ICP-RIE machine, a plasma is continuously supplied with a process gas, creating ions. These ions are accelerated towards the wafer to be etched and react with the material on the substrate, which is referred to as the chemical component of the etch process, or remove material by sputtering it off, called the physical component. Residual gas is continuously removed from the reaction chamber with a turbo-molecular pump. An important process parameter is the selectivity of the plasma, describing the etch rate of the desired material in relation to materials used as an etch mask, for example photoresist or aluminum.

For the etching process development described in the next section, an SI 500C dry etching machine from Sentech was used. Over time, a range of processes has been developed in our group to dry etch different materials. Currently, the machine is used for etching Nb, Au, Si and SiO_2. Additionally, it can be used for a cleaning

---

[13] Technic Deutschland GmbH, Glärbach 2, 58802 Balve, Germany

Material	Process gas flow	parameters	etch rate
Au	145 sccm Ar	$T = 5° \mathrm{C}$, $p_{\mathrm{proc}} = 1.5\,\mathrm{Pa}$, $P_{\mathrm{ICP}} = 200\,\mathrm{W}$, $P_{\mathrm{HF}} = 200\,\mathrm{W}$	$> 10\,\mathrm{nm/min}$
Nb (1)	15 sccm SF_6	$T = 5° \mathrm{C}$, $p_{\mathrm{proc}} = 2\,\mathrm{Pa}$, $P_{\mathrm{ICP}} = 100\,\mathrm{W}$, $P_{\mathrm{HF}} = 50\,\mathrm{W}$	$> 55\,\mathrm{nm/min}$
Nb (2)	15 sccm SF_6, 5 sccm O_2	$T = 5° \mathrm{C}$, $p_{\mathrm{proc}} = 2\,\mathrm{Pa}$, $P_{\mathrm{ICP}} = 100\,\mathrm{W}$, $P_{\mathrm{HF}} = 50\,\mathrm{W}$	$> 15\,\mathrm{nm/min}$
Si	125 sccm SF_6, 12 sccm O_2	$T = -105° \mathrm{C}$, $p_{\mathrm{proc}} = 0.8\,\mathrm{Pa}$, $P_{\mathrm{ICP}} = 650\,\mathrm{W}$, $P_{\mathrm{HF}} = 10\,\mathrm{W}$	$\simeq 2\,\mu\mathrm{m/min}$
SiO_2	50 sccm CHF_3	$T = 15° \mathrm{C}$, $p_{\mathrm{proc}} = 0.8\,\mathrm{Pa}$, $P_{\mathrm{ICP}} = 500\,\mathrm{W}$, $P_{\mathrm{HF}} = 450\,\mathrm{W}$	$> 70\,\mathrm{nm/min}$
organic material	99 sccm O_2	$T = 5° \mathrm{C}$, $p_{\mathrm{proc}} = 2\,\mathrm{Pa}$, $P_{\mathrm{ICP}} = 600\,\mathrm{W}$, $P_{\mathrm{HF}} = 0\,\mathrm{W}$	n.a.

Table 5.2: Overview over dry etch processes and process parameters used within this thesis: the reaction chamber pressure p_{proc}, the process temperature T, the ICP power source P_{ICP} and the high frequency power source P_{HF}. The etch rates represent the minimum values achieved with the institute-own machine for the given parameters. The oxygen plasma for removal of organic material is typically used for cleaning. For that reason, no etch rate is given, as it can vary and initial layer thicknesses are generally not known for the process.

process called ashing where organic materials are removed by an oxygen plasma. All these processes have a different chemistry and, for that reason, need different process pressures, temperatures and supplied powers and have different etch rates. An overview over the parameters and the used gases is given in table 5.2. The table also lists the cryogenic deep-etching process for silicon, which was developed within this thesis. The process and its parameters are described in more detail in section 5.3.2.

5.3.1 General process overview

An overview of all processes during the fabrication of a MOCCA detector is given in table 5.3. In the following section, these processing steps will be described in detail, referring to the layer numbers as defined in this table.

To fabricate a MOCCA detector, first, a 250 nm layer of niobium is deposited on the wafer, followed by an in-situ deposition of 100 nm Au (layer 1). This additional gold layer was added as a protection layer for the niobium. As described in [Kra20], adding this sacrificial gold layer and using the etching process named Nb (2) in table 5.2 yielded the best superconducting connections between the first and the

Layer	Structures	Material	Process	Resist (AZ)
1/Nb1	superconducting coils and connections	250 nm Nb, 100 nm Au	Sputter deposition and plasma etch, wet etch of gold	5214E
2/Iso1a	electr. isolation, anodization	50-60 nm Nb_2O_5	Anodization	5214E (IR)
3/Iso1b	electr. isolation, first step	175 nm SiO_x	Sputter deposition and lift-off	5214E (IR)
4/Iso1c	electr. isolation, second step	175 nm SiO_x	Sputter deposition and lift-off	5214E (IR)
5/Heat	Heating resistances	160 nm AuPd	Sputter deposition and lift-off	5214E (IR)
6/NbEF	Remove anodization connections	-	Nb plasma etch	5214E
7/Nb2	superconducting connections, second layer	600 nm Nb	Sputter deposition and lift-off	5214E (IR)
8/Vias	Au-filled through-wafer vias	...	...	see table 5.4
9/Iso2	Isolation layer	350 nm SiO_x	Sputter deposition and lift-off	5214E (IR)
10/Sens	Sensors	1.5 to 2 µm Ag:Er, 100 nm Au	Sputter deposition and lift-off	nLof 2070
11/Stems	Stems for absorbers	100 nm Au	Sputter deposition	AZ4533
12/Abs	Absorbers	4 µm Au	Electroplating, Au plasma etch	AZ4562

Table 5.3: List of cleanroom processes used for fabrication of the MOCCA detector. The processes for producing through-wafer vias contain more sub-processes and are described in separate sections. IR refers to the respective resist being used as an image-reversal resist.

second niobium layer, i.e. carrying the highest supercurrents without quenching. After structuring the resist, first, the gold is removed using dry etching. Subsequently, the niobium is etched without breaking the vacuum in between. Then, the resist is removed and the gold layer on top of the first niobium layer is etched using the gold wet etch.

In order to electrically isolate the first niobium layer with respect to later metallic layers, a total of three isolation layers (layer 2 to 4) are applied. Bond pads and areas where the first and the second niobium layer should be connected, which are not supposed to be isolated, are covered with photoresist. First, the niobium layer is anodized (layer 2) by immersing the wafer in anodizing solution and applying 25 V to the niobium structures. Anodization at this voltage creates a Nb_2O_5 layer of about 50 to 60 nm thickness that appears deep blue to the eye. For this step, all niobium structures of the first layer have to be electrically connected to each other. This requires additional auxiliary niobium lines that are removed in a later process.

The second and third isolation layer both consist of sputter deposited SiO_x with a thickness of 175 nm each (layer 3 and 4). Both are fabricated using a lift-off process and AZ5214E as photoresist. While this layer could theoretically be sputtered as one layer of 350 nm thickness, the reason for splitting the layer into two separate layers is twofold: Firstly, during lift-off, sharp wing-like structures at the edges of the SiO_x structures can be created. Those can cut off structures in following layers. By reducing the layer thickness of the SiO_x, these wings are also reduced. Secondly, this additionally contributes to ensure a pinhole-free isolation.

Afterwards, a gold-palladium layer (layer 5) is sputter deposited and structured using a lift-off process. This layer is used to define the resistors used for the persistent current switch. After that, the auxiliary niobium connections used during anodization are removed (layer 6) using the plasma etching process named Nb (1) in table 5.2.

The second niobium layer for superconducting connections is deposited (layer 7). To ensure that the connections between the first and the second niobium layer can carry a satisfactory current, about 40 nm of the first niobium layer are removed by argon ion bombardment in-situ before depositing the second one. This ensures the removal of oxide and any solvant-resistant films created during the processing [Kra20].

The processes for the fabrication of gold-filled through-wafer vias, the thermalization connections on the front side and the gold backside of the detector (summed up as layer 8) were developed within this thesis and are described in more detail in section 5.3.2.

After this, another SiO_x isolation layer (layer 9) is sputter deposited on the wafer, followed by a lift-off. It isolates the second niobium layer with respect to sensor and absorbers. On top of this layer, the sensor layer (layer 10) is deposited, using a lift-off process with the negative resist AZ nLof 2070 to achieve the desired sensor thickness. The large foil resulting from most of the deposited Ag:Er being removed during lift-off can be used for magnetization measurements in order to check the Erbium content of the sensor. On top of the Ag:Er layer, a 100 nm Au layer is added to prevent oxidation.

For the stem layer (layer 11), the wafer is structured using AZ4533, leaving the locations of the stems resist-free. To yield a soft incline around the stems instead of a steep resist wall, the wafer is baked for 120 s at 120°C. Under those conditions, a thermal reflow of the resist occurs. A gold layer with a thickness of 100 nm (the so-called seed layer) is then sputter deposited on the resist.

After that, a layer of AZ4562 is applied. This resist is used to define the areas where, during the subsequent electroplating, no gold should be deposited, i.e. the slits separating the absorbers. The soft bake of the resist is done at a temperature of 80° C to avoid wrinkling of the seed layer, caused by melting of the photoresist underneath. Then, the seed layer is used as a cathode for electroplating, and the absorbers are electroplated up to the desired thickness (layer 12). After the electroplating, the wafer is left in solvent for at least 24 hours to ensure complete removal of the resist, also below the absorbers. In order to avoid deformation of the absorbers, the wafer was not subjected to any ultrasonic bath during cleaning; instead, the gold skin between the absorbers, a residual from the seed layer, was removed with an argon-based dry etching plasma on the cleaned wafer.

5.3.2 Through-silicon vias

Through-silicon vias are vertical connections through a silicon wafer or chip to enable eletrical connection between the front and back side of the wafer. Historically, they have been used in the semiconductor industry to achieve high-density chip-to-chip connections by enabling electrical through-chip connections. For MMCs, gold-filled through-silicon vias can be used to provide homogeonous thermalization over the whole MMC detector by connecting sensors to the gold-covered back of the detector. This minimizes temperature gradients over the detector and ensures a defined thermal contact between sensor and heat bath, which is especially desirable for larger detectors such as the MOCCA detector and high-resolution detectors [Möh15, Hen17]. While deep-etching on wafers was already used on earlier detectors [Hen17, Sch19] and a test wafer was produced with gold-filled vias [Gam19], no MMC was equipped with gold-filled through-wafer vias so far. Also, etching rates were about a factor 10 to 20 slower than comparable rates from literature for the same type of etching machine [Sök09, Sök10, Ste14], while the form of the sidewall of the holes varied from process to process . Within this thesis, in cooperation with Freerik Forndran [For19], a reliable, comparably fast and reproducible process for producing gold-filled through wafer vias was developed and successfully applied to the MOCCA detector V8w1, which was used for most of the measurements presented in chapter 6. An overview over the process is given in table 5.4, with the process step numbering in the text referring to that table. Generally, the process can be split up in five parts: the process preparation (step 1 to 7), the deposition of the thermalization pads on the front of the detector (step 8), the cryogenic deep-etching process itself (step 9), the processing steps related to electroplating (step 10 to 12), and the application of the Au-$\underline{\text{Ag}}$:Er-Au layer on the back of the wafer as a backside heat capacity (step 13 to 16). A cut-away view of the wafer at the end of each of each respective part is shown in figure 5.9.

Preparation

As a preparation for the deep etching process, the thermal oxide on both the front and the back side of the wafer have to be removed and the aluminum hard mask has to be applied and structured, as shown in figure 5.9a).

First, the thermal $\mathrm{SiO_x}$ from the front side is removed (step 1). The diameter of the circles in the etch mask is significantly larger than the diameter of the holes to be etched later, as the etching creates a step-like structure on the surface of the wafer (marked in figure 5.9b)) and the gold layer deposited in step 8 will be thinner and structurally weaker on this step. The larger diameter moves this structural weakness away from the holes etched from the back in step 9.

After removal of the resist used for etching (step 2), protective resist is applied to the front of the wafer (step 3) and an aluminum layer of 500 nm thickness is sputter deposited on the back side of the wafer (step 4). This layer will act as a hard mask for the etching of the vias later and has to be treated with care, as any scratch will lead to that scratch being etched through to the front of the wafer. Different choices for the etching mask are discussed below.

In order to structure the hard mask (step 5), 5214E is applied and structured. The aluminum is etched using the wet etch described earlier. Without intermitting lift-off, the thermal oxide of the wafer is etched on the back side of the wafer using plasma etching (step 6). As the aluminum is still covered by resist, redeposition of aluminum on the silicon is prevented, which could otherwise happen during the $\mathrm{SiO_2}$ removal plasma: Aluminum has a comparably low sputtering threshold [Jan96]. Afterwards, the protective resist on the front side and the structured resist on the backside of the wafer are removed with solvent (step 7).

step	Structure	Side	Mask/Resist	Process
(a)	**Preparation**			
1	Thermal oxide etch	front	5214E	plasma etch
2	Lift-Off	both	-	solvant
3	Protective resist	front	5214E	-
4	Al hard mask	back	-	deposition: 500 nm Al
5	Hard mask etch	back	5214E	Wet etch
6	Thermal oxide etch	back	5214E	plasma etch
7	Lift-Off	both	-	solvant
(b)	**Therm. pads**			
8	Thermalization pads	front	4533	deposition: 500 nm Au
(c)	**Deep Etching**			
9	Holes	back	hard mask	plasma etch
(d)	**Electroplating**			
10	Hard mask removal	back	-	wet etch
11	Au in vias	back	4533	Pulsed electroplating
12	Liftoff	both	-	solvant
(e)	**Backside heat cap.**			
13	Protective resist	front	5214E	-
14	Backside gold coating	back	-	deposition: 1 μm Au
15	Backside heat capacity	back	-	deposition: 1 μm Ag:Er, 100 nm Au
16	Lift-Off / cleaning	both	-	Solvant

Table 5.4: Overview over the fabrication steps for production of through-wafer vias for the MOCCA detector. The process can be split up in five separate steps numbered (a) through (e), namely the preparation, the thermalization pads, the deep etching, the electroplating and the backside heat capacity application, as explained in the text.

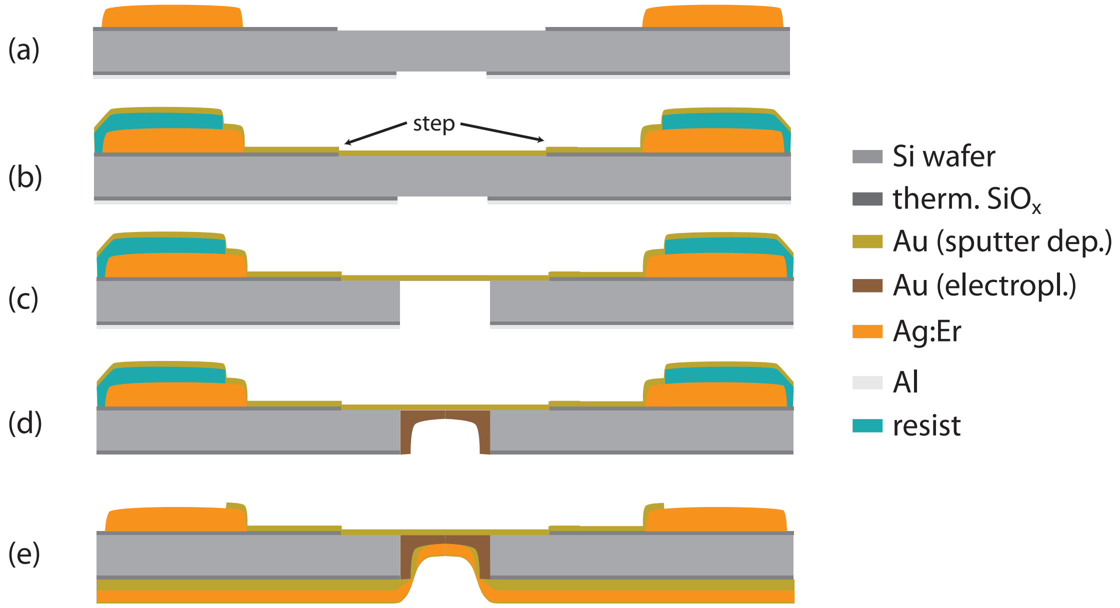

Figure 5.9: Cut-away view of the silicon deep etching process. The wafer is shown at the end of the respective processing for (a) the preparation processes, (b) the thermalization pad, (c) the deep etching, (d) the electroplating, and (e) the deposition of the Au-Ag:Er-Au layer on the back of the wafer, as listed in table 5.4. Layer thicknesses on front and back of the wafer are to scale, wafer thickness and lateral dimensions are not to scale. The protective gold layer on the sensor and other, previous layers were omitted in the drawing for clarity.

Aluminum was chosen as a hard mask as it showed an etch selectivity of better than $1 : 4000$ for the process used in this thesis[14], while selectivities of $1 : 10^5$ are reported in literature [Jan96]. For a hard mask, it is comparably easy to be removed with the aforementioned wet etching process. There is ambiguous data on aluminum hard masks influencing the etch rate. A significant disadvantage is the need of clean and complete removal due to the sensitivity of the electroplating liquid. Two alternatives to the hard mask were tested: a photoresist mask and a SiO_2 mask. Both did not show the required selectivity for the process. As an additional problem, resists with thicknesses above 1.5 µm show cracking, mostly occuring during the thermal ramping on cooldown before the process itself. Advantages and disadvantages of different masks were discussed in more detail in [Sai09].

Thermalization pads

The thermalization pad layer (step 8, shown in figure 5.9b)) has three separate functions. Firstly, the thermalization pad connecting groups of four sensors to the

---

[14] This is a lowest estimate, the actual selectivity can be much higher.

gold-filled through-wafer via providing the thermalization with the back of the wafer. Secondly, it acts as an etch stop for the silicon deep etch process. Thirdly, it is the electrical contact needed for the electroplating in step 11. The resist for structuring this layer stays on the wafer until step 12, which means it has to stay stable during etching and several hours of electroplating. Therefore, AZ 4533 is used as resist, additionally treated with a hard-bake. Then, 500 nm gold are deposited on the resist using sputter deposition. This thickness was found to be sufficient for producing gold films strong enough to act as an etch stop without tearing at a later stage of the process. Any hole that breaks complicates the following processing steps, e.g. applying photoresist evenly.

Cryogenic deep-etching

The cryogenic deep reactive ion etching process (step 9) was first described in [Tac88] and is a process used for dry-etching holes with straight vertical sidewalls into silicon. It uses a mix of SF_6/O_2 as a process gas. When the plasma is ignited, mainly, neutral fluorine radicals and the ions SF_5^+ and F^- are formed. When these ions are accelerated towards the subtrate, they react with the silicon, forming SiF_x. The SiF_x molecules are volatile and desorb from the surface. On surfaces directly exposed to the incoming ions, they also increase the desorption of non-volatile components. On areas not directly exposed to plasma particle impact, a passivation layer consisting of SiF_xO_y that is stable at cryogenic temperatures builds up protecting the silicon from etching, leading to an anisotropic etching profile. When warming up the wafer to room temperature, this passivation layer is almost completely removed. In spectroscopy measurements, it was shown that almost no SiF_xO_y is found on the side walls for room-temperature wafers [Dus04, Mel05]. Etch rates are strongly dependent on process parameters and the etched structure, but papers report rates between one and six micrometers per minute [Cra02, Sök09, Jia12]. A drawing of the wafer after etching is shown in figure 5.9c).

Generally, cryogenic silicon deep etching is reported to be a highly sensitive process where small changes of process parameters can have significant influences on the process outcome. Process parameters are reported to require optimization for every new geometry and structure. Within this thesis, a parameter optimization was done for etching a grid of 16×16 holes with a diameter of 300 µm each into a three-inch wafer, equivalent to the holes needed for MOCCA. The holes are etched from the back of the wafer, with a gold layer on front (the thermalization layer, step 8) acting as the stopping layer.

The most important parameters used in a cryogenic deep etching process are the power of the inductively coupled plasma and the high frequency source, the process pressure inside the reaction chamber, the temperature and the ratio of SF_6 content compared to the O_2 content. The final parameters are summed up in table 5.2, the influence of the parameters on the etching will be explained in the following.

The stage **temperature** enables the build-up of the passivation layer on the side walls: at temperatures above −80° C, the SiF_xO_y inhibitor is too volatile, leading to an etching of the side walls during the process and, by that, undercut or pear-shaped etching profiles. As shown in [Mel05], the passivation layer likely desorbs between −50° C and −80° C. Below −130° C, different crystal planes begin to exhibit different etch rates, leading to a side wall formation that depends on the crystal orientation of the wafer. In the temperature range between those two limits, the etch rate has been shown to slightly increase with temperature [Jia12].

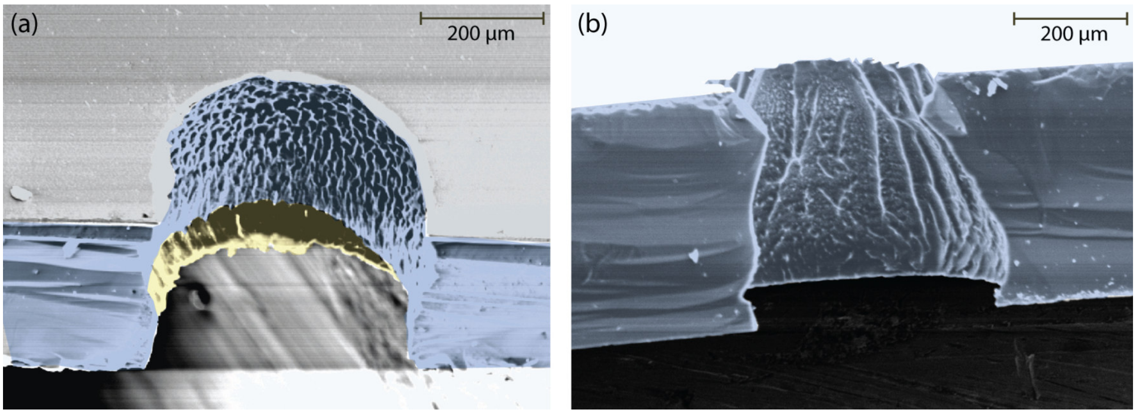

Figure 5.10: (a) SEM picture of an etched hole in a silicon wafer, etched using the process developed within this thesis. The wafer is coloured in blue, while the overhanging stopping layer made from gold is colored in yellow. The wafer was broken along the hole for this picture. (b) SEM picture of a hole etched with initial parameter set before adjustment of the parameters, showing an undercut and a pear-shaped hole profile. The wafer is colored in blue.

The **HF** field applied in the process can be used to control the acceleration voltage for the ions inside the plasma and, with this, the energy of the impinging ions on the etched substrate. The cost of increasing the HF power is that with it, the so-called dark sheath is increased, too. The dark sheath is a layer between the plasma and the etched substrate containing residual gas that the ions have to pass through. If the mean free path of the ions, which depends on the process pressure, is smaller than the thickness of the dark sheath at process pressure, a significant share of ions is scattered and hits the substrate at an angle. This can damage the passivation layer on the sidewalls of the via, leading to an undercut of the etched hole [Jia12].

Another means by which the form of side walls can be influenced is the **O_2 content** of the plasma. If chosen too low, not enough passivation is built up on the side walls, leading to an undercut. High oxygen contents, on the other side, can lead to passivation buildup that cannot be removed by the plasma, leading to an overcut profile [Jia12]. As an additional effect, black silicon can form in high oxygen environments [Sök09, Jia12]. Black silicon is the formation of small silicon pillars, a structure that absorbs light and therefore appears black to the eye. While black silicon can be used to find suitable parameters for the cryogenic deep-etching process [Jan09], the black silicon regime itself is not a desirable regime for MOCCA.

Finally, a significant change in etch rate can be achieved by manually cleaning the etching chamber, removing residuals left over from earlier etching processes. In tests, an uncleaned reactor could lead to etch rates decreasing by a factor of 10 and more. The manual cleaning needs to be done after the etching of the thermal oxide on the wafer (step 1 and 6). The purity of the wafer material can also influence the etch rate [Jan96]. For this reason, high-purity wafers with a resistance of $> 10\,\mathrm{k\Omega cm}$ were used for the MOCCA fabrication.

While etch parameters have to be adjusted according to the structures etched, the parameters listed in table 5.2 led to etch rates around $2\,\mu\mathrm{m}$ per minute for the holes in MOCCA, also achieving straight sidewalls. The parameters used before (slightly higher temperatures, higher RF power, a higher process pressure, a lower oxygen content, no manual cleaning of the reactor) yielded etch rates around 0.2 to $0.3\,\mu\mathrm{m}$ per minute [Sch19]. A comparison between a hole etched with the new process in comparison with a hole etched with the initial processing parameters is shown in figure 5.10. Until step 11, the holes are only covered with the gold layer deposited in step 8, so extra care has to be taken while handling the wafer.

Electroplating

As electroplating liquids are very sensitive to contamination with other metals, the aluminum hard mask has to be completely removed in advance of the electroplating (step 10). For this, the aforementioned aluminum wet etch is used.

For the electroplating (step 11), the gold layer on the front side of the wafer is used as the cathode. For this, a setup is used that presses the front of the wafer onto a teflon surface, with a thin gold foil between wafer and platform for electrical contact. The platform with the wafer is then completely immersed in the electroplating solution. As the surface inside of the holes is bulk silicon, the gold is both deposited on the back of the thermalization area and on the sidewalls of the hole.

If the voltage for electroplating is applied continuously, the electroplating solution inside the holes is constantly depleted of gold. In tests, this lead to the gold mainly depositing on the border of the hole on the back of the wafer, while very little gold

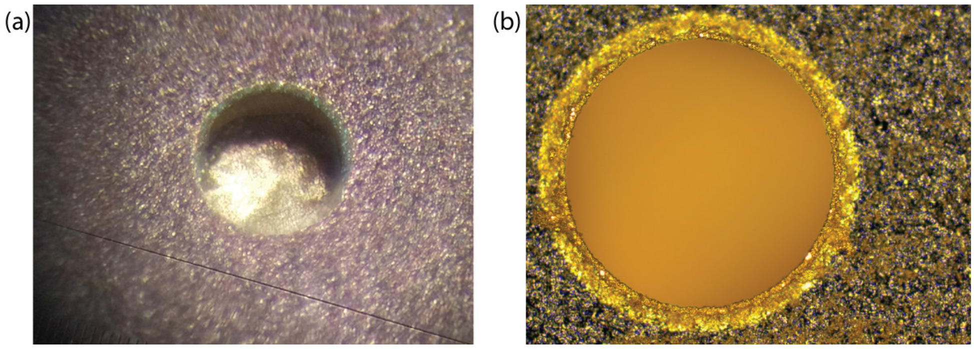

Figure 5.11: Picture of a gold-filled through-wafer via, taken with two different perspectives and depths of field. Both pictures are taken from the back side of the wafer which, for the wafer used here, was unpolished. (a) was composed of two separate photos with different focus settings.

diffused to the inside of the hole. In order to allow replenishment of the electroplating liquid through diffusion of the gold into the holes, the electroplating voltage was applied in pulses. A pulsing sequence of 1s on / 4 s off was found to be sufficient, leading to satisfactory gold deposition in the complete hole. The total electroplating time used for the MOCCA detectors was about two to three days, using a current density of approximately 1 mA/cm^2, leading to layers well above 10 µm. Even for photoresist specified for use in electroplating liquid, this duration can lead to significantly damaged photoresist, possibly enabling the electroplating liquid to flow in between platform and front of the wafer, which was clearly observed for one of the processed wafers. A new, recently constructed electroplating setup can be used to ensure that the electroplating liquid only comes into contact with the front of the wafer.

After electroplating, the wafer is cleaned using solvent (step 12), which also leads to a lift-off of the front thermalization layer. Two pictures of electroplated through-wafer vias, taken through different microscopes, are shown in figure 5.11.

Back side heat capacity

Finally, protective resist is applied to the front of the wafer (step 13) in order to coat the complete back of the wafer with a Au-$\underline{\text{Ag}}$:Er-Au layer. This is done in several sub-steps: first, two layers of 500 nm Au each are sputter deposited (step 14). For this, an special sputter holder is used, whose area is inclined by 30°. In between the deposition of the two layers, the wafer is turned by 180° inside the holder. This ensures thermal contact between the thermalization layer on the front of the wafer, the hole sidewalls and the gold area on the back of the wafer. Then, using a flat holder, 1 µm $\underline{\text{Ag}}$:Er is deposited to increase the heat capacity of the thermal reservoir on the back of the wafer (step 15), followed by 100 nm Au as a protective layer.

5.3.3 Fabricating a stable high-transparency gold grid

As explained in section 5.4.2, the final detector setup at CSR will need an electrically conducting grid with a transparency of at least 95 %. While the setup will be explained in section 5.4.2, the fabrication of the grid itself will be explained here.

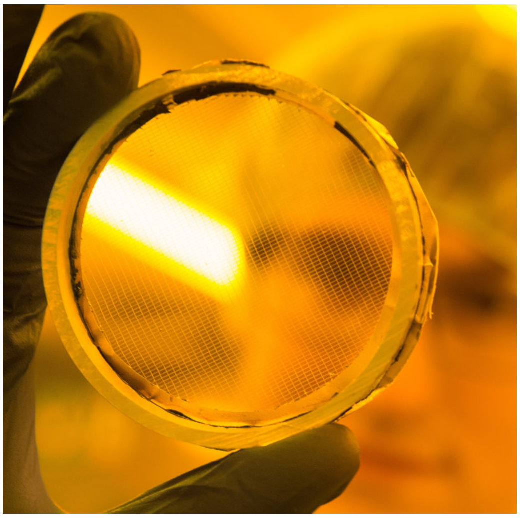

Figure 5.12: A prototype for the fabricated gold grids, produced in the cleanroom. For better handling, this grid was glued to an aluminum ring.

For testing, two grid sizes were fabricated: one with 700 µm × 700 µm pitch and one with 1400 µm × 700 µm pitch, both using a line width of 14 µm, achieving transparencies of 96 % and 97%. The pitch was chosen to be a multiple of the MOCCA absorber pitch to avoid Moiré effects.

For the processing, first, the full wafer is coated with resist. This resist allows the complete removal of the grid from the wafer after the fabrication. The resist is hard-baked and UV-irradiated. Then, 100 nm gold are sputter deposited onto the resist as a seed layer. Another layer of resist is applied and structured. This layer is used to define the grid for electroplating. Using the seed layer as a cathode, the grid is then electroplated to the desired thickness of 3 µm to 5 µm. In a partial lift-off, the resist defining the grid is removed while the first resist layer is left on the wafer. Then, using a dry plasma etching process, the seed layer is removed. By gluing the grid onto the setup for installation at the CSR and then putting the complete setup in solvent, the grid is released from the wafer. For this, it is necessary to choose a glue that is not attacked by the chosen solvent, e.g. Stycast 2850FT[15].

---

[15] Henkel AG & Co. KGaA, Henkel-Teroson-Strasse 57, 69123 Heidelberg, Germany.

The fabricated grids proved to be exceptionally stable. For future designs, higher pitches combined with smaller line widths will be tested to achieve higher transparencies.

5.4 Development of a 32 channel experimental setup

MOCCA, as well as other detectors recently developed within our group, need a total of 32 SQUID channels in order to operate. This lead to the development of a common wiring scheme with standardized connectors, enabling fast switching of experiments between cooldowns. Within this, the use of commonly used, safe and reliable wiring in each of the cryostats was established. This infrastructure was developed within this thesis, in collaboration with Steffen Allgeier [All17], and will be described in this section. Finally, the setup for the MOCCA detector inside the actual CSR ring itself will be described.

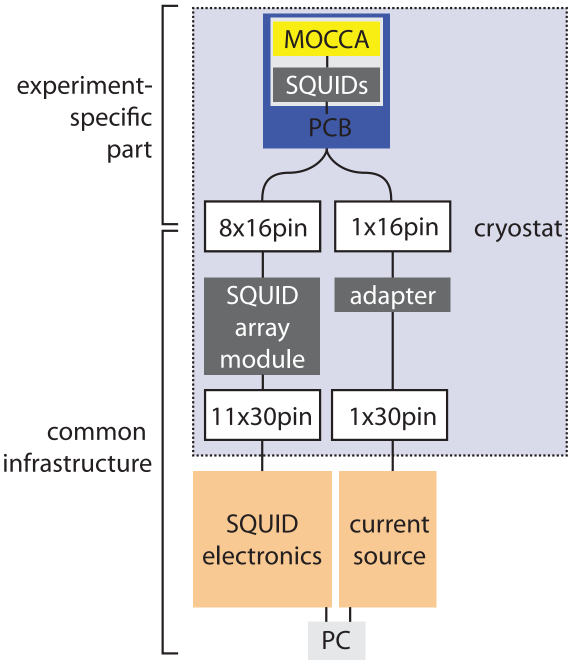

Figure 5.13: Schematic drawing of the detector readout chain. The part of the setup located inside the cryostat on the mixing chamber platform is marked with a light blue background.

5.4.1 32-channel cryostat infrastructure

This section describes the detector setup for MOCCA, and the wiring and modules that were installed in a total of four cryostats. The general setup can be used for

MOCCA characterization, but also for all other detector setups that use a two-stage SQUID flux-locked loop readout, and for SQUID testing at millikelvin temperatures. First, the general wiring will be explained, then, the different modules and wires will be listed.

Wiring scheme

The general scheme for wiring is sketched in figure 5.13 and can be split up in the part that is experiment-specific and the part used commonly by the different detectors.

The experiment-specific part of the wiring consists of the detector and, on the same platform close to the detector, the front-end SQUIDs. The front-end SQUIDs are connected to copper lines of a printed circuit board (PCB) using aluminum bonding wires. The interface between general and experiment-specific part are 16-pin connectors with a pre-defined pin layout. As four wires are needed between each front-end SQUID and SQUID array, four SQUID channels can be carried per cable. Therefore, MOCCA needs a total of eight such wires. Another 16-pin cable is used for connecting the persistent current switch.

From the SQUID array module, custom-fabricated 30-wire cables lead to the room temperature vacuum-feedthrough LEMO connectors[16]. Ten wires are needed to control each two-stage SQUID channel (see fig. 5.16), i.e. three SQUID channels can be carried by each cable. In total, twelve of these 30-pin cables are installed in each cryostat, setting the maximum at 36 SQUID channels. In the future, a specialized cable for connecting the persistent current switch will additionally be installed in all cryostats.

Printed Circuit Boards

All PCBs designed within the work for this thesis are fabricated from FR4, a flame-resistant composite material consisting of fiberglass cloth immersed in epoxy resin. Circuits are both on the front and the back side of each board, realized with 35 µm thick copper lines. To minimize oxidization of the copper and to facilitate the bonding, the copper is covered using ENEPIG[17], i.e. $3-8\,\mu\mathrm{m}$ nickel and $50-150\,\mathrm{nm}$ palladium, finished with a $50-100\,\mathrm{nm}$ layer of gold. Both sides of the PCB are covered with a layer of soldering stop. Vias were used to either connect front side and back side of the PCB or define the position for connectors with through-hole solder pins. Areas not covered by wires were used for large copper areas to improve thermalization. On the back of the PCB, those were pressed against the copper detector

---

[16] LEMO Elektronik GmbH, Hanns-Schwindt-Str. 6, 81829 Munich, Germany.

[17] ENEPIG is an acronym for Electroless Nickel Electroless Palladium Immersion Gold.

holder using screws, while vias are used to connect thermalization areas from front and back to ensure a good coupling between PCB and experimental temperature. For the PCBs shown in figures 5.14 and 5.15, designs were drawn using EAGLE[18] and fabricated by Multi Circuit Boards[19].

To connect the PCBs with the standardized readout infrastructure in the cryostats, two connector types were selected, a 16-pin connector[20] for the connections between front-end SQUIDs and the SQUID arrays and a 30-pin connector[21] used for connecting the room-temperature electronics with the SQUID array PCBs. The connectors both have two rows of pins with a pin center-to-center distance of 1.27 mm. The gold-plated pins have square cross sections with a side length of 0.5 mm.

Detector setup

Figure 5.14 shows a detector setup consisting of the MOCCA detector chip, the 16 front-end SQUID chips glued next to the border of the detector, a PCB with blue solder stop and a holder made from vacuum annealed copper. A collimator fabricated from aluminum (not shown) can be screwed to the copper holder.

To install the setup, first, the detector is placed into an indentation of the copper holder. Vacuum grease is used between detector and copper holder to fix the detector on the plate and ensure a thermal connection. The SQUIDs are glued using glue stick[22]. Then, the PCB is fixed to the platform. The PCB contains tongue-like structures pressing the detector onto the surface of the base. Detector, SQUIDs and PCB are electrically connected using wedge-bonded aluminum wires. For additional thermal connection, gold bonding wires are used between the large gold areas on the sides of the detector and the copper base.

Array module

The SQUID arrays, the second stages of the two-stage SQUID setups, are located in a separate module from the detector module. This has several advantages: As the SQUID arrays produce significant heating during operation, they could increase

---

[18] EAGLE was developed by CadSoft and is currently owned by Autodesk, 111 McInnis Pkwy, San Rafael, CA 94903, USA

[19] Multi Circuit Boards Ltd., Business Centres, Holyrood Close, GB-Poole, BH17 7FJ, Great Britain

[20] Type FFTP-08-D-18.00-01-N, Samtec USA, 520 Park East Boulevard, New Albany, IN 47150, USA.

[21] Type SFM-115-01-S-D, also from Samtec USA.

[22] Pro Office Klebestick, Carstensen Import-Export Handelsgesellschaft mbH, Werner-von-Siemens-Strasse 3, 25479 Ellerau, Germany

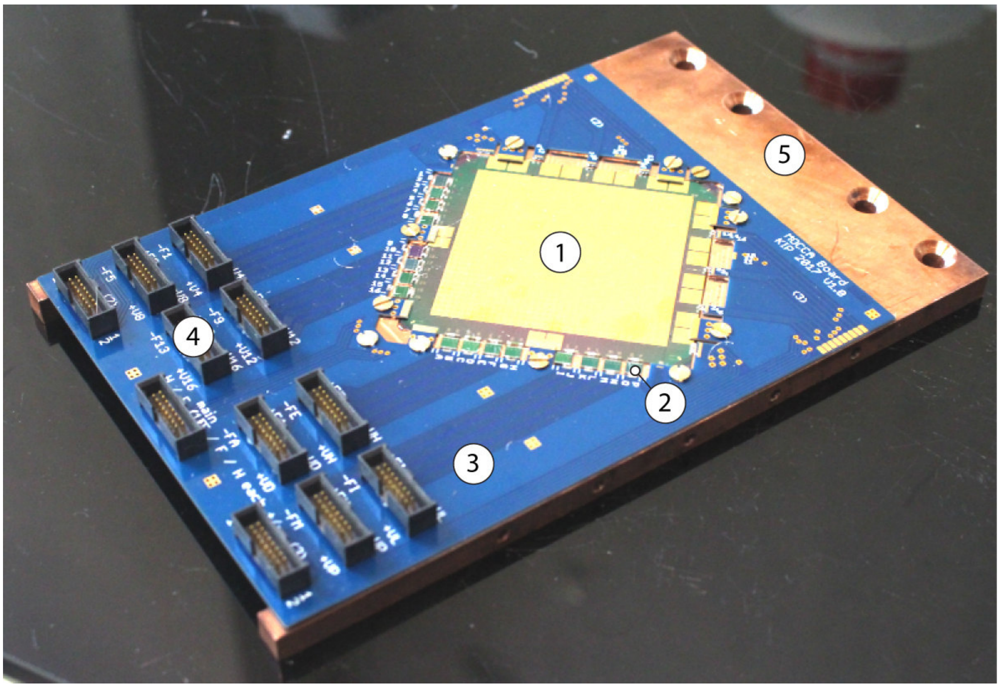

Figure 5.14: Setup of one MOCCA detector (1) with 16 SQUID chips (2), and the PCB (3) with the 16-pin connectors (4), screwed on the copper holder(5) and prepared for mounting in the cryostat.

the detector temperature and, therefore, decrease energy resolution if operated close to the detector. Also, through the separation, it is easier to use the same SQUID arrays in the same refrigerator for different experiments, significantly reducing the preparation time for setting up new experiments. Finally, during the design of the array module, special care could be taken to shield the SQUID arrays from the earth's magnetic field and electromagnetic interference.

One full SQUID array module can be seen in figure 5.15. The PCB has a finger-like structure, with one SQUID array chip glued to each of the fingers. Each SQUID array chip provides two separate SQUID arrays, leading to a total of 12 SQUID array channels on each PCB. The PCB, together with the SQUIDs, is placed inside a tin-coated copper holder which forms a cup-like structure around each finger, which is about 35 mm deep with a cross section of 6.2 mm × 3 mm. Using grub screws, the end of the finger-like structure is pressed against the holder to suppress vibrations of the PCB. The copper of the holder leads to a good thermalization of the SQUID arrays, while the tin forms a superconducting shield around the SQUID arrays at experimental temperatures, reducing external magnetic interference. In order to run a full MOCCA setup, three of these modules are needed. To provide additional shielding against the earth's magnetic field, a group of three modules is surrounded by

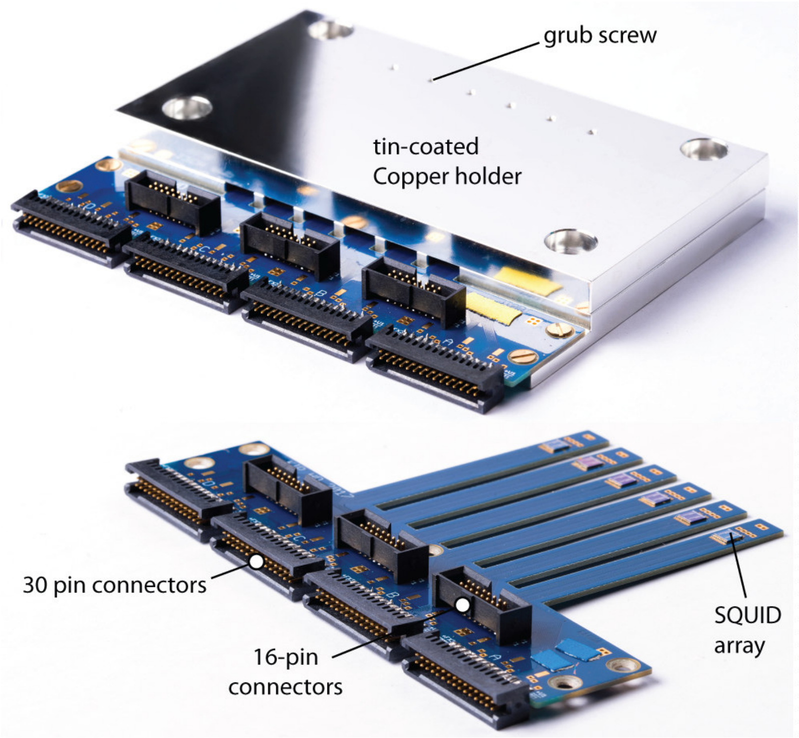

Figure 5.15: Holder for the SQUID arrays. **Top:** Full unit for a total of 12 SQUID array channels with tin-coated copper holder. The finger-like structures are inside the holder, resulting in a cup-like screening geometry. Grub screws are used to press the end of the finger-like structure against the holder to avoid vibrations. **Bottom:** PCB with the six SQUID array chips.

a cup made from a nickel-iron soft magnetic alloy[23] consisting of 81% Ni, 5% Mo, and 14% Fe. The alloy is heat-treated to attain high levels of magnetic permeability even at low temperatures, reaching a relative permeability of around 70000 at $T = 4\,\mathrm{K}$ and fields of up to 0.4 A/m, according to the specifications of the manufacturer.

Connection to room temperature

As mentioned before, every SQUID channel requires a total of nine separate wires between the experimental platform and the room temperature connector, resulting in a total of 360 wires for a full 36 SQUID channel setup. The wires add a heat load to the experimental stage. To keep the impact on the detector temperature as low as possible, the wires were made from a 98% Cu 2% Ni alloy, commercially available as alloy-30[24]. The wires have a diameter of 200 µm, a resistance of $1.56\,\frac{\Omega}{\mathrm{m}}$ and are

---

[23] Sold under the brand name Cryophy. Magnetic Shields Ltd., Headcorn Road, TN12 0DS, United Kingdom. Similar products are marketed under the brand name Cryoperm.

[24] Isabellenhütte Heusler GmbH, Eibacher Weg 3-5, 35683 Dillenburg, Germany.

coated with a thin resist layer for isolation. The Nickel atoms act as impurities, keeping the residual resistivity ratio at $RRR \simeq 1.2$, so that, in first approximation, the resistivity of the wires can be assumed as constant with temperature. As shown in [All17], no significant increase of the base temperature of the experiments is to be expected, while cooldown times were slightly increased after installing the cables.

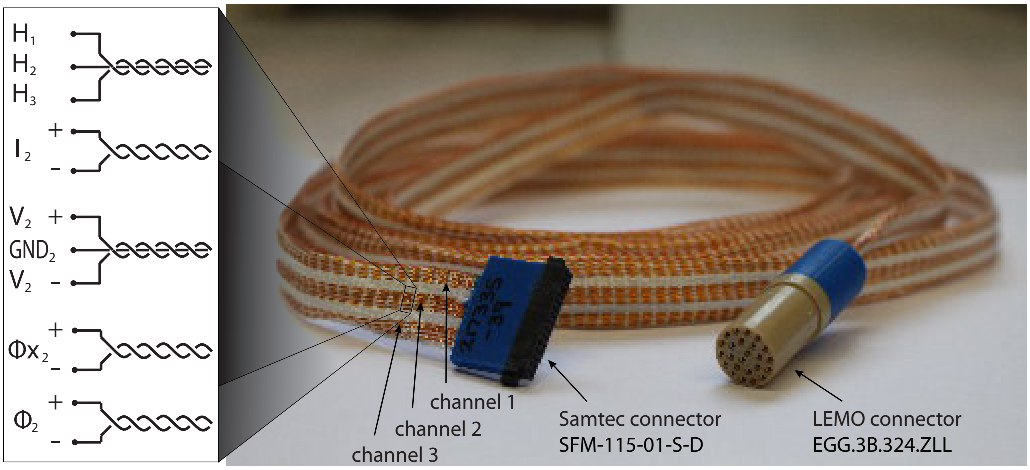

Figure 5.16: Schematical view of one channel of woven copper cables (left) and complete unmounted cable (right). The nine wires per SQUID channel are the feedback coil of the front-end SQUID (Φ_i), the feedback coil of the amplifier SQUID ($\Phi\mathrm{x}_\mathrm{i}$), the bias current for the detector SQUID (I_i) and two wires carrying the voltage over the array SQUID (V_i), given for channel i=2 in the picture. The heating lines for all three channels in the cable (H_i) are seperately twisted together. Adapted from [All17].

The cables, consisting of 30 wires interwoven with Nomex[25], are shown in figure 5.16. They were custom-fabricated by Tekdata[26] and have connectors on both sides: on the array module side, the 30-pin 2-row connector[27] fitting to the connectors used for the SQUID array boards is used, on the room temperature side, a 24-pin LEMO[28] connector is connected with a vacuum feed-through connector that is also fabricated by LEMO. The full setup, with 36 SQUID channels, consists of 12 of these cables.

The cables were heat-sunk at every temperature stage of the cryostat using the heat sink blocks shown in picture 5.17. They consist of seven copper plates that, when screwed together, have six grooves 0.73 mm deep, 24 mm wide and 50 mm

---

[25] Nomex is a chemically resistant, temperature-stable plastic. Fabricated by DuPont de Nemours GmbH, Hugenottenallee 175, 63263 Neu-Isenburg, Germany.

[26] Tekdata Interconnections Ltd, Innovation House The Glades, Festival Way, Stoke-on-Trent ST1 5SQ, United Kingdom

[27] Samtec TFM-115-01-L-D, purchased at Farnell, Farnell House, Forge Lane, Leeds, LS12 2NE, England.

[28] LEMO Elektronik GmbH, Hanns-Schwindt-Str. 6, 81829 Munich, Germany

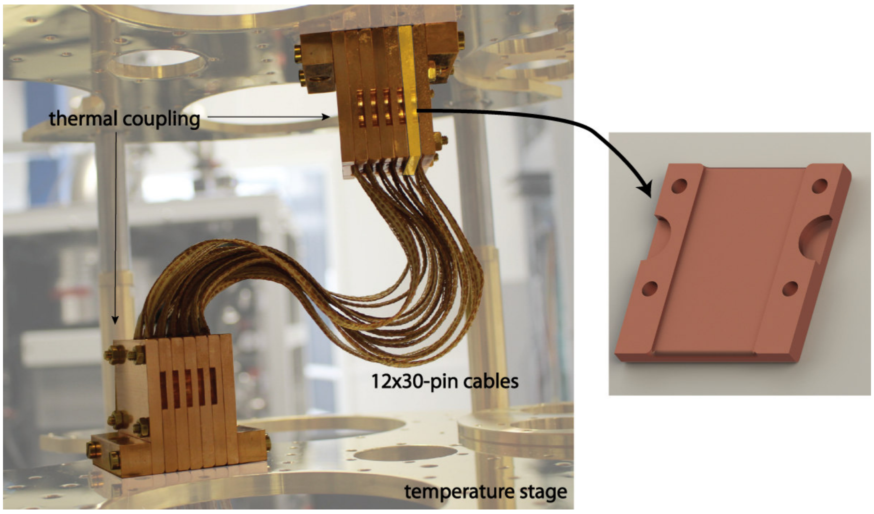

Figure 5.17: Right: Heat sinks for the cables between amplifier module and room temperature connector. The two temperature stages in the picture are the still stage (below, 750 mK), and the 3.3 K stage (above). **Left:** One of the copper plates with the indentation holding two cables is shown as a rendering from the model.

long, fitting two cables each. Inside the groove, vacuum grease is used to increase the thermal coupling between copper block and cable.

On the room-temperature end, the cables are connected to the vacuum side of LEMO vacuum feed-throughs, as described above. These vacuum feed-throughs are located in a designed aluminum case shown in figure 5.18, placed on top of the cryostat. Aluminum plates are used to support the box to reduce leverage on the cryostat flange.

5.4.2 Setup at CSR

In parallel to the development of the MOCCA detector, a setup was designed to install the detector inside the CSR ring. As the experimental setups at the CSR facility are dedicated for MOCCA only, generality of the setup is not necessary anymore. This section will explain the most important parts of the planned setup.

The MOCCA section at CSR

At CSR, MOCCA will be placed inside a future appendix of the beam tube shown in figure 2.1, which can be shut off from the main ring using a valve. This side arm will be placed in the already existing outer vacuum chamber. The future setup for the MOCCA detector and its surroundings after mounting in the CSR are shown in a

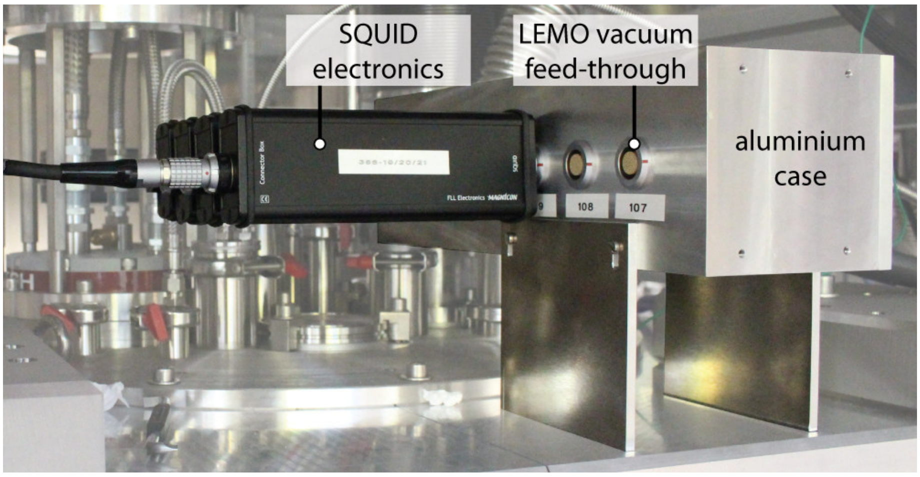

Figure 5.18: The aluminum case acting as an interface between cryostat vacuum and atmosphere, located on top of the refrigerator. The 30-pin cables (not shown) are plugged into the LEMO vacuum feed-throughs on the vacuum side. Then, the SQUID electronics can be connected at room temperature. To reduce the leverage through the aluminum box, additional plates were installed to support its weight.

sectional view in figure 5.19. It was decided that the cryostat will share the vacuum with the isolation vacuum of the CSR in order to keep the beam tube vacuum as low as possible. For that reason, a triangular detector chamber was constructed as an inset into the experimental vacuum. This detector chamber is shown in detail in figure 5.20. The MOCCA detector chip sits on the outside of this chamber in the beam vacuum, while the inside of the chamber is at isolation vacuum.

The cryostat will be placed on top of the detector chamber. MOCCA will sit on a copper base, screwed together with a large copper rod connected to the bottom of the mixing chamber of the cryostat. To ensure thermal coupling between the mixing chamber stage of the cryostat and the experiment rod, stainless steel screws will be used to screw the rod to the bottom of the stage.

As the beam tube is at temperatures of a few Kelvin, it cannot be directly connected to the detector chamber, which is at $T \simeq 20\,\mathrm{mK}$. Therefore, the connections between beam tube and detector chamber are made of thin wall stainless steel bellows with a comparably low thermal conductivity. Additionally, two intermediate temperature stages will exist, consisting of rings with a copper inlet to distribute the temperature equally. The temperature stages will be anchored to the 100 mK and the 750 mK stage of the cryostat via long copper rods, as shown in 5.21.

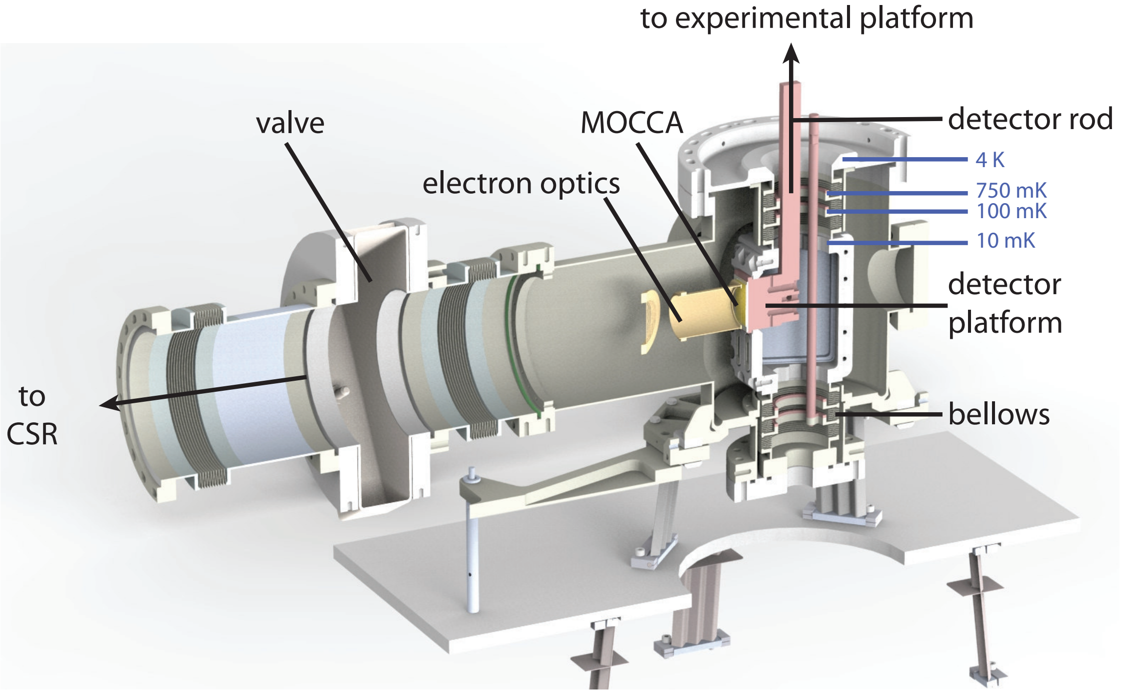

Figure 5.19: The planned detector sector of CSR, which will be located at the end of one of the four straight sections of the CSR. Depicted are the beam tube holding the experimental vacuum, the detector and the electron optics in front of the detector (shown in yellow) and the copper holder and rods used for heat sinking (shown in red-brown). Outer temperature shields and the vacuum chamber are not shown in this picture.

The triangular detector chamber

The triangular detector chamber is shown in figure 5.20. Each of the three sides of the chamber has a removable cover. In order to hold the MOCCA detector, one of the covers is welded vacuum-tight to a copper base.

The electrical connections for MOCCA will be similar to the ones in the test setup described above: the front-end SQUIDs will be glued in direct proximity of the MOCCA detector itself, and aluminum bonding wires will be used to connect detector, front-end SQUIDs and PCBs. The PCB will connect to four 37-pin Micro-D[29] vacuum interfaces[30] welded to the cover of the chamber. On the back of the platform, the Micro-D connectors will connect to 16-pin cables via an adapter PCB. These cables will be connected to a SQUID array block placed on the mixing chamber platform of the cryostat.

As can be seen in figure 5.21, MOCCA is mounted behind a circular copper

---

[29] Micro-D is a high-density connector norm of roughly half the size of Sub-D connectors.

[30] Glenair, Schaberweg 28, 61348 Bad Homburg, Germany

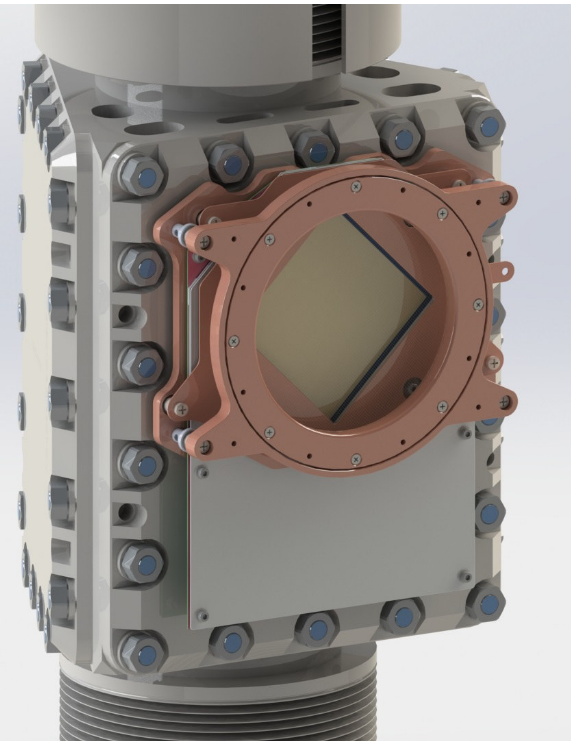

Figure 5.20: Drawing of the triangular detector chamber with the MOCCA detector placed on its holder. The figure was created by rendering a 3D model.

structure. This structure is part of a planned setup used to improve the timing resolution of MOCCA by measuring the secondary electrons emitted after a molecule hit the detector. This setup will be described in the next section.

Electron optics

To fully reconstruct the fragmentation of particles at CSR, a detector would be required to resolve the timing difference of the incident particles, which is in the range of nanoseconds. As the signal rise times of MOCCA are artifically slowed down to microseconds through the use of the Hydra principle, as described in section 5.1.2, this timing resolution cannot be achieved using the MOCCA detector on its own. For that reason, an additional setup was simulated in [Spa18], taking advantage of the secondary electron emission upon absorption of a massive particle on MOCCA: those electrons are accelerated onto a detector with high timing resolution to achieve the required timing resolution for the experiments at CSR.

The simulated setup is shown in figure 5.22. It consists of three electrostatic grids: one mounted in a distance of about 10 mm to the surface of the MOCCA detector, accelerating the secondary electrons in opposite beam direction, and two

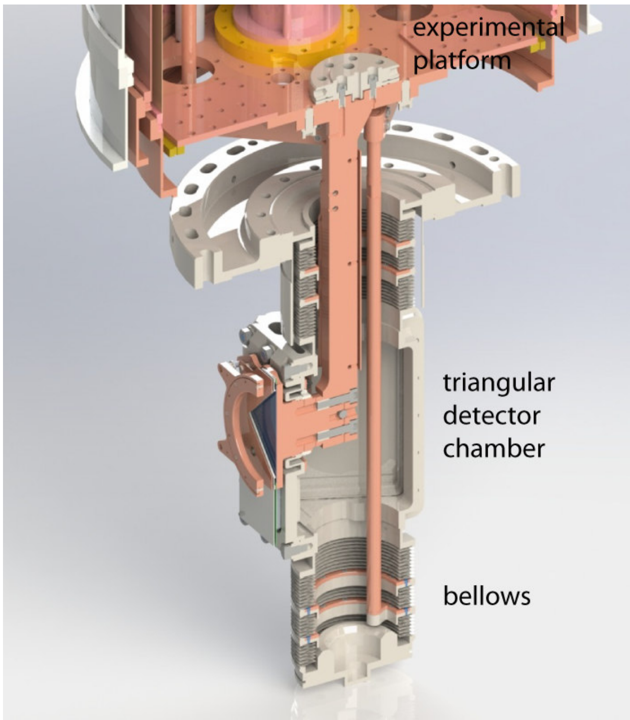

Figure 5.21: Sectional view of the experimental platform of the cryostat, mounting of the copper rod, and the triangular detector chamber. The drawing was created by rendering a 3D model.

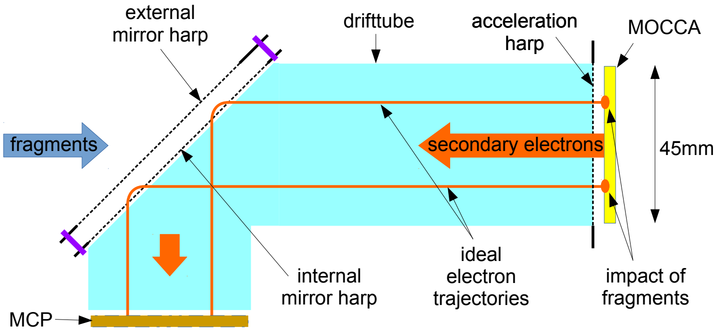

Figure 5.22: Schematic view of the simulated grid setup for the acceleration and deflection of secondary electrons caused by the impact of molecule fragments on MOCCA. Taken from [Spa18].

grids mounted at an angle of 45° to the beam direction. Those two grids are called the internal mirror harp and the external mirror harp. They deflect the secondary electrons by 90° onto a micro channel plate-type detector which amplifies the number of electrons. A fluorescent screen, monitored by a high-speed CCD camera, can be used to measure the arrival time of the electron bursts. This setup, with an acceleration voltage of 4 kV and an additional correction electrode at an intermediate voltage to alleviate fringe effects, can yield an impact time resolution of 30 ps, according to simulations. Also, the spatial mapping was simulated to be exact enough to resolve multiple particles simultaneously hitting the detector, predicting a deviation in the mapping of the impact spot from the MOCCA onto the screen better than 2 mm (with the exception of the outer edges of the detector).

This complete setup requires three electrostatic grids all placed in the path of the incoming ions towards the detector. Therefore, the transparency of every single grid should be maximal, as a transparency for a single grid of 95% already leads to a loss of about 14% of the incoming ions for three grids. As shown in section 5.3.3, a fabrication process for the grids was developed in the cleanroom of the institute, reaching transparencies of 97% with the possibility to go even higher.

5.5 Data acquisition and analysis

In order to analyze the data acquired in MOCCA measurements, a python class was written. The class takes data collected by PAQs, the acquisition software described in section 4.3.2, and uses the PulseReader package written by Arnulf Barth that will be explained in later publications [Bar21]. This section sums up the most important methods of the analysis class with a focus on the timestamp-based filtering, which can be used to filter noise for all other MMC-type detectors, too.

5.5.1 General analysis

Every particle impacting on a MOCCA absorber leads to two signals in two channels: one signal in one of the MOCCA detector channels 1 to 16 (number channels), and one in one of the channels A to P (letter channels). During analysis, to reconstruct where the particle hit the absorber, it is necessary to match those two traces to each other using the timestamp of the signal, which marks the ADC time at which a respective trace was recorded. By determining the rise time of the signal, the correct absorber from which the signal originated can be determined. Then, the correct template fit for that specific rise time can be used to determine the energy of the measured particle. Apart from particles hitting the detector, electromagnetic interference coupling into the experiment can cause large amounts of traces being written to disc. A major source for this noise are signals emitted by mobile phones. It is advantageous to filter those traces before fitting as, during fitting, it is hard to distinguish them from real events, especially for low-energy events.

In the following text, recorded data will be referred to as a **trace**. Traces originating from particles hitting the detector will be called **pulses**, and successfully matched pulse pairs will be called **coincidences**. Generally, analysis can be split up in three steps: First, all traces are filtered. Then, the pulses are matched to each other. To determine the energy spectrum of the measured particles, the traces are then fitted using a template fit method.

5.5.2 Timestamp-based filtering

Timestamp-based filtering describes all filters that only rely on the timestamp information, i.e. the respective value of the ADC clock at the activation of the trigger. Using timestamps for filtering has two significant advantages: As the timestamp information is very fast to access and the filter conditions can be formulated as vectorized calculations, they are extremely fast to calculate, even for very large measurements. Also, they are independent of signal height. As a large part of the noise recorded during measurements stems from phone signals and those signals have a very specific time structure, timestamp-based filters can be efficiently used to flag these traces. In total, five different timestamp filters were developed in collaboration with Robert Hammann [Bar21] and used within this thesis: the hold-off filter, the burst filter, the GSM filter, the false coincidence filter and the fixed ratio filter.

Burst filter

For a known hit rate A_{det} on the detector, the expected number of traces n_{tr} per time unit Δt_{bin} is given by $n_{\text{tr}} = A_{\text{det}} \times \Delta t_{\text{bin}}$. If the number of recorded traces within a certain time span Δt_{bin} significantly exceeds n_{tr}, it is very likely that those traces were caused by external sources and not by actual particles on the detector. The burst filter divides the complete measurement in bins with width Δt_{bin} and flags all traces within a bin if the number of traces within that bin exceeds a threshold. Usually, the bin width is chosen so that the amount of maximal traces per bin can be set to a about two to five. An example for the working principle of the burst cut is given in figure 5.23.

GSM filter

The **G**lobal **S**ystem for **M**obile Communication (GSM) is a technical standard describing protocols for cellular networks used, among other devices, by mobile phones. It was introduced in the 1990s and will stay in use in Germany for the foreseeable future. In order to enable multiple users to communicate on the same transmission frequency at the same time, GSM uses time-domain multiplexing. For this, GSM signals are split up in time frames with a length of 4.615 ms each, with each frame

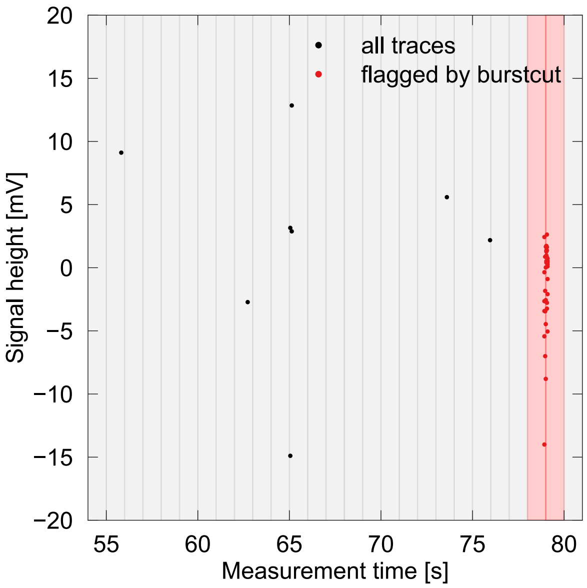

Figure 5.23: Sketch to illustrate the principle of the burst cut filter for a bin time of $\Delta t_{\mathrm{bin}} = 1\,\mathrm{s}$ with a maximum of four traces per bin. The red bins contain more than four traces, for that reason, all traces within that bin are flagged by the burst filter.

consisting of eight time slots with a length of 0.577 ms. Depending on how occupied the network is, users get assigned one or two time slots within one time frame, or one time slot every two frames for busy networks. Phones can send one of four signal types within their time slot: the so-called normal burst to transmit data, a frequency correction burst and a synchronization burst to align with the time and clock of the network, and an access burst in order to access the network. Each of these signal types has a guard period of 30.5 ms on the beginning and the end of the signal to avoid overlapping of signals due to different transit times. The access burst ends in a longer, additional guard period.

Signals sent by mobile phones in order to communicate with cell towers are strong enough to significantly interfere with MMC setups. A typical trace resulting from GSM signals, showing the characteristic time difference of one time slot 0.577 ms minus the guard time, is shown in figure 5.24. The GSM filter works by searching for a total of 42 typical GSM time differences Δt_{GSM} between two pulses in the same channel. Those time differences are multiples or combinations of time frames and time slots.

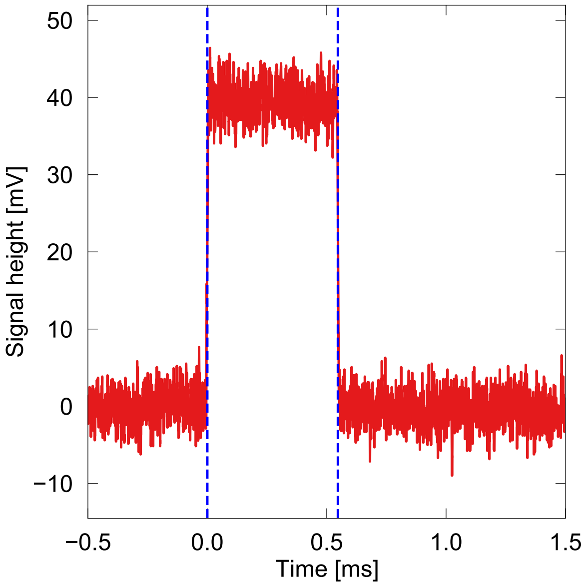

Figure 5.24: A typical trace caused by a GSM signal, recorded during a MOCCA measurement. The time distance between the two dotted blue lines is the width of one GSM time slot (0.577 ms) minus the guard time (30.5 ms).

Coincidence filter

In measurements with MOCCA, each event on the detector leads to two independent traces, one in a number channel, one in a letter channel. If the clocks of the ADCs used for the experiment are well-synchronized, these two independent traces will be typically recorded within a few µs of each other. It is possible that, within that time, two or more traces are recorded that both stem from a number or a letter channel. In the future measurements at CSR, these multi-hit events will be the normal situation, as the molecules will break apart into multiple fragments. However, in the experiments discussed here, we detect single photons and alphas at fairly low rates, so the probability to find two such events on MOCCA within 25 µs is below 10^{-4} and such events can be discarded without harm. The coincidence filter looks for these cases and flags them. An example for two flagged traces is shown in figure 5.25. This filter usually removes large amounts of GSM signals, as they typically hit multiple channels almost simultaneously.

Offline hold-off

In some measurements, the decay time of a signal is longer than the recorded trace itself. It is possible that the next trace in the same channel is triggered while the

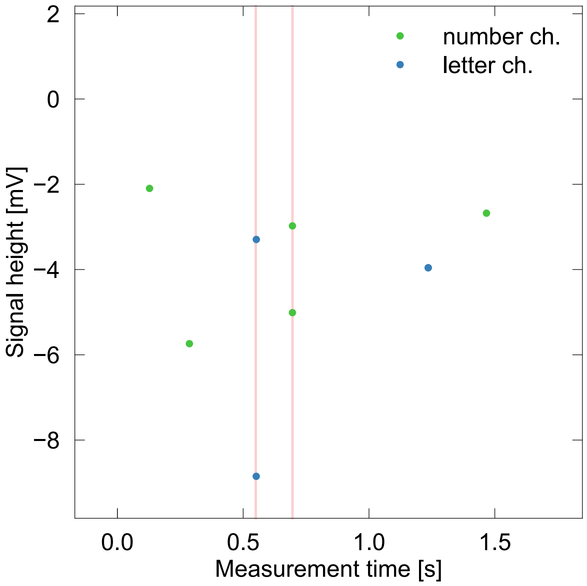

Figure 5.25: Working principle of the coincidence filter: If two traces occur coincidentally and both belong to the same group of channels, i.e. both are either from channel 1-16 or from channel A-P, they are flagged by the coincidence filter, marked by the vertical red lines.

signal of the previous pulse is still decaying. This pile-up distorts the pulse shape and can lead to wrong amplitudes during fitting and, by that, to a broadening of energy spectra in the analysis. The hold-off filter flags traces that follow within a time Δt_h on a signal in the same channel.

This filter is the offline-analysis equivalent of the hold-off-option in PAQs. If PAQs is set to filter for hold-off, the trigger is set to inactive for a certain time after it is activated, preventing pile-up events from being recorded.

Fixed Ratio filter

As radioactive decay is a statistical process, there should be no regular structure in the timestamps. For a given trace i, the fixed ratio filter calculates the time difference to the next two recorded traces $\Delta t_{i,i+1}$ and $\Delta t_{i,i+2}$ and, with this, the ratio between $r = \Delta t_{i,i+2}/\Delta t_{i,i+1}$ between those two values. The filter flags traces with certain ratios that can be given as an input to the filter. A fictional example is given in figure 5.26: here, $\Delta t_{13}/\Delta t_{12} = 2$, which would result in all three traces being flagged. Typical ratios to filter for are multiples of 0.5 between 1 and 4, as they are caused, for example, by GSM pulse bursts.

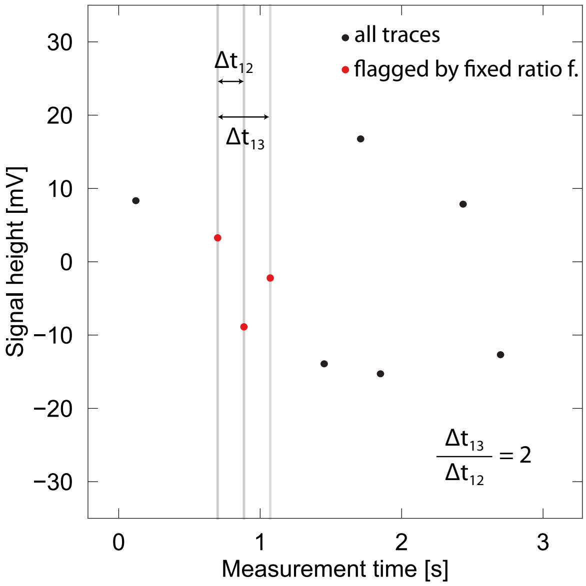

Figure 5.26: Principle of the fixed ratio filter, each point representing a recorded trace. As the relation between the timestamps of the three marked traces $\Delta t_{13}/\Delta t_{12} = 2$, those three traces would be flagged by the filter.

5.5.3 Coincidence search

Due to the column- and row-wise readout of MOCCA, it is necessary to match pairs of recorded traces to each other to resolve which sensor the signal originated from. As those traces arrive coincidentally, the timestamp of traces is used to match. Due to variations of the trigger times of the two pulses of a pair of pulses, timestamps of coincidences will usually differ by a small time difference δt. The principle to match traces to each other during offline analysis is explained in figure 5.27. Two pulses are accepted as a coincidence if three conditions are fulfilled:

- The time difference between the pulses δt is smaller than a limit δt_{jit} chosen during analysis, with δt_{jit} typically being in the range of a few µs.
- One of the traces was registered in a number channel (i.e. MOCCA channel 1 to 16) and the other was recorded in a letter channel (i.e. channel A to P).
- Within a range of δt_{jit} around both traces, no other trace was recorded on any other channel. For measurements at the CSR, this requirement needs to be dropped.

The efficiency $e = n_{\mathrm{co}}/n_{\mathrm{tr}}$ with the number of traces that are part of a found coincidences n_{co} and the total number of recorded traces n_{tr} is a measure for the

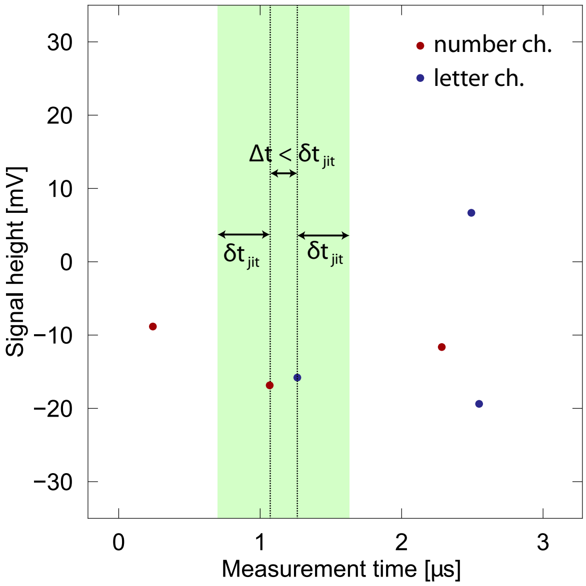

Figure 5.27: Illustration of the coincidence search during data analysis. Further explanation is given in the text. As the time difference between the two traces is below δt_{jit} and no other pulse was recorded within the area marked green, those two traces would be counted as a coincidence.

functionality of the detector. Reaching values close to 100% means that the described filters did remove the noise from the measurement efficiently and that all particle hits on the detector are successfully recorded both in the number and in the letter channel.

5.6 Used setups

For the measurements presented in the next chapter, different setups were used. This chapter introduces the two detector prototypes discussed in this thesis, the collimator options and the radioactive sources for X-ray photons and alpha particles.

5.6.1 Detector versions

For the data acquisition, two detector versions of the MOCCA were used: The MOCCA V7w1 and w2 and the MOCCA V8w1. The numbering refers to the design version (V7 and V8), w1 and w2 refer to the wafer number within the respective version. Pictures of MOCCA V7w1 and MOCCA V8w1 are shown in figure 5.28.

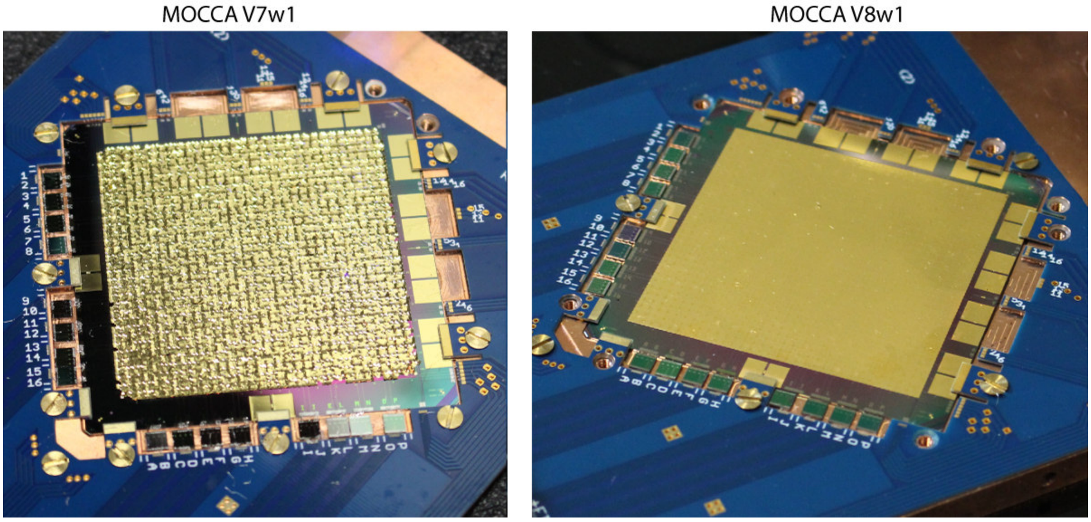

Figure 5.28: Two MOCCA chips discussed in this thesis. Both photos were taken of the full setup directly after finishing fabrication and before the first cooldown.

MOCCA V7w1 and V7w2

During the production of MOCCA V7w1 and V7w2, the deep-etch process development was still ongoing, so neither of the detectors has gold-filled through-wafer vias. As the lift-off process used during absorber fabrication included an ultrasonic bath to remove the remainders of the seed layer between the absorbers, the absorbers on the detector partially bent upwards. This causes the significant difference in appearance of the golden absorbers of the two detectors. The designed rise times for the hydra were 4, 20, 40, and 80 µs.

MOCCA V8w1

MOCCA V8w1 has different lengths of the thermal links between absorber and sensor, leading to different designed rise times of 4, 8, 12 and 16 µs. For absorber fabrication, a dry etching plasma for seed layer removal after the absorber fabrication was used, yielding completely flat absorbers. MOCCA V8w1 is also the first MMC from our group having gold-filled through-wafer vias. Due to a processing error during the lift-off of the second isolation layer, SiO_2 flakes cut off some of the thermal links between absorbers and the sensor, introducing a sensor-dependent variation of the measured signal rise times.

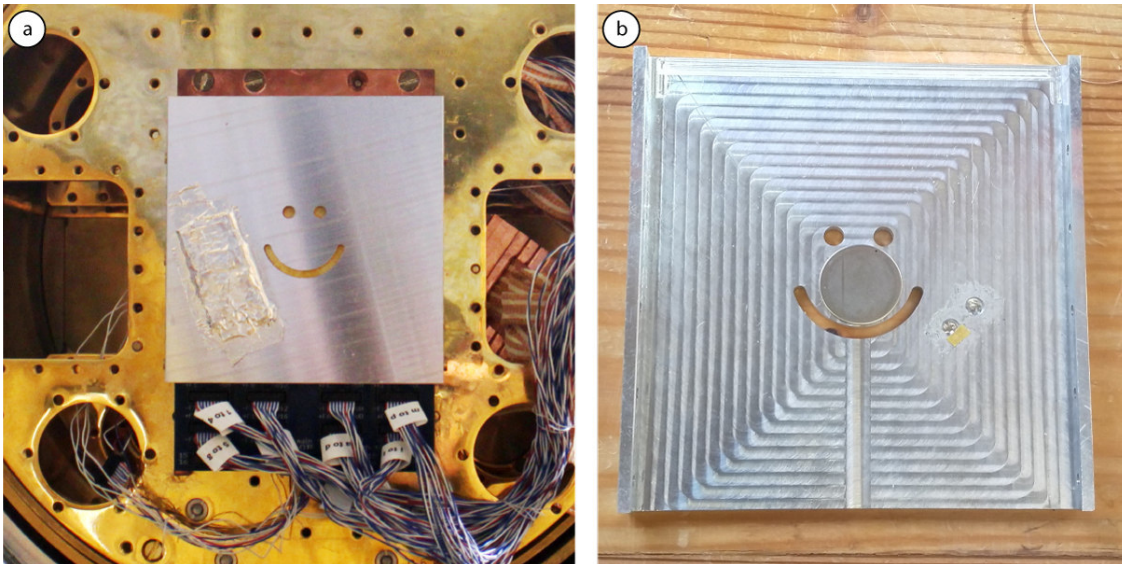

Figure 5.29: The collimator used for MOCCA measurements: (a) A collimator forming a smiley, screwed to a detector setup mounted on the experimental platform of the cryostat and connected to the readout wiring. (b) Disc source containing trace amounts of ^{241}Am and ^{243}Am, mounted on the detector side of the collimator.

5.6.2 Detector setups

The MOCCA detector is mounted on the copper holder using a small amount of vacuum grease[31] to increase the mechanical stability, to dampen vibrations of the MOCCA chip and to ensure a thermal connection between holder and MOCCA. The copper holder is made from heat-treated copper to maximize the thermal conductivity. The SQUIDs used within this thesis are all in-house fabricated[32].

The PCB was designed within the work for this thesis. The properties of the PCB are described in section 5.4.1. By manually setting aluminum bonding wires between them, PCB, front-end SQUIDs and the detector were connected to each other. For the spatial resolution measurements presented in chapter 6.2.10, a collimator was mounted in front of the detector. The collimator is made from aluminum with a thickness of approximately 5 mm and can be screwed to the copper base. To demonstrate the spatial resolution of MOCCA, the collimator has the form of a smiley face, as shown in figure 5.29. A disc with a low activity alpha source was glued to the detector side of the collimator, leaving a distance of approximately

---

[31] Apiezon N, Hibernia Way, Trafford Park, Manchester, M32 0ZD, United Kingdom

[32] The used front-end SQUIDs were from the SQUID generations HDSQ10ä-w1, HDSQ13-w3, HDSQ13-w4 and HDSQ14-w1, the array SQUIDs were from the generations HDSQ5-w3 and HDSQ12a-w1.

1 mm between detector and source. The mounting is shown in figure 5.29b). A second collimator was used for X-ray photon measurements determining the energy resolution of MOCCA. It has a rectangular hole over channels 5 to 8 and d to l, respectively.

5.6.3 Radioactive sources

For measurements with the detectors, two separate radioactive sources were used: an encapsulated ^{55}Fe source with an activity of 37 MBq, mounted outside the cryostat and illuminating the detector through a series of IR-blocking X-ray windows in the radiation shields of the cryostat, and a disc containing trace amounts of ^{241}Am and ^{243}Am on its surface.

The isotope ^{55}Fe has a half-life of 2.73 years and decays via an electron capture process to an excited state of ^{55}Mn. In 90 % of cases, the captured electron stems from the K-shell, leading to X-ray photons (branching ratio 28 %) or Auger electrons during the relaxation of the atom. The X-ray photons are able to leave the source through the X-ray window; about 90 % of the resulting X-ray photons are Mn-K$_\alpha$ photons with an energy of about 5.9 eV, while 10 % of the rays are Mn-K$_\beta$ photons with an energy of around 6.5 eV. The K$_\alpha$ line exhibits a hyperfine splitting of about 12 eV, which can be resolved by high-resolution MMC-type detectors, but not by MOCCA. The center of mass of the K$_\alpha$ line is at 5.8944 keV, the one of K$_\beta$ is at 6.4864 keV.

The disc has a diameter of 2 cm and a low activity of 2 Bq by ^{241}Am, which mainly emits alpha particles at 5.485 MeV when decaying to ^{237}Np, and 1 Bq by ^{243}Am, decaying to ^{239}Np with a main energy of 5.275 MeV. The outer 2 mm of the disc do not contain Am, therefore, the effective diameter of the source area is 1.6 cm.

6. Experimental results

This chapter will sum up the experimental results achieved with the detector setups described in section 5.6. First, the filters described in section 5.5.2 used to remove noise from the acquired data sets will be characterized. Then, data measured with the MOCCA detectors will be presented, demonstrating the full functionality of the detector.

6.1 Noise filtering

Mobile phones or WiFi signals can lead to rapid voltage transients in the detector signal, leading to an activation of the trigger. This can seriously impede a measurement: especially in the low energy region, the traces of these events can pass as real pulses with low amplitudes during fitting, leading to incorrect lines in the energy spectrum. Therefore, it is necessary to flag those traces before fitting.

In order to compare the different filters, a noisy part of a measurement with a rate of 1.06 pulses per second[1] was selected. Then, the different timestamp filters introduced in section 5.5.2 were applied to the data. Within the shown time span, a total of 136000 traces were recorded, over a factor 7 more than expected with the given rate. The filter results[2] are shown in figure 6.1. For comparison, the unfiltered amount of traces per bin is shown in grey in every histogram, with one bin standing for a measurement time of approximately 18 seconds. The colored bins show the amount of traces that passed the respective filter. In order to estimate the amount of pulses incorrectly flagged as noise, the amount of filtered traces on a noise-free part of the measurement was calculated, which are referred to as false positives in the text.

For this comparably low-rate measurement, the **GSM filter** works well for removing actual noise, not real pulses: no false positives were registered. This is reasonable, as the time differences filtered by the GSM filter are all below 100 ms, which is significantly smaller than the average time difference between traces of one channel in this measurement. For the five-hour stretch shown in figure 6.1, a total of 50 % of traces were flagged. A significant part of the traces in high-intensity bursts

---

[1] To simplify, this rate refers to the number of recorded pulses per second, not to particles hitting the detector per second. As every particle leads to two separate pulses, the actual measured rate of particles on the detector was 0.53 Bq.

[2] The hold-off filter is not considered in this discussion, as its primary aim is to remove pile-up, which it does by definition.

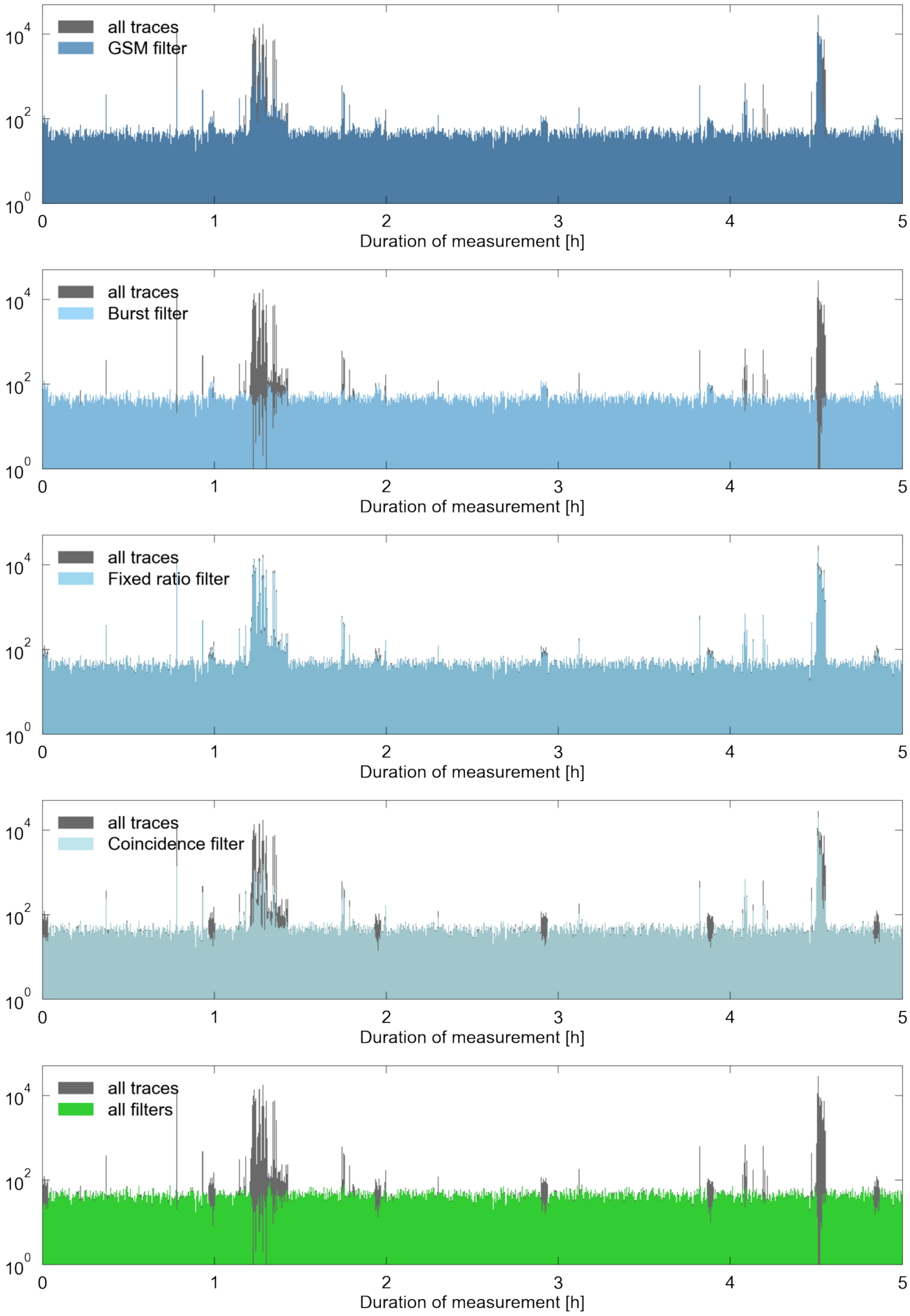

Figure 6.1: Histograms of recorded traces per timespan for five hours of a noisy measurement before and after filtering. Each of the histograms shows the original amount of recorded traces in grey and the amount of traces that passed the filter in the respective color. The green histogram shows the total filtering result for all filters.

are not detected: At high noise intensities, channels sometimes are just triggered as fast as the setup allows, creating timestamps that do not follow any particular pattern.

For a lot of measurements, the **burst filter** proved to be the most reliable filter. Just as the GSM filter, it had no false positives. During intense signal bursts, the burst filter tends to remove real pulses in addition to the noisy signals. For most measurements, this can be seen as an advantage: pulses recorded during intense noise bursts tend to be distorted, or the trigger might be so occupied that no real pulses can be triggered at all. For the example measurement, the burst filter removes 85 % of traces. Even when taking the removed pulses during the intense bursts into account, the number of traces after the burst cut is very close to the number of traces expected from the rate on the detector. About 14 % of all traces were exclusively flagged by the burst filter, compared to below 1 % for the GSM or the coincidence filter.

Within the presented measurement, the **fixed ratio filter** is the least effective. It has a rate of 2 % false positives, but only flags 13 % of traces within the examined noisy time span. 3.8 % of traces are flagged exclusively by the fixed ratio filter. It was observed that, in other measurements, the fixed ratio filter can be very efficient to find noise not found by any other filter, making it a tool for measurements where complete noise removal is of high importance.

Finally, the **coincidence filter** is, by definition, effective in its intended job. However, the filter also removes a lot of GSM noise. In total, the filter removes 59 % of traces.

Adding all the filters up, the noise created by electromagnetic interference was efficiently removed. The average rate of pulses after filter is 1.08 hits per second, very close to the expected rate. In general, the filters were tested on measurements with rates between 0.5 Bq and 40 Bq and worked reliably in that range for MOCCA. Filters developed in parallel for the ECHo project showed similarly promising results. Therefore, the implementation of these filters into the online acquisition program PAQs is planned.

6.2 Characterisation of the MOCCA detector

In order to characterize the MOCCA detector, measurements using the ^{55}Fe and the alpha source described in section 5.6.3 were performed. In this section, first, the inductance of the pick-up coils of the detection channels of MOCCA is experimentally determined, followed by a demonstration of the readout principle of the detector. The signal height for different persistent currents is shown and compared to simulations.

Then, the signal shape is discussed, determining the decay time for a detector with and without through-etched vias, and the functionality of the hydra principle is presented. The cross talk between different detector channels is measured. Then, the energy resolution for measurements of X-ray photons is shown, and the linearity of the detector is calculated. Within this chapter, data was acquired using the newest detector, MOCCA V8w1, unless explicitly stated otherwise.

6.2.1 Pick-up coil inductances

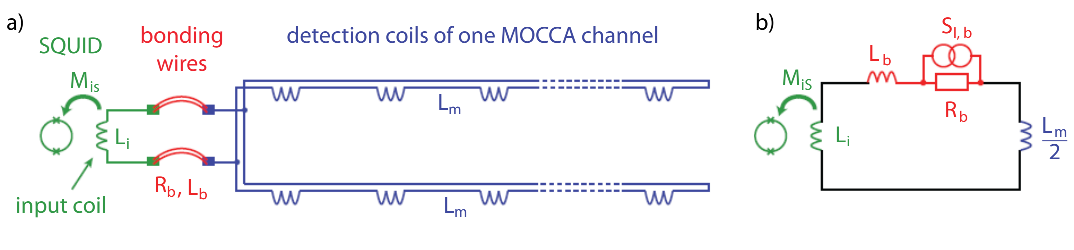

Figure 6.2: Sketch (**left**) and equivalent circuit (**right**) of the detection coils of one MOCCA channel, connected with the input coil of a SQUID via aluminum bonding wires. Adapted from [Gam19].

It is possible to estimate the inductance of the pick-up coils of the MOCCA detector channels using the spectral noise recorded at temperatures around 4 K. At these temperatures, the aluminum bonding wires are still normal conducting and cause a current noise that can be described with a spectral current density $S_{I_b} = 4k_B T/R_b$, where R_b is the resistance of the bonding wires. This current noise couples into the SQUID via the mutual inductance M_{is}, causing a flux noise in the SQUID. As can be seen in the equivalent circuit for one MOCCA channel shown in figure 6.2, the resistance R_b forms a low-pass filter together with the total inductance $L_{tot} = L_i + L_b + L_m/2$, consisting of the inductance L_m of one row of pick-up coils, connected in parallel with a second row to form a channel, the inductance L_b of the bonding wires and the inductance L_i of the input coil of the SQUID. The low pass has a cutoff frequency

$$f_s = \frac{R_b}{2\pi L_{tot}}. \tag{6.1}$$

By fitting the measured noise at 4 K to the total noise

$$S_{\Phi,ges} \approx S_{\Phi,b} + S_{\Phi,w} \tag{6.2}$$

with the white noise $S_{\Phi,w}$ of the SQUID and the current noise caused by the bonding wires

$$S_{\Phi,b} = M_{is}^2 \frac{4k_B T}{R_b} \frac{1}{1 + (f/f_s)^2}, \tag{6.3}$$

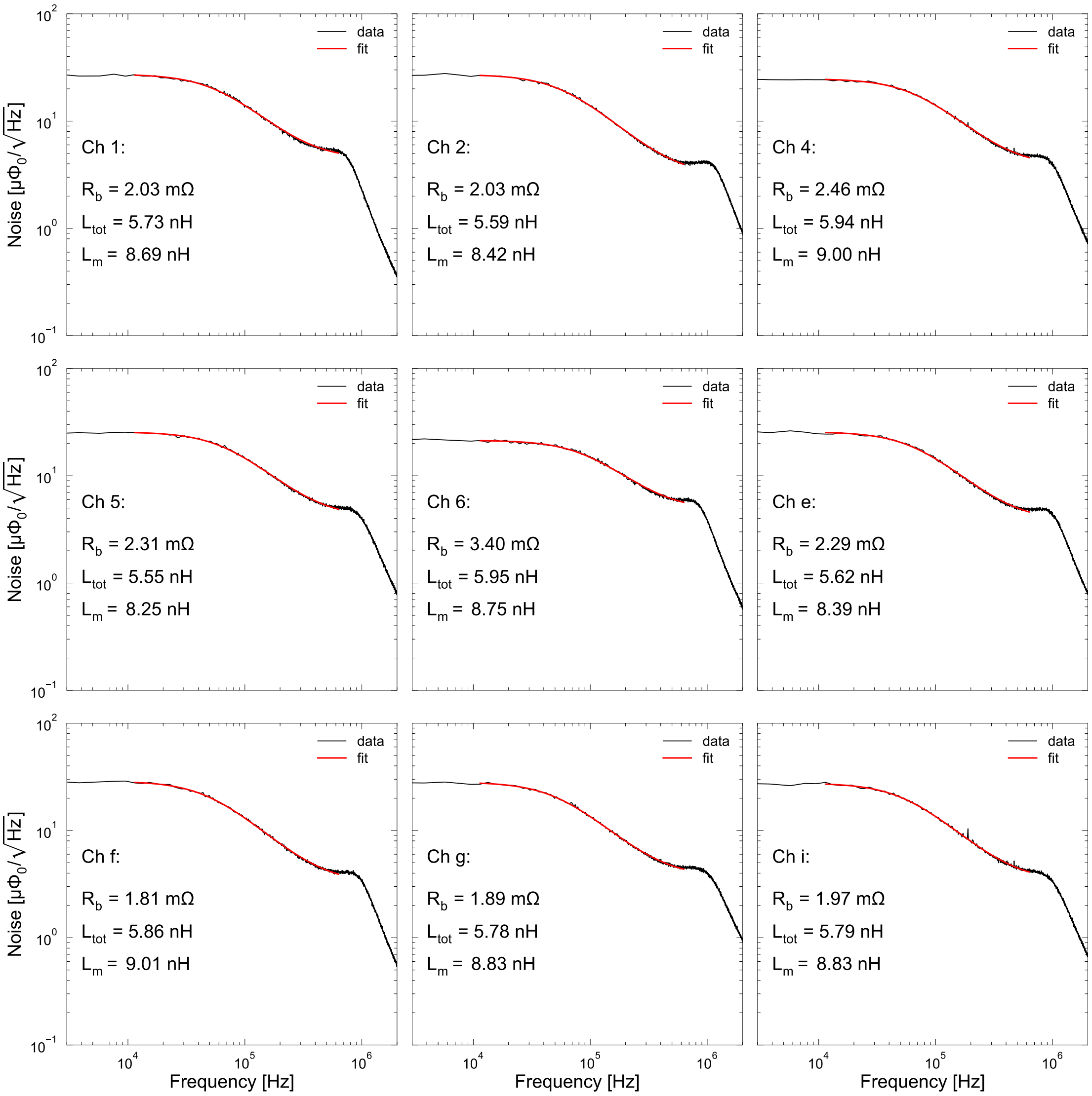

Figure 6.3: Noise spectra of MOCCAV8w1, measured at 3.5 K on different channels of MOCCAV8w1. The results of fitting equation 6.2 to the data and the resulting inductance L_m for one row of pick-up coils are given in the plot. The resulting fit function is shown in red.

the total inductance L_tot and the resistance R_b can be determined for each channel. By estimating the inductance of the bonding wire using the relation

$$L_\mathrm{b} = R_\mathrm{b}(0.14 \pm 0.04)\frac{\mathrm{nH}}{\mathrm{m\Omega}} \tag{6.4}$$

given in [Hen17], the inductance L_m of each row of pick-up coils can be calculated.

Figure 6.3 shows the measured spectral density of the magnetic flux noise in the front-end SQUID for selected number and letter channels of MOCCA V8w1 at a detector temperature of 3.5 K in a double logarithmic plot. The values for R_b, L_tot and L_m determined by the fit for the respective channels are given in the plot. The measured spectral noise shows two plateaus: Additional to the white noise level at high frequencies, as expected, a second plateau occurs at lower frequencies, caused by the noise of the bonding wires. The cutoff at around 1 MHz is caused by the limited bandwidth of the readout.

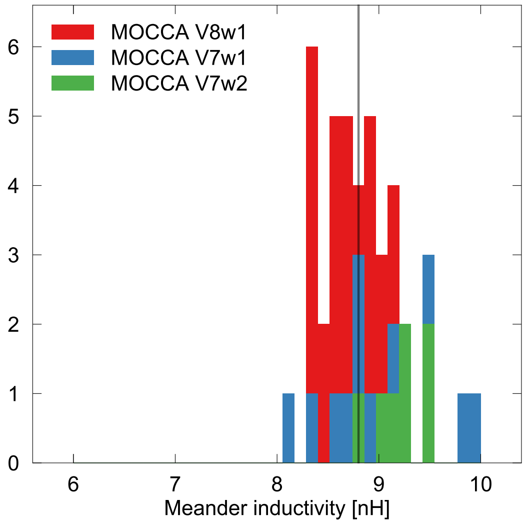

Figure 6.4: Values for the inductance L_m of single rows of pick-up coils for MOCCAV8w1, MOCCAV7w1 and MOCCAV7w2, determined by fitting equation 6.2 to the noise spectrum acquired at 3.5 K, shown as a stacked histogram. The designed value $L_\mathrm{m} = 8.8\,\mathrm{nH}$ is given as a vertical line.

The results for L_m for several channels of MOCCA V7w1, V7w2 and V8w1 are shown as a stacked histogram in figure 6.4. The designed value, $L_\mathrm{m} = 8.8\,\mathrm{nH}$, is given as a black line. Generally, a good agreement between the values for the different detectors and the designed value can be seen. One possible reason for the observed spread of the values can be that an average value had to be assumed for the input sensitivities M_is, which can vary from chip to chip and has a significant influence on the fit outcome. While theoretically possible, it is unlikely that the variations are caused by fabrication errors such as short circuits in single pick-up coils or line width variations, as none of them were observed during the fabrication of the detectors. The mean value for MOCCA V8w1 is $L_\mathrm{m} = (8.7 \pm 0.2)\,\mathrm{nH}$, which includes the design value within the margin of error, therefore, a good agreement between measured values and the designed value can be assumed.

6.2.2 Demonstration of the readout principle

As explained in section 5.1.3, each time MOCCA is hit by a particle, two pulses are generated, one in the respective letter channel row, one in the number channel column. These pulses are then independently triggered and written to disk. Figure 6.5a) shows an example for the resulting timestamps of the arriving pulses for row i and column 5. If a pulse originates from sensor +i+5, +i−5, −i+5 or −i−5, both channel 5 and channel i receive a coincident signal. Those pulses are marked with a black dotted line. The other recorded traces originate from other sensors that are read out by either channel i or channel 5.

Figure 6.5b) shows a histogram for the timestamp differences between subsequent traces in channel i and 5 between 0 and 200 µs, with the coincidences shown in yellow. The coincidences arrive with a relative time differences of less than 23 µs. The time difference depends on small variations of the trigger time due to the overlaying noise on the detector signal, variations in signal rise time, imperfect synchronization of the ADC clocks and the use of different cable lengths in the setup and, therefore, can vary slightly, depending on the respective pair of channels. With a typical time difference of a few µs between the timestamps of coincident pulses, the maximal rate on the detector in measurements is determined by avoiding pile-up and not by the ability to identify coincident pulses.

Figure 6.5c) shows a histogram of the timestamp differences between two traces for a range between 0 and 200 ms. On this scale, the coincidences are all within the first bin. A step can be seen at 6.3 ms, marked by a dotted black line. The step is caused by the online hold-off filter chosen in PAQs for this measurement, as described in section 5.5.2. This is the expected behavior for the hold-off filter, as the hold-off filter works channel-wise, i.e. for the two channels pictured, the amount of traces is approximately halved by the hold-off. Apart from that, the occurrence of timestamp differences follows an exponential distribution, as expected for hits caused by a radioactive source.

As coincident pulses stem from the same event and the same sensor signal, they should be identical in form, but may differ in signal amplitude due to different persistent currents in the respective channels. Figure 6.6 shows three examples of raw data of recorded pulses that were found to be coincidences during analysis, originating from different sensors. A grey line has been added, showing the relative difference of the two normalized traces. As demonstrated by the plot, the traces share the same rise time and decay time and the relative deviations are limited to the detector noise overlaying the signal. However, the relative amplitudes between the two traces vary from sensor to sensor. This behavior is discussed in the next section.

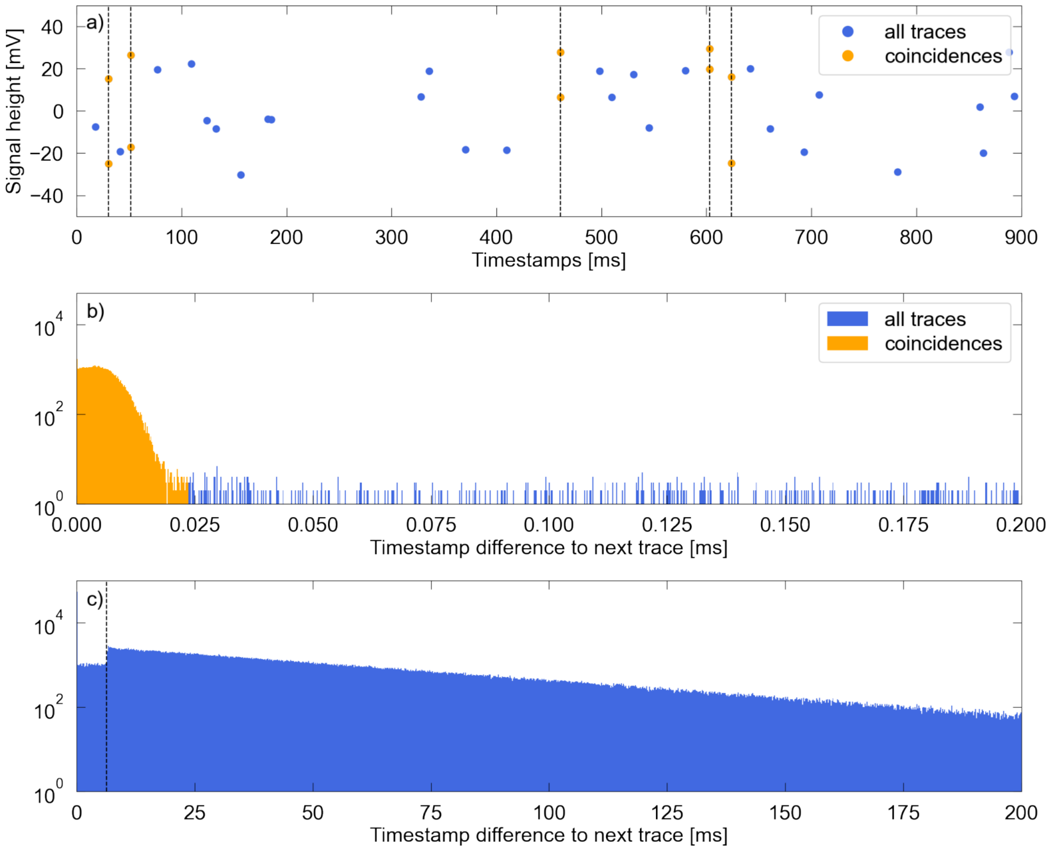

Figure 6.5: Demonstrating the functionality of the column- and line-wise readout on a measurement of X-ray photons with a sampling rate of 5.05 MHz for signals from channel i and 5. **a)** Signal height, plotted against the timestamp, for recorded traces during a 900 ms stretch of a measurement. Traces that were identified as coincidences are shown in yellow and marked with a black dotted line. **b)** Timestamp differences between subsequently recorded pulses in the range between 0 and 200 µs, shown as a histogram. Timestamp differences between coincident traces are marked in yellow. **c)** Timestamp differences between traces in the range between 0 and 200 ms. The black dotted line shows the online hold-off value applied by PAQs during the measurement.

6.2.3 Signal height

Preparation of the persistent current within this work was achieved using special electronics that control the superconducting current switch by delivering µs heating pulses. For MOCCA V8w1, the persistent current was prepared separately for the number and the letter channels.

To check the amount of persistent current in the respective channels, the relative amplitude of each coincident pair of a number and a letter pulse were determined

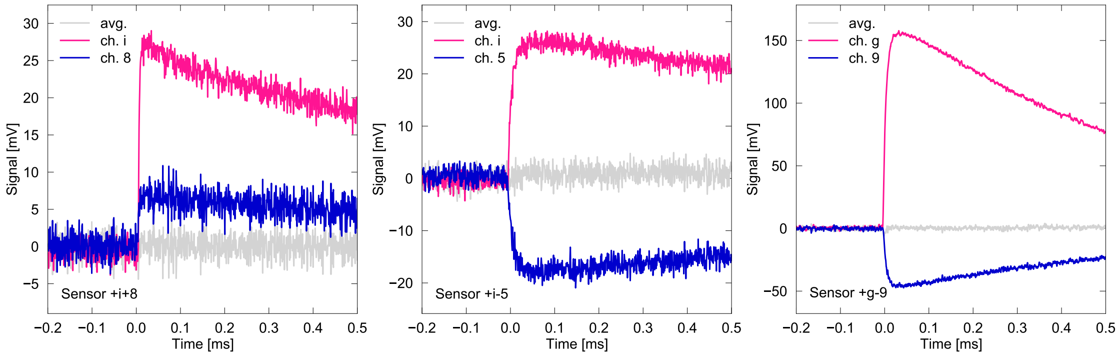

Figure 6.6: Raw data of coincident pulses found in X-ray (**left**, **middle**) and alpha (**right**) measurements. The offset is subtracted from the signals. The pulses from letter channels are shown in pink, the pulses from number channels are shown in blue. The grey line shows the difference of the two normalized signals. The originating sensors are +i+8, +i−5 and +g−9. For an explanation of the varying decay times and relative amplitudes see sections 6.2.5 and 6.2.3.

using template fits. Figure 6.7a) shows the relative amplitudes between channel 5 and i for a measurement of X-ray photons. The ratio between the signal amplitude of channel 5 to channel i is 0.64 ± 0.01, which is the signal height ratio expected in the simulation for respective persistent currents of 75 mA and 32 mA at a detector temperature of 27.5 mK, meaning that the actual number channel current would be 8 mA lower than the nominal current of 40 mA for this measurement. However, the relative amplitudes can vary depending on the channel: Figure 6.7b) shows the relative amplitudes for an alpha measurement, where channels 6 to 10 are compared with the amplitudes of all letter channels. While channel 6, 8 and 9 seem to carry the same persistent current with a relative amplitude of about 0.3 compared to the letter channels, other channels show smaller ratios. A likely reason for that behavior is that the letter channels all carry the same persistent current, while the current in the number channels differs from channel to channel.

To further investigate this behavior, the pulse height at different injected persistent currents was measured, using X-ray photon spectra at a detector temperature of 25 to 30 mK. The average pulse heights for MOCCA channel 8, 13, and i and the corresponding signal heights calculated with the detector simulation are given in figure 6.8, together with the values from the detector simulation for detector temperatures of 25 mK, 27.5 mK and 30 mK. Both channels i and 13 show a good agreement with the simulation up to a persistent current of about 90 mA, approximately following the values for $T = 27.5\,\mathrm{mK}$. Channel 8, in comparison, breaks down at around 30 mA, still showing small signal sizes at higher currents. A possible reason limiting the critical current is the quality of interconnections between the first and the second

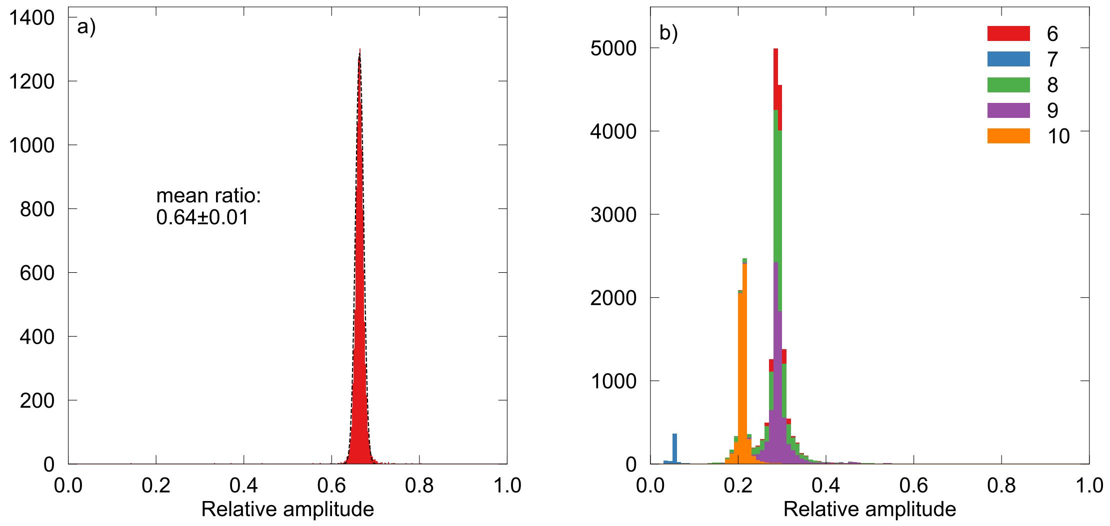

Figure 6.7: Relative amplitudes of selected number channels compared to all letter channels, as determined by a template fit. **(a)** Relative amplitudes between channel 5 and i of a X-ray photon measurement with nominal persistent currents of 75 mA for channel i and 40 mA for channel 5. **(b)** Relative amplitudes between all letter and selected number channels for an alpha particle measurement, shown as a stacked histogram. The nominal persistent current was 80 mA for the letter channels and 25 mA for the number channels.

niobium layer, so-called vias. In total, MOCCA has over 13000 vias, over 2000 of which are non-redundant. These can limit the critical current in single channels, i.e. by dirt or thin insulating layers partially interrupting them. One option for a future version of MOCCA is to create full redundancy for all vias to avoid this limitation, or further increase the size of critical vias.

In general, the results show a good agreement between the measured signal heights and the simulations. For MOCCA V8w1, the letter channels were usually prepared with a current between 65 and 70 mA, a value close to the optimal value found in the simulations for detector temperatures around 15 to 20 mK, and well below the critical current. For the number channels, preparing a current of below 23 mA was chosen for full detector measurements to ensure a sufficient persistent current for all channels.

6.2.4 Hydra principle

After the functionality of the row- and columnwise readout principle has been shown, this section will demonstrate the hydra principle, which is integral for the spatial resolution of MOCCA: As described in chapter 5.1.2, for the MOCCA detector, groups of

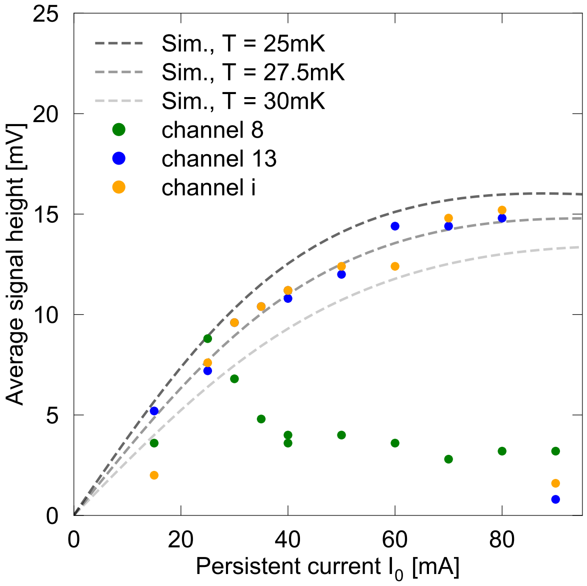

Figure 6.8: Average pulse height for X-ray photons at 5.9keV at different persistent currents for detector channels 8, 13, and i. The pulse heights predicted by the simulation for a detector temperature of 25, 27.5 and 30 mK are given as grey lines.

four absorbers are connected with one sensor, using different thermal conductivities for the connection between the sensor and each absorber. By this, the information which of the absorbers received the signal is encoded in the rise time of the detector signal.

MOCCA V8w1 was designed to have rise times of 4, 8, 12 and 16 µs. Figure 6.9a) shows 1000 signals arriving in sensor +h−5 of MOCCA V8w1, originating from hits on the detector with X-ray photons at an energy of 5.9 keV, measured at a detector temperature of 15 mK to 20 mK. The signals are unfiltered raw data, drawn with a transparency of 90 % and in a color representing the respective hydra absorber. Figure 6.9b) shows the corresponding four template pulses, calculated by averaging over the traces shown in figure 6.9a). From these templates, the signal rise times were determined to be 4.0 µs, 7.0 µs, 11.6 µs and 16.2 µs, showing a good agreement with the designed values.

Due to the fabrication error for MOCCA V8w1 described in section 5.6.1, the rise times can vary for some hydras, with some of the rise times too close together for safe separation. For the intact sensors, however, the different rise times can easily be separated, enabling the full spatial resolution of 4096 pixels, which is demonstrated in section 6.2.10.

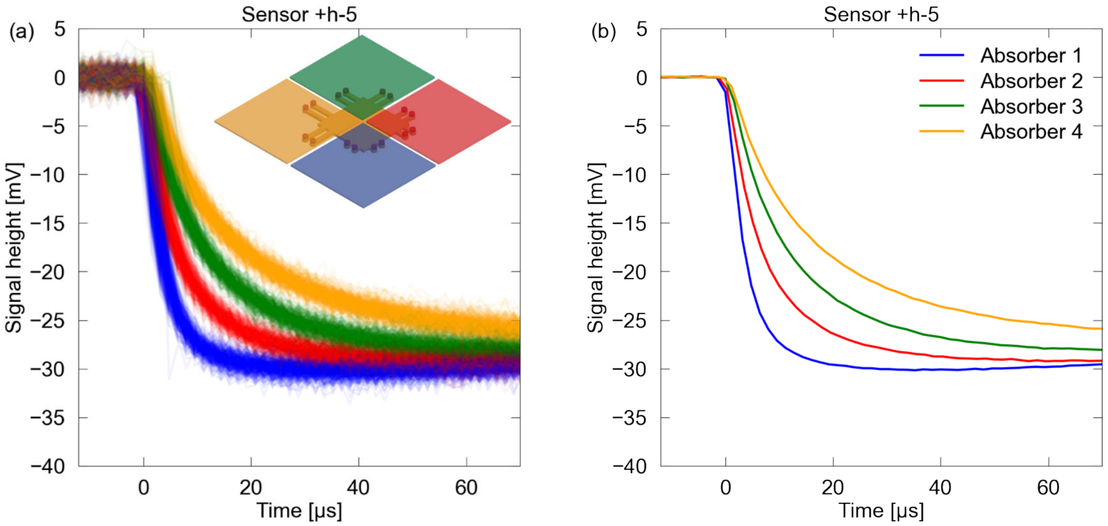

Figure 6.9: (a) Signals caused by 5.9 keV X-ray photons on the four different absorbers of sensor +h−5. The signals from different absorbers are drawn in different colors. **(b)** Averaged traces, calculated from the pulses shown on the left.

6.2.5 Signal decay

A significant difference of MOCCA V8w1 compared to earlier detectors are the gold-filled through-wafer vias, a technique planned to be used on many of the MMC-based detectors within our group, as it provides a uniform thermalization even for large-scale detector arrays. In this section, the decay times of MOCCA V8w1 will be compared to MOCCA V7w2, a detector without through-wafer vias.

MOCCA V8w1 and MOCCA V7w2 have significantly different thermalization behaviors. After the absorption of a particle in MOCCA V7w2, first, the sensor thermalizes with the thermalization pad and the three other hydras sharing the same thermalization pad, as the thermal contact between pad and wafer is comparably weak. Then, the four hydras return slowly to the base temperature by thermalization with the wafer and the copper base of the detector platform. For an earlier MOCCA version, a decay time of 4.8 ms was observed [Gam19]. For MOCCA V8w1, in contrast, each thermalization pad is connected by a gold-filled though-wafer via to the gold-coated back of the wafer. In this case, the decay time should mostly be governed by the designed metallic thermal link between each sensor and the thermalization pad.

Figure 6.10 shows a histogram of the distribution over decay times over a large amount of sensors for both MOCCA V7w2 and MOCCA V8w1. The average decay time for all measured sensors of MOCCA V7w2 is 2.75 ms. The difference to the

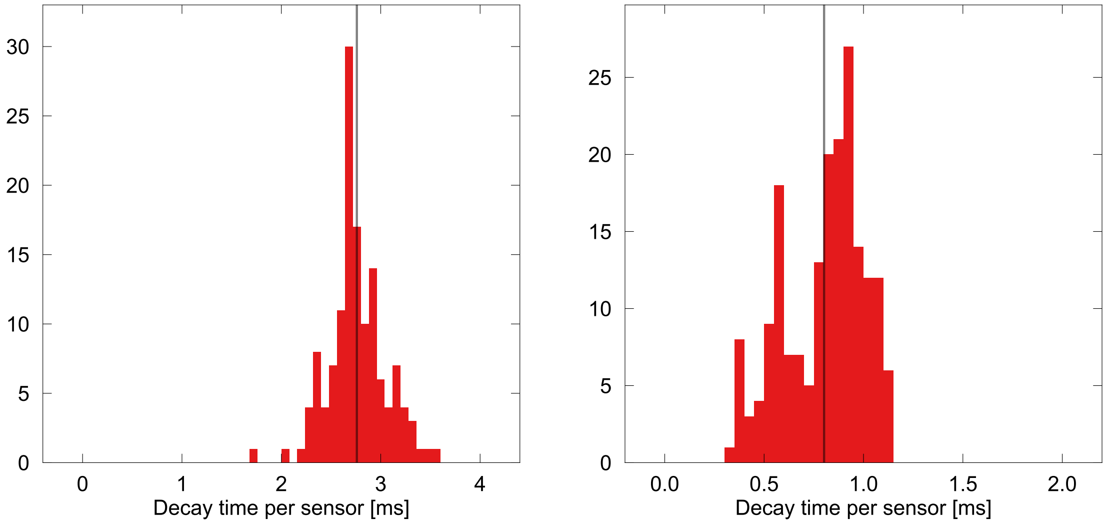

Figure 6.10: Histogram of the decay times of single sensors of MOCCA V7w2 **(left)** and MOCCA V8w1 **(right)**. The grey lines mark the average decay time for all sensors.

detector measured in [Gam19] is due to differences in layer thickness: For MOCCA V7w2, the 70 µm long and 75 µm wide thermal link made of gold has a layer thickness of 500 µm compared to 300 µm in earlier detector versions. With a thermal conductance of $G_{\mathrm{sb}} \approx 9.2\,\mathrm{nW/K}$, the decay time for MOCCA V7w2 is expected to be

$$\tau_{\mathrm{b}} \approx \frac{C_{\mathrm{ges}} \times 3C_{\mathrm{ges}}}{C_{\mathrm{ges}} + 3C_{\mathrm{ges}}} \left(\frac{1}{G_{\mathrm{sb}}} + \frac{1}{3G_{\mathrm{sb}}} \right) = 2.67\,\mathrm{ms}, \tag{6.5}$$

a value close to the measured average.

The average of the decay times of MOCCA V8w1 is 0.78 ms, which is significantly smaller than the ones of MOCCA V7w2. A significant difference between the two detectors is the spread of the values: While the decay times for MOCCA V7w2 mostly lie within 20 % of the mean value, the spread of the values for MOCCA V8w1 is significantly larger, showing a peak at a decay time of 1 ms, but also further peaks at approximately 0.6 ms and 0.3 ms. The distribution of the decay times over the detector is not random: An example for the letter channels i, h and g and the number channels 8, 9 and 10 is given in figure 6.11, with the black lines indicating which of the sensors share the same thermalization pad. As can be seen in the figure, the decay times of groups of sensors sharing the same thermalization pad are typically close to each other, while the decay times can vary significantly from one group of sensors to the next. MOCCA V7w2 does not show this spatial dependency. A possible reason for this behavior was that during the electroplating of the through-wafer vias, MOCCA V8w1 was fully immersed in electroplating liquid for a total

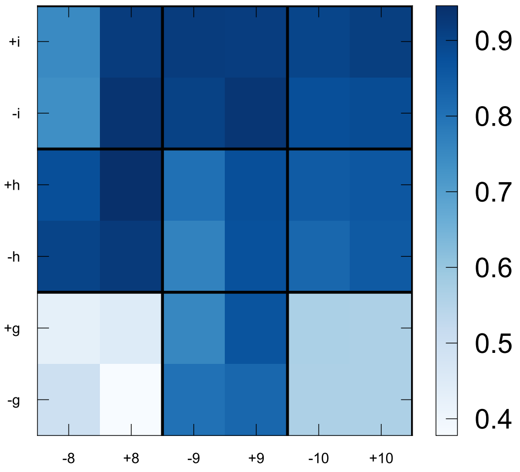

Figure 6.11: Distribution of decay times over 36 sensors on the detector. The decay times are displayed as false colors, the values at the color scale are given in ms. The black lines indicate which groups of four sensors share one common thermalization pad.

of 65 hours. While the front of the detector should be protected by photoresist and being pressed against a flat teflon surface, a galvanization process of this length can attack the photoresist, leading to small amounts of galvanization liquid coming into contact with the thermalization layer on the front of the detector. This behavior was observed in a very pronounced way during the production of another wafer processed after MOCCA V8w1, using the same method. Even depositing small amounts of galvanized gold can lead to significantly faster decay times, as the RRR of the galvanized gold is probably a factor of 3 to 5 higher than the RRR of the sputtered gold of the thermalization layer.

For future detectors, this problem will be avoided: a new electroplating setup was developed, ensuring that the electroplating liquid only comes into contact with one side of the wafer. With this, it will be possible to produce gold-filled through-wafer vias on MOCCA and other MMCs, while ensuring higher uniformity over the detector in the future.

6.2.6 Temperature dependency of rise and decay times

As introduced in section 3.4, the rise and the decay time depend on the heat capacity of the absorbers C_a, the heat capacity of the sensors C_s, the total heat capacity $C_\mathrm{tot} = C_\mathrm{a} + C_\mathrm{s}$ and the thermal conductance between absorber and sensor, G_as, and between sensor and thermal bath, G_sb. The absorber heat capacity C_a and the conductances

G_{as} and G_{sb}[3] are proportional to temperature between 20 and 60 mK. If the sensor heat capacity would be proportional to temperature, too, both relaxation times would be temperature-independent. In fact, C_{s} decreases with increasing temperature, resulting in the observed faster relaxation at higher temperatures.

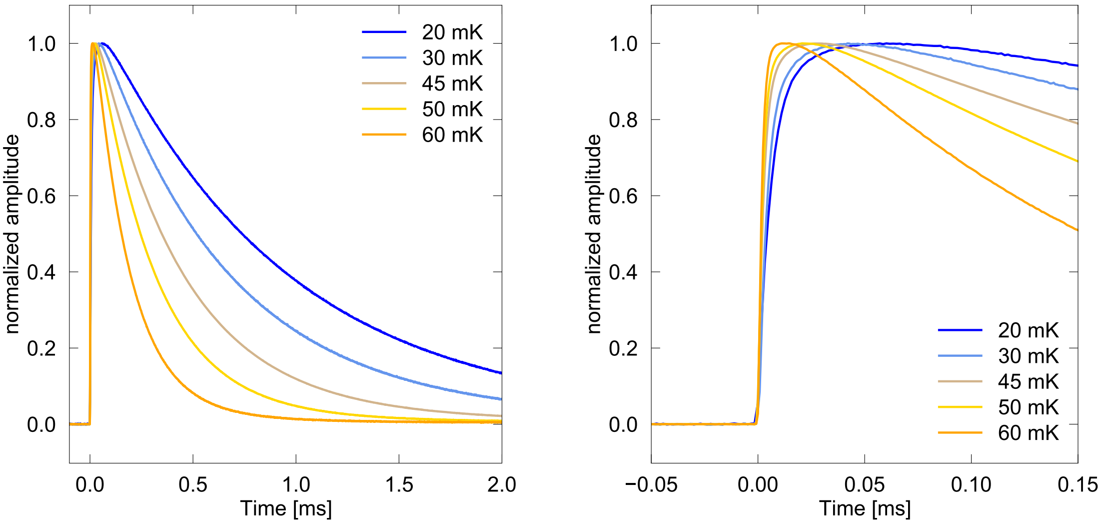

Figure 6.12: Averaged pulses of the second-fastest hydra absorber from sensor +h−8 showing the temperature dependency of rise times **(left)** and decay times **(right)** between 20 and 60 mK. Pulses are taken from a measurement with alpha particles.

Figure 6.12 shows averaged traces for the second-fastest absorber of sensor +h−8 on MOCCA V8w1 at different detector temperatures between 20 mK and 60 mK. For this measurement, alpha particles were used, as they provide signal heights that can still be measured at higher detector temperatures. The rise and decay times for the traces are given in table 6.1. At higher temperatures, the differences between the rise times of a hydra decrease, making it more difficult to differentiate them during analysis.

6.2.7 Cross talk

A central design goal for MOCCA was to minimize the cross talk between columns and rows by using a gradiometric design for the meander-shaped pick-up coils under each sensor, where the lines of the number and letter channels run within a few µm of each other and cross each other. To determine the amount of cross-talk present in MOCCA V8w1, the detector channels 1, 2, 15 and 16 were triggered each time

---

[3] At temperatures above 50 mK, phonons also contribute to G_{sb}.

Temperature	Rise time	Decay time
20 mK	5.9 µs	0.95 ms
30 mK	4.8 µs	0.68 ms
45 mK	2.8 µs	0.45 ms
50 mK	2.3 µs	0.31 ms
60 mK	1.8 µs	0.19 ms

Table 6.1: Rise and the decay time for the second-fastest absorber of the hydra for sensor +h−8 at different temperatures, determined by an exponential fit to the averaged pulses shown in figure 6.12.

any of the letter channels was triggered. To, for example, then determine the cross talk caused by the sensors −i+1 and −i−1 from this data, the traces containing no signal from channel 1, triggered when a pulse of negative polarity was recorded in channel i, are averaged. Any cross talk between the channels would contribute to all the signals recorded in channel 1 and show up in the averaged trace. Therefore, the relative amplitude between the averaged traces from channel i and the averaged traces from channel 1, weighted with the relative signal height of both channels relative to each other as determined in figure 6.7, gives a approximation for the cross talk. The resulting signals for channel −i and 1 are given in figure 6.13. The template fit is shown as a dotted line in the plot on the right.

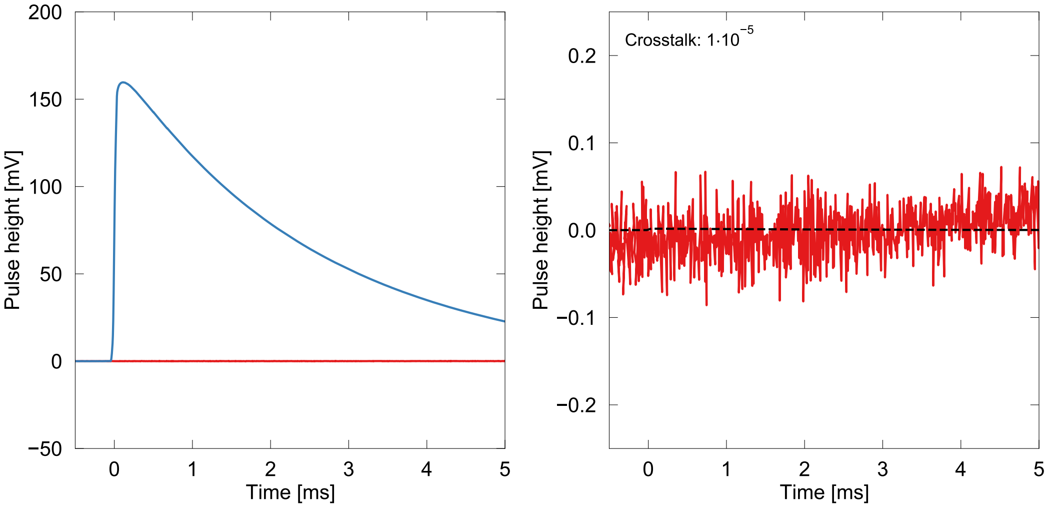

Figure 6.13: **Left:** Averaged traces with negative polarity of channel i (blue, shown inverted) and averaged traces simultaneously triggered on channel 1 (red). **Right:** Averaged traces from channel 1, downsampled by a factor 10, and template fit of the averaged traces from channel i, shown as a dotted black line, with a relative amplitude of 1×10^{-5}.

The averaged trace from channel 1 in figure 6.13 shows no resemblance of a pulse, therefore, the determined value for the crosstalk of 1×10^{-5} can be seen as an upper limit, with the real crosstalk being below the sensitivity of this measurement. The averaged cross talk for all examined channels is 2.5×10^{-5}, which is significantly below values that would influence measurements with MOCCA. Therefore, the care taken during design, minimizing the cross talk between channels, paid off, and cross talk in MOCCA can be neglected.

6.2.8 Linearity

As the heat capacity of the detector and the magnetization are approximately constant for the temperature difference caused by the absorption of an X-ray photon in an absorber, the signal amplitude of an MMC should be approximately linear to the energy of the incoming particle. Deviations from the linear behavior can be approximately described by a simple quadratic function

$$A(E) = aE + bE^2 = a\left(1 - \frac{E}{E^*}\right)E, \tag{6.6}$$

with the coefficient $E^* = -a/b$ describing the relative non-linearity.

Figure 6.14 (top) shows the relative amplitude of the K_α and the K_β line for the four absorbers of sensor +i−5, with the respective fits of equation 6.6. As the fits are so close to a perfectly linear behavior, they can hardly be distinguished from each other. Figure 6.14 (bottom) shows the deviation from the linear behavior for the four absorbers on average, given in eV. At an energy of 6.49 keV, the relative deviations are (0.6±0.2) %. Due to the margin of error and only two data points being included in the fit, more data is needed to determine the linearity with a smaller margin of error. Still, the detector shows an excellent linearity, and calculations in [Gam19] show that, even at particle energies present at the CSR, the non-linearity is expected to be below 5 %, and the non-linearity can easily be corrected using equation 6.6.

6.2.9 Energy resolution

The ^{55}Fe source emits X-ray photons at energies of approximately 5.9 keV and 6.5 keV. To measure the energy spectrum with MOCCA, the detector was prepared with a persistent current of nominally 70 mA on the letter channels and 45 mA on the number channels. To keep the detector temperature as low as possible, all but four front-end SQUIDs were turned off, leading to an effective detector temperature of about 15 mK to 20 mK. Signals from sensor +i−5 were sorted by rise time, as demonstrated in section 6.2.4. Then, the pulses were fitted using a template pulse generated by averaging over traces from the respective absorber in the time interval

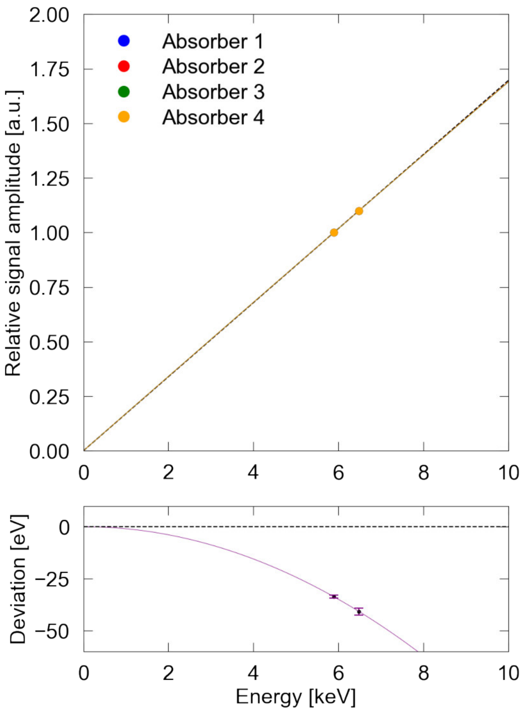

Figure 6.14: Top: Relative measured signal amplitude of the 5.9 keV K_α and the 6.49 keV K_β peak of ^{55}Fe, normalized to the K_α amplitude, for the four absorbers of +i−5. A completely linear behavior is indicated by the dashed line. For all four absorbers, a data was fitted to equation 6.6. The resulting fits are shown, but superimpose each other. **Bottom:** Average derivation from a linear behavior for all four absorbers.

$[-0.6\,\mathrm{ms}, 0.6\,\mathrm{ms}]$ around the trigger time. With the K_α line as a gauge line, figure 6.15 shows the resulting spectra for the four absorbers of hydra +i−5. For each K_α line, a normal distribution was fitted to the data. The corresponding values for the full-width at half maximum energy resolution are given in the respective plots and were determined to be 87 eV, 88 eV, 87 eV and 89 eV. This energy resolution is close to the energy resolution of 64 eV predicted by the detector simulation for the actual parameters and properties of the detector.

In the energy spectrum for absorber 1 in figure 6.15, two additional peaks show up, which are shown in pink. Regarding relative amplitudes and occurrence, they resemble the K_α and K_β line of ^{55}Fe, shifted to higher energies. Their pulse shape exhibits a slightly faster rise times compared to the regular traces of this absorber. These signals are very likely direct sensor hits. As all energy is immediately deposited in the sensor, those pulses initially reach a higher amplitude before thermalizing with the four absorbers. For that reason, they appear to have higher relative energies. While the rise time for those traces normally should be significantly faster than

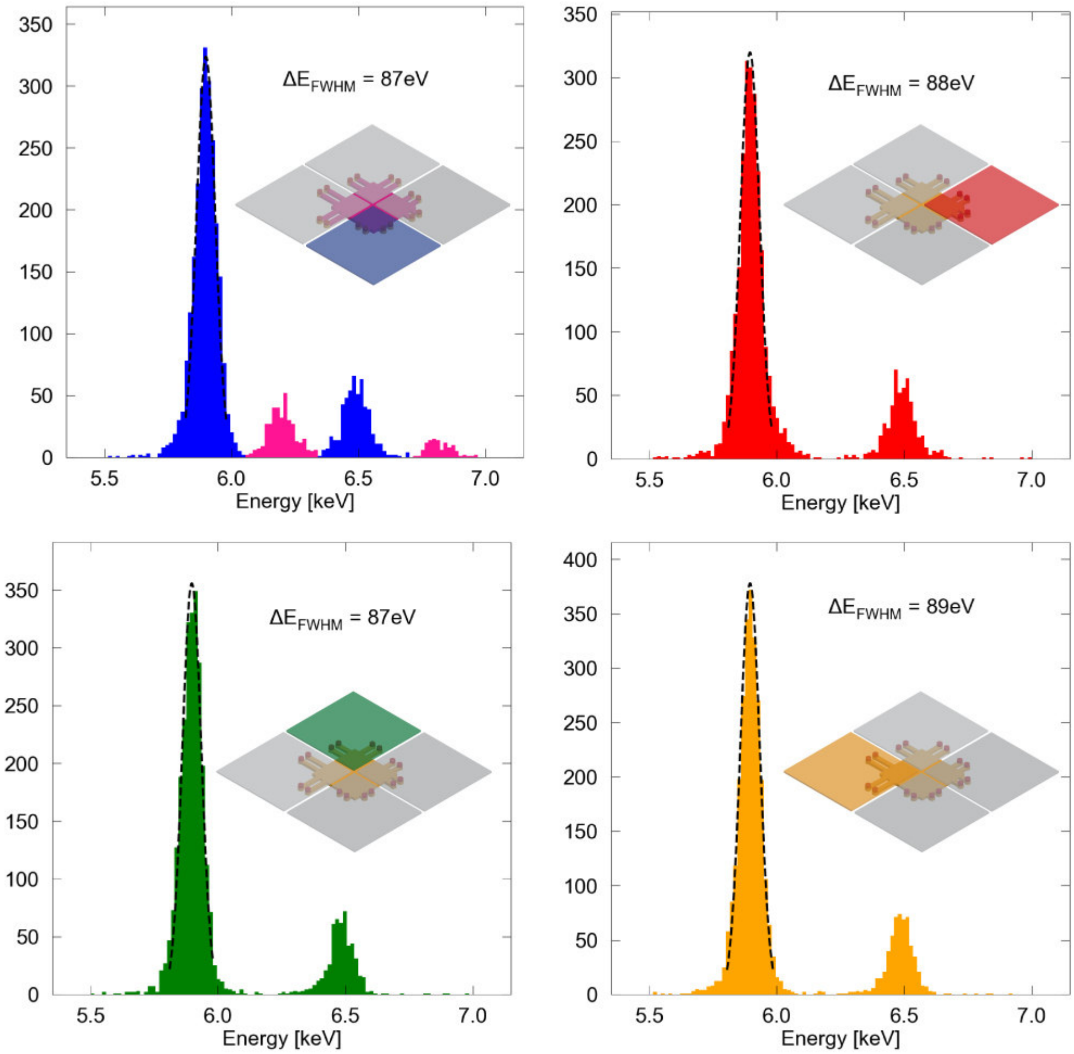

Figure 6.15: Measured energy spectra of X-ray photons from the ^{55}Fe source using sensor +i−5 from MOCCA V8w1, split up by the four absorbers. The K_α peak for each absorber was fitted with a Gaussian distribution, with the full-width half-maximum energy resolution ΔE_{FWHM} of the peak shown in each graph. The spectra were recorded at a temperature of approximately 15 mK, using a persistent current of 70 and 45 mA, respectively.

the fastest signal rise time of absorber hits, the chosen bandwidth of the SQUID FLL-circuit for this measurement was relatively low, making the rise time hard to distinguish from the rise times of the fastest signal from an absorber. Sensor hits can occur in one of two ways: either the photons directly hit the sensor through the narrow slits between the absorbers, or they pass through the absorbers and then get absorbed in the sensor. At an absorber thickness of 4 µm and 4 µm space between the absorbers, about 0.6 % of the hits are expected to be sensor hits. As the relative rate for the hits shown in figure 6.15 is closer to 3 %, this might hint at a slightly lower absorber thickness than designed or a damage of the absorbers over that sensor.

A possible explanation for the difference between the measured and the calculated energy resolution was the use of auxiliary stems for additional stability of the absorbers. As they are in direct contact with the substrate, at those points, phonons can escape into the substrate, not contributing to the detector signal. Another possible reason causing a broadening of the energy resolution are small temperature fluctuations during the measurement. As MOCCA, in opposition to other detectors, has no channels specifically designed to be used for temperature measurement, small variations in the operational temperature cannot easily be detected, even though variations as small as 0.1 mK can already lead to a 0.4 % change in corresponding signal height.

The excellent energy resolution determined for MOCCA in this section is about a factor three better than previously measured energy resolutions for a previous version of the MOCCA detector [Gam19] and close to the energy resolution of 64 eV, predicted by the detector simulation for the actual parameters and properties of the detector. The improvement possibly results from the improved design and fabrication of the detector: due to the improved connections between the first and second niobium layer, a higher persistent current can be prepared in the detector. The increase of the rise times for MOCCA V8w1 also improved the energy resolution. The high rate on the detector allowed a shorter measurement time, leading to less variations of the cryostat temperature. Additionally, the gold-filled through-wafer vias ensured a good thermalization of the detector.

The alpha source was used to further investigate signal shapes at higher deposited energies. However, a quantitative energy resolution or spectra cannot be determined from the measurements, as determined by SRIM[4] calculations: at alpha energies around 5.5 keV, the absorption depth inside the material was calculated to be 9.44 µm, far above the absorber thickness of 4 µm. Of 1000 simulated alpha events, none was predicted to be fully absorbed inside the absorber. Therefore, in all detected pulses the alpha particle deposited only a fraction of its kinetic energy inside the absorber. Future MOCCAs intended for alpha spectroscopy therefore have to be produced with somewhat higher absorber thickness.

6.2.10 Measurements with collimator

After demonstrating the functionality of the row- and columnwise readout, the full functionality of the hydra principle and the excellent energy resolution of MOCCA,

---

[4] SRIM is the **S**topping and **R**ange of **I**ons in **M**atter software package, software written by James F. Ziegler [Zie10]. The simulation was done by Lisa Gamer.

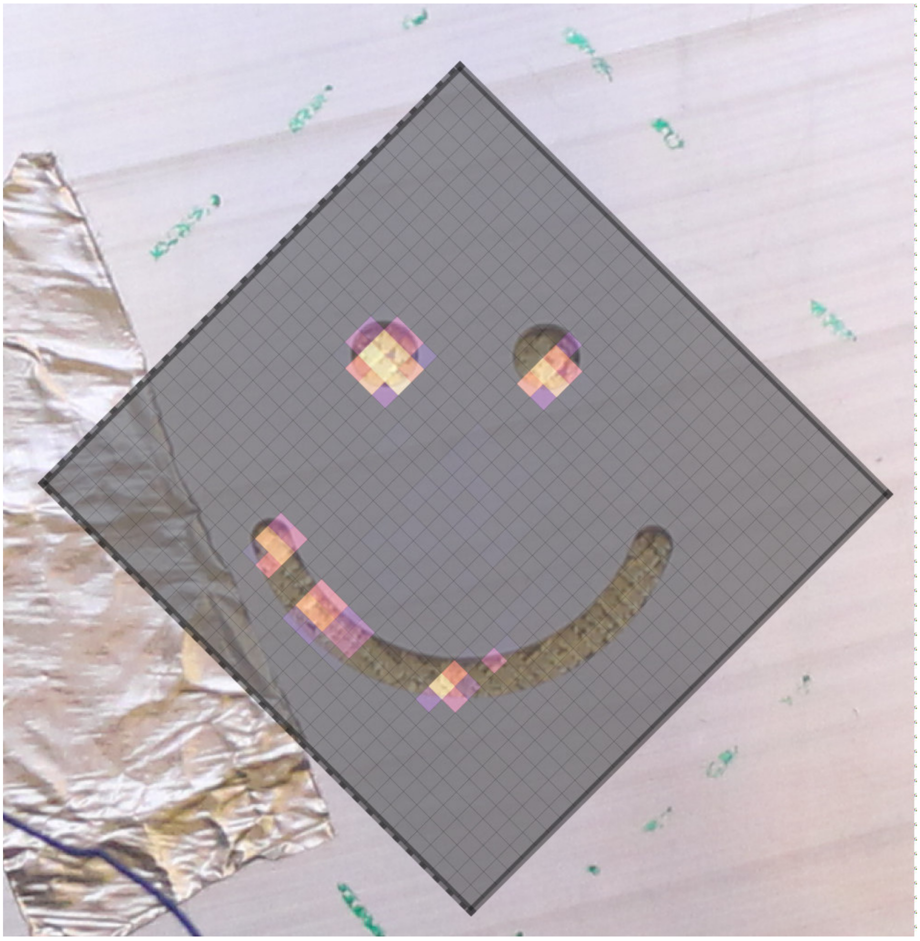

Figure 6.16: Picture of the MOCCA setup with the mounted smiley collimator. Superimposed on the position of the detector is a plot of the resulting spatial distribution of hits measured on the detector, showing a sensor resolution of 32×32 pixels. More details on the measurement are given in the text.

this chapter demonstrates a successful use of MOCCA as a camera.

To demonstrate this, the ^{55}Fe source was placed so that it illuminates the full detector setup, while a collimator was mounted on the detector. The measured data was filtered, and coincident pulses were identified. This allows to determine a sensor-resolved hit rate on the detector with a resolution of 32×32 pixel. The resulting sensor-resolved hit map is shown in 6.16, superimposed on a picture of the detector with the collimator. The sensors receiving the most hits are shown as yellow, while the sensors receiving little to no hits are shown as grey. As one of the ADCs used for this measurement was partially defect, reducing the signal height of half of the channels to 10 %, no hits were detected in about half of the detector, which was noticed after the measurement campaign. However, this stems from an instrumental defect and not from the detector itself. A new measurement campaign to measure this picture with the full detector is in preparation, and for the functional channel, the eyes and the mouth of the smiley are correctly reconstructed in the plot.

To reach the full resolution of MOCCA, the four absorbers of each hydra have to be distinguished. For this, an integral over the rising part of the signals up to 95 % of the pulse maximum was used, yielding small values for fast rise times and large values for slow rise times. For MOCCA V8w1, the identification of the four absorbers of each hydra was done manually for about 10 % of the sensors, as the manufacturing error described in section 5.6.1 lead to varying rise times for some of the sensors.

Figure 6.17 (bottom) shows a plot with hydra resolution for the alpha source. As a bonding wire detached from the PCB during cooldown, no data could be recorded for MOCCA channel 11, corresponding to rows 41-44 in figure 6.17 (bottom). However, as this was the only channel not recording traces in this measurement, it is possible to attribute all unmatched traces to channel 11. As the polarity information from channel 11 is missing, these trace numbers were distributed equally over all eight possible absorbers. Figure 6.17 (top) shows the distribution of hits, averaged over MOCCA channel 9, which is equal to row 33 to 36 in the plot. The distribution of hits follows the expected distribution for a disc source, with the source area given in the plot for reference.

These measurements show the immense capabilities of MOCCA: the ability for spatially resolved measurements of massive particles with excellent energy resolution, as demonstrated in section 6.2.9, and the large detection area of 4.5 cm × 4.5 cm fully qualify for the demanding experimental conditions at the CSR, but also for a large range of other experiments that need imaging capabilities. Measurements showing more complex imaging capabilities are currently in preparation. In conclusion, MOCCA is the largest MMC-based detector, and by matching the absorber thickness to the desired alpha energy, MOCCA is also the largest high-resolving alpha detector world-wide.

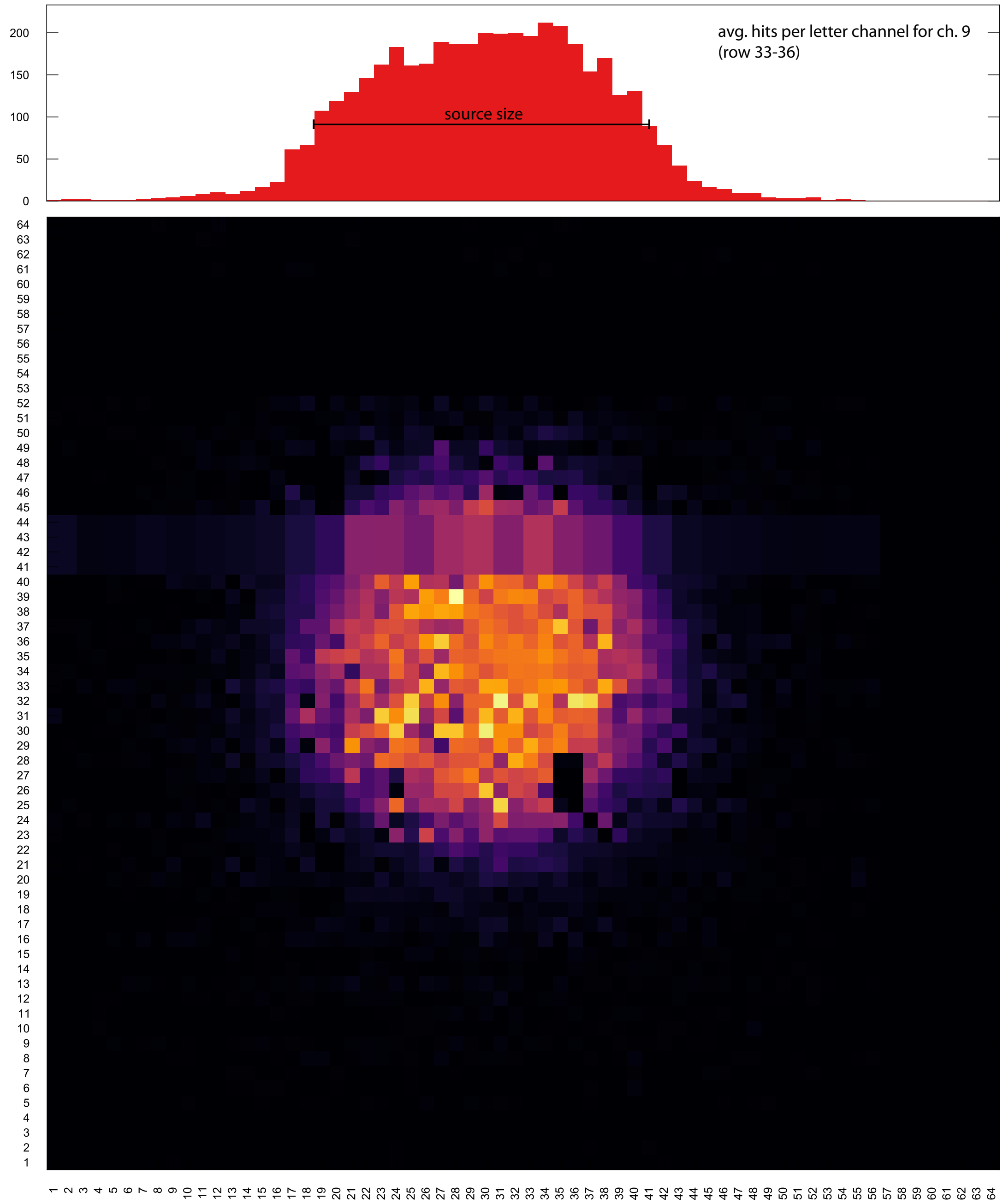

Figure 6.17: Top: Average hits per letter channel for MOCCA channel 9, which is equivalent to rows 33 to 36 in the bottom plot. The size of the active area of the Am disc source is given in the plot. **Bottom:** Plot of the amount of hits per MOCCA pixel for the alpha source mounted in a distance of approximately 1 mm in front of and in parallel to the detector, as shown in figure 5.29 b), showing the total MOCCA resolution of 64 × 64 pixels. The values for row 41 to 44 were reconstructed, as described in the text.

7. Conclusion

The molecule camera MOCCA, a 4096-pixel detector based on metallic magnetic calorimeters (MMCs) with a detection area of 4.5 cm × 4.5 cm, was described and characterized within this thesis. Together with the developed measurement infrastructure and using the newly implemented algorithms for data analysis, MOCCA was shown to be a versatile tool for the energy-resolving detection of neutral massive particles where a good spatial resolution and a large detection area are required. MOCCA was designed for deployment at the Cryogenic Storage Ring CSR at the Max Planck Institute for Nuclear Physics in Heidelberg, a ring enabling the investigation of reaction networks in interstellar molecular clouds [vH16].

MOCCA is a detector based on MMCs, optimized for measuring massive molecule fragments. At CSR, it will enable resolving the full kinetics of dissociative recombination even for complex systems. To reduce the amount of readout channels needed for MOCCA, two readout principles were used: Firstly, a summed-signals row- and columwise readout means that every particle hit on the detector leads to two seperate and independent pulses, one in the respective column, one in the row. Secondly, the so-called hydra principle uses the rise time of the signal to encode which one of a group of four pixels was hit. Through the use of these principles, it was possible to reduce the readout to 32 SQUID channels. In simulations, it was shown that MOCCA is able to reach an intrinsic energy resolution of 50 eV. For the fabrication, a number of processes were developed within this thesis, creating an array of 16 by 16 gold-filled through-wafer vias contacting the detector with the backside of the chip. This ensures good thermalization throughout the detector.

To characterize MOCCA and run other MMC-based detectors in cryostats, a standardized readout infrastructure for up to 36 SQUID channels was developed, enabling quick mounting and connecting of setups to the cryostat. For the planned setup of MOCCA at the CSR, a MOCCA-specialized setup was developed. It allows for MOCCA to be inside the beam tube, while most of the measurement infrastructure is in the less sensitive isolation vacuum of CSR.

A central problem during measurements with MMCs is the sensitivity to eletromagnetic radiation such as GSM signals, e.g. emitted by mobile phones. When analyzing the pulse data, some of those pulses are hard to distinguish from low-amplitude pulses, leading to incorrect energy spectra. A complete removal of those traces is necessary before applying further data analysis. A range of different filters was developed to flag those signals, only based on the information when the respective pulses were recorded. Using vectorized calculations, those filters were fast during calculation and were shown to remove noise with high precision, filtering minimal amounts of real pulses. These filters were further developed and are now used on other MMC-type detectors.

The most recently produced MOCCA detector demonstrates all functionalities needed for the demanding experiments at CSR. The full functionality of the readout system was shown. With the exception of a few pixels damaged by a production error, the hydra principle works and enables the reconstruction of the pixel hit by a particle. The gold-filled vias couple the sensors to the thermal bath provided by the cryostat. While a variation in signal decay times over the detector was observed, the origin of the variation will likely be fixed by a new electroplating setup. The cross-talk between lines and columns of the detector is below 2.5×10^{-5} on average and, with that, far below levels that would compromise the function of the detector, confirming that the gradiometric design of the detector works. The energy resolution for X-ray photons was determined to be 88 eV on average, an excellent energy resolution improving the resolution measured in [Gam19] approximately by a factor three. For X-ray photons, MOCCA shows a very low relative non-linearity of 0.1 %. The spatial resolution is demonstrated by showing heatmaps for the hits on detector, correlating with the respective source and collimator shape above the detector.

For future measurements, further demonstrations of the energy and spatial resolution will be carried out, collecting more data on alpha measurements and proving more complex imaging capabilities. It is planned to produce further wafers of MOCCA, getting rid of the production error spoiling some of the hydra measurements and producing more uniform gold-filled through-wafer vias. Finally, MOCCA will be installed at the Max Planck Institute as soon as a new detector and the detector setup at CSR are finished.

The results demonstrated in this thesis show the large potential of MOCCA: Its ability to measure neutral massive particles on its detection area of more than $20\,\mathrm{cm}^2$ with a spatial resolution below a millimeter and an outstanding energy resolution is a unprecedented and powerful tool for high-precision research.

Bibliography

[Abr70] A. Abragam and B. Bleaney, Electron paramagnetic resonance of transition ions, Claredon Press, Oxford, 1970.

[Ada41] W. S. Adams, Some Results with the COUDÉ Spectrograph of the Mount Wilson Observatory, *The Astrophysical Journal*, **93**(638), 11, 1941.

[All17] S. Allgeier, Entwicklung einer modularen 36-Kanal-Auslesekette mit rauscharmen SQUID-basierten Vorverstärkern für die 4k-Pixel-Molekülkamera MOCCA, PhD Thesis, Universität Heidelberg, 2017.

[Ban93] S. R. Bandler, C. Enss, R. E. Lanou, H. J. Maris, T. More, F. S. Porter, and G. M. Seidel, Metallic magnetic bolometers for particle detection, *Journal of Low Temperature Physics*, **93**(3-4), 709–714, 1993.

[Ban19] S. R. Bandler, J. A. Chervenak, A. M. Datesman, S. J. Smith, T. R. Stevenson, D. Bennett, D. Swetz, J. N. Ullom, K. D. Irwin, M. E. Eckart, E. Figueroa-Feliciano, and D. McCammon, Lynx x-ray microcalorimeter, *J. Astron. Telesc. Instrum. Syst.*, **5**(2), 021017, 2019.

[Bar21] A. Barth and R. Hammann, Data reduction for a calorimetrically measured 163Ho spectrum of the ECHo experiment, *to be submitted*, 2021.

[Biz20] L. Bizzocchi, D. Prudenzano, V. M. Rivilla, A. Pietropolli-Charmet, B. M. Giuliano, P. Caselli, J. Martín-Pintado, I. Jiménez-Serra, S. Martín, M. A. Requena-Torres, F. Rico-Villas, S. Zeng, and J. C. Guillemin, Propargylimine in the laboratory and in space: Millimetre-wave spectroscopy and its first detection in the ISM, *Astronomy and Astrophysics*, **640**, 2020.

[Bru82] J. J. Bruines, V. J. de Waal, and J. E. Mooij, Comment on: "Dc SQUID: Noise and optimization" by Tesche and Clarke, *Journal of Low Temperature Physics*, **46**(3-4), 383–386, 1982.

[Bue88] M. Buehler and E. Umlauf, A magnetic bolometer for single-particle detection, *Europhysics Letters*, **297**, 1988.

[Bue93] M. Buehler, T. Fausch, and E. Umlauf, Measurement of spin-lattice relaxation times at millikelvin temperatures, *Europhysics Letters*, **23**(7), 529–534, 1993.

[Bur04] A. Burck, Entwicklung großflächiger magnetischer Kalorimeter zur energieaufgelösten Detektion von Röntgenquanten und hochenergetischen Teilchen, PhD Thesis, Universität Heidelberg, 2004.

[Cam10] J. Cami, J. Bernard-Salas, E. Peeters, and S. Malek, Detection of C60 and C70 in a Young Planetary Nebula, *Science*, **329**, 1180–1182, 2010.

[Cla04] J. Clarke, The SQUID Handbook. Vol. 1, Fundamentals and Technology of SQUIDS and SQUID Systems, Wiley-VCH, 2004.

[Cra02] G. Craciun, M. Blauw, E. van der Drift, P. Sarro, and P. French, Temperature influence on etching deep holes with SF6/O2 cryogenic plasma, *Journal of Micromechanics and Microengineering*, **12**, 390–394, 2002.

[Dan05] T. Daniyarov, Metallische magnetische Kalorimeter zum hochauflösenden Nachweis von Röntgenquanten und hochenergetischen Molekülen, PhD Thesis, Universität Heidelberg, 2005.

[De 75] H. De Waard, The investigation of radiation damage and lattice location by nuclear hyperfine interaction techniques, *Physica Scripta*, **11**(3-4), 157–166, 1975.

[De 17] S. E. De Graaf, A. A. Adamyan, T. Lindström, D. Erts, S. E. Kubatkin, A. Y. Tzalenchuk, and A. V. Danilov, Direct Identification of Dilute Surface Spins on Al2 O3: Origin of Flux Noise in Quantum Circuits, *Physical Review Letters*, **118**(5), 1–5, 2017.

[Dus04] R. Dussart, M. Boufnichel, G. Marcos, P. Lefaucheux, A. Basillais, R. Benoit, T. Tillocher, X. Mellhaoui, H. Estrade-Szwarckopf, and P. Ranson, Passivation mechanisms in cryogenic SF6/O2 etching process, *Journal of Micromechanics and Microengineering*, **14**(2), 190–196, 2004.

[Fau93] T. Fausch, M. Buehler, and E. Umlauf, Signal rise time of the magnetic bolometer, *Journal of Low Temperature Physics*, **93**(3-4), 703–708, 1993.

[Fel01] P. A. Feldman, Molecular astronomy from a Canadian perspective: The early years, *Canadian Journal of Physics*, **79**(2-3), 89–100, 2001.

[Fle00] A. Fleischmann, J. Schönefeld, and J. Sollner, Low temperature properties of erbium in gold, *Journal of Low Temperature Physics*, **118**(1/2), 7–21, 2000.

[Fle03] A. Fleischmann, Magnetische Mikrokalorimeter: Hochauflösende Röntgenspektroskopie mit energiedispersiven Detektoren, PhD Thesis, Universität Heidelberg, 2003.

[Fle05] A. Fleischmann, C. Enss, and G. M. Seidel, Metallic magnetic calorimeters, in C. Enss (Ed.), *Cryogenic Particle Detection*, Volume 99, 151–216, Springer, 2005.

[Fle09] A. Fleischmann, L. Gastaldo, S. Kempf, A. Kirsch, A. Pabinger, C. Pies, J. P. Porsf, P. Ranitzsch, S. Schäfer, F. V. Seggern, T. Wolf, C. Enss, and G. M. Seidel, Metallic magnetic calorimeters, *AIP Conference Proceedings*, **1185**, 571–578, 2009.

[For19] F. Forndran, Optimization of Si deep etching and fabrication of the first P2 detector with trenches, Master thesis, Universität Heidelberg, 2019.

[Fra76] S. Fraga, J. Karwowski, and K. Saxena, Handbook of atomic data, Elsevier Scientific Publishing Company, New York, 1976.

[Fuk10] Y. Fukui and A. Kawamura, Molecular Clouds in Nearby Galaxies, *Annual Review of Astronomy and Astrophysics*, **48**(1), 547–580, 2010.

[Gam13] L. Gamer, Ein großflächiges magnetisches Kalorimeter zur energie- und ortsauflösenden Detektion von Molekülfragmenten, Master thesis, Universität Heidelberg, 2013.

[Gam17] L. Gamer, C. E. Düllmann, C. Enss, A. Fleischmann, L. Gastaldo, C. Hassel, S. Kempf, T. Kieck, and K. Wendt, Simulation and optimization of the implantation of holmium atoms into metallic magnetic microcalorimeters for neutrino mass determination experiments, *Nuclear Instruments and Methods in Physics Research, Section A: Accelerators, Spectrometers, Detectors and Associated Equipment*, **854**(February), 139–148, 2017.

[Gam19] L. Gamer, Entwicklung und Charakterisierung des 4k-Pixel Detektorarrays MOCCA für die energie- und ortsaufgelöste Detektion neutraler Molekülfragmente, PhD Thesis, Universität Heidelberg, 2019.

[Gas17] L. Gastaldo, K. Blaum, K. Chrysalidis, T. Day Goodacre, A. Domula, M. Door, H. Dorrer, C. E. Düllmann, K. Eberhardt, S. Eliseev, C. Enss, A. Faessler, P. Filianin, A. Fleischmann, D. Fonnesu, L. Gamer, R. Haas, C. Hassel, D. Hengstler, J. Jochum, et al., The electron capture in 163Ho experiment ECHo, *European Physical Journal: Special Topics*, **226**(8), 1623–1694, 2017.

[Gei20] J. Geist, Bestimmung der Isomerenergie von 229Th mit dem hochauflösenden Mikrokalorimeter-Array maXs30, PhD Thesis, Universität Heidelberg, 2020.

[Hah92] W. Hahn, M. Loewenhaupt, and B. Frick, Crystal field excitations in dilute rare earth noble metal alloys, *Physica B: Condensed Matter*, **180-181**, 176–178, 1992.

[Har04] J. Hartmann, Investigations on the spectrum and orbit of delta orionis, *Astrophysical Journal*, **19**, 268–286, 1904.

[Hen17] D. Hengstler, Development and characterization of two-dimensional metallic magnetic calorimeter arrays for the high-resolution X-ray spectroscopy, PhD Thesis, Universität Heidelberg, 2017.

[Her22] M. Herbst, to be submitted, PhD Thesis, Universität Heidelberg, 2022.

[Isa65] L. L. Isaacs, Low-Temperature Specific Heat of Gold, Silver and Copper, *J. Chem. Phys*, **43**, 307, 1965.

[Jan96] H. Jansen, H. Gardeniers, M. De Boer, M. Elwenspoek, and J. Fluitman, A survey on the reactive ion etching of silicon in microtechnology, *Journal of Micromechanics and Microengineering*, **6**(1), 14–28, 1996.

[Jan09] H. V. Jansen, Black silicon method X : a review on high speed and selective plasma etching of silicon with profile control : an in-depth comparison between Bosch and cryostat DRIE processes as a roadmap to next generation equipment, *Journal of Micromechanics and Microengineering*, **19**, 2009.

[Jia12] F. Jiang, A. Keating, M. Martyniuk, K. Prasad, L. Faraone, and J. Dell, Characterization of low-temperature bulk micromachining of silicon using an SF 6 / O 2 inductively coupled plasma, *Journal of Micromechanics and Microengineering*, **22**(095005), 2012.

[Jos62] B. D. Josephson, Possible new effects in superconductive tunnelling, *Physics Letters*, **1**(July), 7–9, 1962.

[Kam10] A. Kampkötter, Design-Studie und Entwicklung eines großflächigen metallisch magnetischen Kalorimeters zur orts- und energieauflösenden Detektion von hochenergetischen Molekülfragmenten, PhD Thesis, Universität Heidelberg, 2010.

[Kas56] T. Kasuya, A Theory of Metallic Ferro- and Antiferromagnetism on Zener's Model, *Progress of Theoretical Physics*, **16**(1), 45–57, 1956.

[Kem16] S. Kempf, A. Ferring, and C. Enss, Towards noise engineering: Recent insights in low-frequency excess flux noise of superconducting quantum devices, *Applied Physics Letters*, **109**(16), 2016.

[Kem17] S. Kempf, M. Wegner, A. Fleischmann, L. Gastaldo, F. Herrmann, M. Papst, D. Richter, and C. Enss, Demonstration of a scalable frequency-domain readout of metallic magnetic calorimeters by means of a microwave SQUID multiplexer, *AIP Advances*, **7**(1), 2017.

[Kim20] G. B. Kim, S. T. Boyd, R. H. Cantor, A. S. Voyles, J. T. Morrell, L. A. Bernstein, and S. Friedrich, A New Measurement of the 60keV Emission from Am-241 Using Metallic Magnetic Calorimeters, *Journal of Low Temperature Physics*, **199**(3-4), 1055–1061, 2020.

[Koc07] R. H. Koch, D. P. Divincenzo, and J. Clarke, Model for 1/f flux noise in SQUIDs and qubits, *Physical Review Letters*, **98**(26), 1–4, 2007.

[Kog81] S. M. Kogan, 1/F Noise in Spin Glasses and in the Disordered Kinetic Ising Model, *Solid State Communications*, **38**(11), 1015–1018, 1981.

[Kra20] M. Krantz, Development of a metallic magnetic calorimeter with integrated SQUID readout, PhD Thesis, Universität Heidelberg, 2020.

[Kre19] H. Kreckel, O. Novotny, and A. Wolf, Astrochemical studies at the Cryogenic Storage Ring, *Philosophical Transactions of the Royal Society A: Mathematical, Physical and Engineering Sciences*, **377**(2154), 2019.

[Kre20] J. Krełowski, G. A. Galazutdinov, and R. Siebenmorgen, On the Relation between Diffuse Bands and Other Interstellar Features, *The Astrophysical Journal*, **899**(1), L2, 2020.

[Kum16] P. Kumar, S. Sendelbach, M. A. Beck, J. W. Freeland, Z. Wang, H. Wang, C. C. Yu, R. Q. Wu, D. P. Pappas, and R. McDermott, Origin and Reduction of 1 /f Magnetic Flux Noise in Superconducting Devices, *Physical Review Applied*, **6**(4), 1–5, 2016.

[Lar12] M. Larsson, W. D. Geppert, and G. Nyman, Ion chemistry in space, *Reports on Progress in Physics*, **75**(6), 2012.

[Lou74] O. Lounasmaa, Experimental Principles and Methods Below 1 K, Academic Press, 1974.

[Mar73] D. L. Martin, Specific Heat of Copper, Silver and Gold below 30 K, *Phys. Rev. B*, **8**(12), 1973.

[McG20] B. A. McGuire, A. M. Burkhardt, R. A. Loomis, C. N. Shingledecker, K. L. Kelvin Lee, S. B. Charnley, M. A. Cordiner, E. Herbst, S. Kalenskii, E. Momjian, E. R. Willis, C. Xue, A. J. Remijan, and M. C. McCarthy, Early Science from GOTHAM: Project Overview, Methods, and the Detection of Interstellar Propargyl Cyanide in TMC-1, *The Astrophysical Journal*, **900**(1), L10, 2020.

[McK40a] A. McKellar, Evidence for the molecular origin of some hitherto unindentified interstellar lines, *Publications of the Astronomical Society of the Pacific*, **52**(307), 187–192, 1940.

[McK40b] A. McKellar, Wave Lengths of the CH Band Lines, *Publications of the Astronomical Society of the Pacific*, **52**(309), 312–318, 1940.

[Mel05] X. Mellhaoui, R. Dussart, T. Tillocher, P. Lefaucheux, P. Ranson, M. Boufnichel, and L. J. Overzet, SiO xF y passivation layer in silicon cryoetching, *Journal of Applied Physics*, **98**(10), 2005.

[Mer34] P. W. Merrill, Unidentified interstellar lines, *Publications of the Astronomical Society of the Pacific*, **46**(272), 206–207, 1934.

[Möh15] G. Möhl, Optimierung von Ionenätzprozessen zur Herstellung metallischer magnetischer Kalorimeter, Bachelor thesis, Universität Heidelberg, 2015.

[Mül01] H. Müller, S. Thorwirt, D. Roth, and G. Winnewisser, The Cologne Database for Molecular Spectroscopy , CDMS, *Astronomy & Astrophysics*, **370**, 49–52, 2001.

[Mül05] H. Müller, F. Schlöder, J. Stutzki, and G. Winnewisser, The Cologne Database for Molecular Spectroscopy, CDMS: A useful tool for astronomers and spectroscopists, *Journal of Molecular Structure*, **742**(1-3), 215–227, 2005.

[Nak17] Y. Nakano, Y. Enomoto, T. Masunaga, S. Menk, P. Bertier, and T. Azuma, Design and commissioning of the RIKEN cryogenic electrostatic ring (RICE), *Review of Scientific Instruments*, **88**(003110), 2017.

[Nov15] O. Novotný, S. Allgeier, C. Enss, A. Fleischmann, L. Gamer, D. Hengstler, S. Kempf, C. Krantz, A. Pabinger, C. Pies, D. W. Savin, D. Schwalm, and A. Wolf, Cryogenic micro-calorimeters for mass spectrometric identification of neutral molecules and molecular fragments, *Journal of Applied Physics*, **118**(10), 2015.

[Nov19a] O. Novotný, P. Wilhelm, D. Paul, Á. Kálosi, S. Saurabh, A. Becker, K. Blaum, S. George, J. Göck, M. Grieser, F. Grussie, R. Von Hahn, C. Krantz, H. Kreckel, C. Meyer, P. M. Mishra, D. Muell, F. Nuesslein,

D. A. Orlov, M. Rimmler, et al., Quantum-state-selective electron recombination studies suggest enhanced abundance of primordial HeH+, *Science*, **365**(6454), 676–679, 2019.

[Nov19b] O. Novotný, P. Wilhelm, D. Paul, Á. Kálosi, S. Saurabh, A. Becker, K. Blaum, S. George, J. Göck, M. Grieser, F. Grussie, R. Von Hahn, C. Krantz, H. Kreckel, C. Meyer, P. M. Mishra, D. Muell, F. Nuesslein, D. A. Orlov, M. Rimmler, et al., Supplementary Materials: Quantum-state-selective electron recombination studies suggest enhanced abundance of primordial HeH+, *Science*, **365**(6454), 676–679, 2019.

[Pie08] C. Pies, Entwicklung eines Detektor-Arrays basierend auf magnetischen Kalorimetern für die hochaufgelöste Röntgenspektroskopie an hochgeladenen Ionen, Diploma thesis, Universität Heidelberg, 2008.

[Pie12] C. Pies, maXs-200: Entwicklung und Charakterisierung eines Röntgendetektors basierend auf magnetischen Kalorimetern für die hochauflösende Spektroskopie hochgeladener Ionen, PhD Thesis, Universität Heidelberg, 2012.

[Por11] J. Porst, High-Resolution Metallic Magnetic Calorimeters for β-Spectroscopy on 187Rhenium and Position Resolved X-Ray Spectroscopy, Diploma thesis, Universität Heidelberg, 2011.

[Riv20] V. M. Rivilla, J. Martín-Pintado, I. Jiménez-Serra, S. Martín, L. F. Rodríguez-Almeida, M. A. Requena-Torres, F. Rico-Villas, S. Zeng, and C. Briones, Prebiotic Precursors of the Primordial RNA World in Space: Detection of NH 2 OH , *The Astrophysical Journal*, **899**(2), L28, 2020.

[Rud54] M. A. Ruderman and C. Kittel, Indirect exchange coupling of nuclear magnetic moments by conduction electrons, *Physical Review*, **96**(1), 99–102, 1954.

[Sai09] L. Sainiemi, Cryogenic Deep Reactive Ion Etching of Silicon Micro and Nanostructures, Phd thesis, Helsinki University of Technology, 2009.

[Sch00] J. Schönefeld, Entwicklung eines mikrostrukturierten magnetischen Tieftemperatur-Kalorimeters zum hochauflösenden Nachweis von einzelnen Röntgenqanten, PhD Thesis, Universität Heidelberg, 2000.

[Sch13] H. Schmidt, R. Thomas, M. Gatchell, S. Rosen, P. Reinhed, P. Löfgren, L. Brännholm, M. Blom, M. Björkhage, J. Bäckström, J. D. Alexander, S. Leontein, D. Hanstorp, H. Zettergren, K. Liljeby, A. Källberg, A. Simonsson, F. Hellberg, S. Mannervik, M. Larsson, et al., First storage of ion beams in the Double Electrostatic Ion-Ring Experiment : DESIREE Experiment : DESIREE, *Review of Scientific Instruments*, **84**(005115), 2013.

[Sch15] D. Schulz, Entwicklung einer 4k-Pixel-Molekülkamera, basierend auf magnetischen Mikrokalorimetern, für den energie- und ortsaufgelösten Nachweis von neutralen Molekülfragmenten, Master thesis, Universität Heidelberg, 2015.

[Sch19] C. Schötz, PolarmaXs: hochauflösendes, polarisationssensitives Röntgenspektrometer basierend auf magnetischen Mikrokalorimetern, PhD Thesis, Universität Heidelberg, 2019.

[Sel10] K. Sellgren, M. W. Werner, J. G. Ingalls, J. D. Smith, T. M. Carleton, and C. Joblin, C60 in reflection nebulae, *Astrophysical Journal Letters*, **722**(1 PART 2), 54–57, 2010.

[Sik20] T. Sikorsky, J. Geist, D. Hengstler, S. Kempf, L. Gastaldo, C. Enss, C. Mokry, J. Runke, C. E. Düllmann, P. Wobrauschek, K. Beeks, V. Rosecker, J. H. Sterba, G. Kazakov, T. Schumm, and A. Fleischmann, Measurement of the Th 229 Isomer Energy with a Magnetic Microcalorimeter, *Physical Review Letters*, **125**(14), 142503, 2020.

[Sim35] F. Simon, Application of low temperature calorimetry to radioactive measurements, *Nature*, 763, 1935.

[Sno06] T. P. Snow and B. J. McCall, Diffuse Atomic and Molecular Clouds, *Annual Review of Astronomy and Astrophysics*, **44**(1), 367–414, 2006.

[Sök09] Ü. Sökmen, A. Stranz, S. Fündling, H. H. Wehmann, V. Bandalo, A. Bora, M. Tornow, A. Waag, and E. Peiner, Capabilities of ICP-RIE cryogenic dry etching of silicon: Review of exemplary microstructures, *Journal of Micromechanics and Microengineering*, **19**(10), 2009.

[Sök10] Ü. Sökmen, A. Stranz, S. Fündling, S. Merzsch, R. Neumann, H. H. Wehmann, E. Peiner, and A. Waag, Shallow and deep dry etching of silicon using ICP cryogenic reactive ion etching process, *Microsystem Technologies*, **16**(5), 863–870, 2010.

[Spa18] S. Spaniol, Electron Transport System for Fast-Timing-Readout at a Micro-Calorimeter Particle Detector, Bachelor thesis, Universität Heidelberg, 2018.

[Ste14] F. Steib, S. Merzsch, H. Wasisto, A. Stranz, P. Hinze, T. Weimann, E. Peiner, and A. Waag, Production of vertical nanowire resonators by cryogenic ICP DRIE, *Microsystem Technologies*, **20**, 759–767, 2014.

[Ste19] T. R. Stevenson, M. A. Balvin, S. R. Bandler, A. M. Devasia, P. C. Nagler, K. Ryu, S. J. Smith, and W. Yoon, Magnetic calorimeter option for the Lynx x-ray microcalorimeter, *J. Astron. Telesc. Instrum. Syst.*, **5**(2), 021009, 2019.

[Tac88] S. Tachi, K. Tsujimoto, and S. Okudaira, Low-temperature reactive ion etching and microwave plasma etching of silicon, *Applied Physics Letters*, **52**(8), 616–618, 1988.

[Tao71] L. Tao, D. Davidov, R. Orbach, and E. Chock, Hyperfine Splitting of Er and Yb in Au: A Separation between the Atomic and Covalent Contributions to the Exchange Integral, *Physical Review B*, **4**(1), 5–9, 1971.

[Ter18] B. Tercero, S. Cuadrado, A. López, N. Brouillet, D. Despois, and J. Cernicharo, Chemical segregation of complex organic O-bearing species in orion kl, *Astronomy and Astrophysics*, **620**, 1–12, 2018.

[Tes77] C. D. Tesche and J. Clarke, dc SQUID : Noise and Optimization, *Journal of Low Temperature Physics*, **29**(3/4), 301–331, 1977.

[Vel19] C. Velte, Measurement of a high energy resolution and high statistics 163Ho electron capture spectrum for the ECHo experiment, Phd thesis, Universität Heidelberg, 2019.

[vH06] R. von Hahn, V. Andriamarijaona, J. Crespo Lopez-Urrutia, H. Fadil, M. Grieser, C. Haberstroh, V. Mallinger, D. Orlov, H. Quack, M. Rappaport, C. Schröter, D. Schwalm, J. Ullrich, T. Weber, A. Wolf, and D. Zajfman, Cryogenic Concept for the Low-Energy Electrostatic Cryogenic Storage Ring (CSR) at MPI-K in Heidelberg, *Advances in Cryogenic Engineering: Transactions of the Cryogenic Engineering Conference*, **51**, 1187–1194, 2006.

[vH11] R. von Hahn, F. Berg, K. Blaum, J. Crespo Lopez-Urrutia, F. Fellenberger, M. Froese, M. Grieser, C. Krantz, K.-U. Kühnel, M. Lange, S. Menk, F. Laux, D. Orlov, R. Repnow, C. Schröter, A. Shornikov, T. Sieber, J. Ullrich, A. Wolf, M. Rappaport, et al., The electrostatic Cryogenic Storage Ring CSR Mechanical concept and realization, *Nuclear Instruments and Methods in Physics Research Section B: Beam Interactions with Materials and Atoms*, **269**(24), 2871–2874, 2011.

[vH16] R. von Hahn, A. Becker, F. Berg, K. Blaum, C. Breitenfeldt, H. Fadil, F. Fellenberger, M. Froese, S. George, J. Göck, M. Grieser, F. Grussie, E. A. Guerin, O. Heber, P. Herwig, J. Karthein, C. Krantz, H. Kreckel, M. Lange, F. Laux, et al., The cryogenic storage ring CSR, *Review of Scientific Instruments*, **87**(6), 2016.

[Wak10] V. Wakelam, I. W. Smith, E. Herbst, J. Troe, W. Geppert, H. Linnartz, K. Öberg, E. Roueff, M. Agúndez, P. Pernot, H. M. Cuppen, J. C. Loison, and D. Talbi, Reaction networks for interstellar chemical modelling: Improvements and challenges, *Space Science Reviews*, **156**(1-4), 13–72, 2010.

[Wel94] F. C. Wellstood, C. Urbina, and J. Clarke, Hot-electron effects in metals, *Physical Review B*, **49**(9), 5942–5955, 1994.

[Wil69] G. Williams and L. Hirst, Crystal-field effects in solid solutions of rare earths in noble metals, *Physical Review*, 1969.

[Wil19] P. Wilhelm, First Studies of Low-Energy Electron Cooling of keV Energy Ion Beams at the Electrostatic Cryogenic Storage Ring CSR, PhD Thesis, Universität Heidelberg, 2019.

[Xue20] C. Xue, E. R. Willis, R. A. Loomis, K. L. Kelvin Lee, A. M. Burkhardt, C. N. Shingledecker, S. B. Charnley, M. A. Cordiner, S. Kalenskii, M. C. McCarthy, E. Herbst, A. J. Remijan, and B. A. McGuire, Detection of Interstellar HC 4 NC and an Investigation of Isocyanopolyyne Chemistry under TMC-1 Conditions , *The Astrophysical Journal*, **900**(1), L9, 2020.

[Yoo20] W. Yoon, M. A. Balvin, S. R. Bandler, A. M. Devasia, P. C. Nagler, K. Ryu, S. J. Smith, and T. R. Stevenson, Position-Sensitive Magnetic Calorimeters for Lynx, *Journal of Low Temperature Physics*, **199**(3), 916–922, 2020.

[Yos57] K. Yosida, Magnetic properties of Cu-Mn alloys, *Physical Review*, **106**(5), 893–898, 1957.

[Zha11] Y. Zhang and S. Kwok, Detection of C60 in the protoplanetary nebula IRAS 01005+7910, *Astrophysical Journal*, **730**(2), 2011.

[Zie10] J. F. Ziegler, M. D. Ziegler, and J. P. Biersack, SRIM - The stopping and range of ions in matter (2010), *Nuclear Instruments and Methods in Physics Research, Section B: Beam Interactions with Materials and Atoms*, **268**(11-12), 1818–1823, 2010.